Università degli Studi di Padova
Department of Information Engineering

MASTER DEGREE IN
INFORMATION AND COMMUNICATION TECHNOLOGIES
FOR INTERNET AND MULTIMEDIA
CURRICULUM: PHOTONICS AND QUANTUM ENGINEERING

Quantum Cavity Optoacoustics at Room Temperature using a cm-scale Crystal

Candidate:
Davide Tomasella
ID 2037849

Supervisor:
Dr. Francesco Vedovato
Università degli Studi di Padova

Co-Supervisors:
Prof. Ulrik Lund Andersen
Denmark Technical University
Doct. Santiago Tarrago Velez
Denmark Technical University

Academic Year 2022/2023

Preface

This thesis is the result of my traineeship at the Department of Physics at the Denmark Technical University under the program Erasmus+ For Studies, fulfilling the requirements for the Master's degree in ICT for Internet and Multimedia at the University of Padua. The work was carried out in the Quantum Physics and Information Technology (QPIT) group, Center for Macroscopic Quantum States (bigQ), under Prof. Ulrik Lund Andersen supervision.

This project allowed me to deepen my knowledge in Physics and Quantum Optics and to enhance my skills in experimental physics, in addition to experiencing a stimulating environment rich in talented scientists at QPIT. I consider it the accomplishment of five years of studies, dedication, and passion and hopefully a stepping stone for my future achievements. I wish to thank Dr. Francesco Vedovato and Prof. Ulrik Lund Andersen for the opportunity to develop this thesis and for their constant support during the period in Italy and Denmark. A special greeting is dedicated to Santiago Tarrago Velez for the collaboration in the laboratory and the stimulating discussions during the project. Another warm thank you goes to the optomechanics team and the entire QPIT group for their hospitality during the months I spent with them. Finally, I am also thankful to all professors, friends, and family, with whom I spent incredible moments during my Bachelor's and Master's degrees, for helping me grow and improve.

<div align="right">

DAVIDE TOMASELLA
Kongens Lyngby - Padova
July 2023

</div>

Abstract

Cavity optomechanics is a field that investigates the interaction between photons and phonons in optomechanical cavities, offering insights into fundamental physics and potential applications in quantum technologies.

This master thesis focuses on exploring the strong-coupling regime in a macroscopic system operating at room temperature, utilizing a centimeter-scale quartz crystal enclosed within an optical resonator capable of sustaining high-frequency bulk acoustic waves at approximately $12.5\,\mathrm{GHz}$. The Brillouin optomechanical interactions couple the light to the mechanical system and, when the phenomenon is in resonance with the optical cavity modes, enable the transferring of energy between them, i.e., optomechanically induced amplification (OMIA) and transparency (OMIT).

Operating at room temperature presents several advantages, including the ability to thermally tune the cavity resonances and employ high-power optical beams ($\sim 100\,\mathrm{mW}$). These conditions enable the achievement of the strong-coupling regime with an effective photon coupling rate in the MHz range. In this regime, the confinement and intrinsic losses of the optical and acoustic modes are overcome by the light coupled from the optical pump and create hybrid optoacoustic modes.

The results of this work serve as essential prerequisites for investigating Brillouin interactions at cryogenic temperatures and enabling the development of hybrid quantum technologies, such as quantum memories and microwave-to-optical transducers.

Contents

Introduction 1

In recent years, Quantum Mechanics has transitioned from a purely fundamental science into the technological realm. The development of advanced quantum setups that exploit new principles to enhance the performances and widen the application range raises new requirements to extend the systems' quantum coherence and develop practical devices for industrial and commercial applications. Quantum transducers enter the scene as a tool to integrate different platforms and overcome the respective limits. They can coherently transfer quantum information between systems, thus incorporating operations usually relegated to specific platforms into the same infrastructure, significantly expanding their capabilities.

A clear cooperation example is the network of quantum computers that can receive, process, and transmit information encoded into quantum states [1]. The quantum internet is essential for more secure communication and cloud quantum computing. However, the integration between the diverse physical platforms is still challenging. Quantum computers have quickly developed into several physical platforms with diverse requirements and incompatible operation environments [2]. The most common semiconductor qubits require cryogenic temperatures and microwave control signals [3, 4], which contrast with laser-operated trapped-ions quantum computers [5] or even room-temperature photonic circuits [6]. On the other hand, quantum communication systems rely on optical devices exploiting the already-deployed optical fiber network to implement quantum key distribution applications by exchanging photons between distant parties [7, 8]. Microwave-to-optical transducers are thus critical technology because they convert light quanta into electrical signals, usable in most of the solid-state quantum information processing systems [9–11]. They enable connecting different processing nodes [12] and establishing long-distance hybrid quantum networks [13], in addition to providing another substantial piece, i.e., quantum memories with long decoherence time [14, 15].

Other than the technological empowering, Quantum Mechanics has developed after the second quantum revolution towards investigating the macroscopic world. From the initial wave-particle dualism experiments with electrons and photons, the aim has always been to understand the limits of the theory and the boundary between a microscopic quantum system and a macroscopic classical one [16]. Most quantum experiments rely on photons, atoms, or nanoscale structures to test quantum properties and manipulate quantum states, demonstrating quantum entanglement [17], quantum teleportation [18], etc. Nevertheless, more experiments have proved that the larger the system, the shorter the decoherence time before the disappearance of quantum effects because of the increased difficulty in minimizing the interactions with the external environment. Still, the presence of a precise boundary

between quantum and classic frameworks is unclear, and more advanced technologies are needed to improve our measurements and provide a conclusive answer.

In this environment, optomechanics has bloomed as a promising way to address many technological challenges in implementing efficient quantum transducers and explore the limits of the current quantum theory [19]. Optomechanics describes the interaction between the optical field and the quantized mechanical motion, i.e., in terms of photons and phonons. The optomechanical coupling enables energy transfer between the modes in the two subsystems and requires a coupled description of the optomechanical oscillator. Within this concept, many successful designs have been proposed and implemented using a variety of supports from membranes [11, 20] to phononic-crystal resonators [21] relying on different physical interactions and with diverse advantages and limits [22] to increase the optomechanical coupling strength and the quality factor x frequency product (Qf) [23]. In several applications, the Qf product is the key figure of merit because it displays the coherence degree of the acoustic modes, i.e., the higher the phonon frequency and the cavity quality factor, the lower the interactions with the environment and the longer the phonon lifetime.

This thesis characterizes a room-temperature high-frequency bulk optomechanical setup, aiming at the strong-coupling regime [19]. The setup comprises a centimeter-scale quartz crystal placed inside an optical cavity to enhance the optomechanical coupling strength. The quartz lattice supports 12.5-GHz phonons that have higher frequency compared to the more common membrane systems, and the crystal's macroscopic nature allows the propagation of bulk acoustic waves (BAW) in the material. The optomechanical interaction is based on Brillouin scattering, where the counter-propagating optical modes generate time-dependent electrostriction in the material, equivalent to a propagating BAW. Although working at room temperature prevents cooling down the phonons to the ground state, i.e., the mode thermal occupancy is smaller than one, we can still characterize several peculiar behaviors, e.g., the strong-coupling regime.

In the strong-coupling regime, the interaction rate (or coupling strength) between light and mechanical motion surpasses both the dissipation rates of the optical and mechanical components and can be achieved by increasing the laser power, i.e., the number of photons circulating inside the optical cavity suitable to interact. In general, achieving strong coupling in optomechanical devices within micro- and nano-mechanical systems [24, 25] is not straightforward due to practical limits on the circulating number of photons, which limit the cavity-enhanced coupling rate [26, 27]. Instead, the use of high-frequency optomechanical platforms and high-finesse optical cavities can lead to high Qf products and lower thermal decoherence that is advantageous for operating at cryogenic temperatures while remaining in the ground state [28]. In fact, cryogenic temperatures increase the phonon lifetime, transforming the crystal into a BAW resonator [29, 30], essential for transferring and memorizing quantum states into the mechanical modes [11, 14].

The results of this project first demonstrate Brillouin lasing and strong coupling at room temperature for this optomechanical system [31]. If phonon lasing has already been shown at low temperatures [32], Brillouin lasing involving acoustic linewidth broader than the optical one has never been presented for macroscopic quartz crystals. Examples of strong coupling in an optomechanical system have been displayed in cryogenic systems with kHz mechanical linewidths and, thus, less demanding power constraints [28], and a room temperature with a fused-silica optomechanical platform [33].

The structure of this manuscript comprises three parts: a theoretical introduction of the formalism developed to study the optomechanical response, an analysis of the measurement setup and the optical cavity, and a discussion of the main results. In Chapter 2, we introduce the optomechanics theory, focusing on the Quantum Mechanics description of an optoacoustic device. The following Chapter 3 presents a characterization of the optical response of

the optomechanical cavity when a quartz crystal is inserted and the mechanical assembly temperature dependence as a tool to tune the cavity length and the free spectral range (FSR) to enhance the optomechanical coupling. Chapter 4 describes Brillouin scattering as the source of optomechanical interaction, divided into Stokes and Anti-Stokes scattering, which can be selectively suppressed in our cavity thanks to the non-uniform resonance mode distribution. The theory concludes in Chapter 5 with a mathematical model of the cavity spectral response, including the optomechanical interaction between the addressed optical modes. In Chapter 6, we present the cavity design and the measurement setup, jointly with a performance evaluation and the data analysis methods. Finally, Chapter 7 reports and discussion the results for the Optomechanical Induced Amplification (OMIA) and Transparency (OMIT), demonstrating Brillouin lasing and strong coupling and noting an estimate for the single-photon coupling rate.

Optomechanics 2

2.1 A general description of an optomechanical system

When we operate with an optical system, we often inquire about how laser light evolves after interacting with solid matter. Optomechanics explores the interaction between light and mechanical motion at the quantum level. It combines concepts from quantum optics and condensed matter physics to investigate the fundamental physical phenomena that arise when light and mechanical systems are coupled in a confined space such as an optomechanical cavity. The interaction between light confined in a high-quality optical cavity and a mechanical oscillator enables the manipulation and control of both the optical and mechanical degrees of freedom, leading to intriguing phenomena and potential applications in quantum information processing [15], precision measurement [34], and fundamental tests of quantum mechanics [17, 18, 35]. In particular, optomechanics offers a unique platform to study quantum effects at the macroscopic scale [35].

The fundamental elements of a typical cavity optomechanical system include an optical cavity, a mechanical resonator, and a coupling mechanism between them [19]. The optical cavity, formed by two highly reflective mirrors, allows light confinement within a small volume. The mechanical resonator, on the other hand, can be any structure that exhibits mechanical motion, such as a micro- or nanoscale cantilever, a vibrating membrane, or the atom vibration in a crystal lattice, as the main focus of this work. Each system presents different mechanical properties, allowing different phenomena and applications. We can consider very diverse examples: the micromovements of optical mirrors due to radiation pressure to measure external forces [36], the manipulation of nanoparticles through optical tweezers [37], the cooldown of mechanical trampolines using laser cooling [26], or electrostrictive forces that lead to acoustic waves inside materials [29]. However, we can always map the optomechanical interaction at the base into the formalism of radiation pressure generated from the light impinging on a mechanical element. In easy terms, coherent light exerts a force proportional to its intensity, leading to a displacement or vibration of the mechanical component. This back-action from the mechanical motion can then modify the properties of the light, creating a feedback loop between the optical and mechanical systems (Figure 2.1).

We can thus model the behavior of a general optomechanical system by treating the optical cavity as a resonator with discrete electromagnetic mode and the mechanical resonator as a harmonic oscillator. Finally, the coupling between the optical and mechanical modes is characterized by the optomechanical coupling strength, which quantifies the intensity of the interaction. Moreover, we can apply the Quantum Mechanics framework to this description
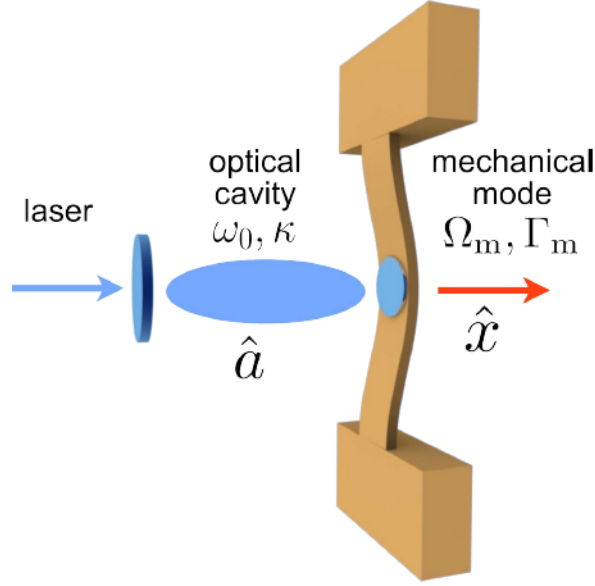
FIGURE 2.1: Scheme of an optomechanical system. A laser beam impinges on an optical cavity and transfers energy to the mode $\hat{a}$. The photons propagating inside the cavity apply radiation pressure on a movable mirror, generating mechanical oscillations $\hat{x}$. This movement generates a close loop with the optical system because of a change in the cavity resonant frequency, creating a coupled photon-phonon mode. Image adapted from [19].

to study the optomechanical system at the single photon and phonon level.

In the following sections, we deepen these concepts by reviewing the main parameters of optical and mechanical resonators in Section 2.2 before describing the optomechanical interaction using the coupled mode theory in Section 2.3. Finally, we introduce the Quantum Mechanics formulation of the two-mode system through the interaction picture (Section 2.4).

2.2 Optical cavities and mechanical resonators

As we just described, the fundamental description of each optomechanical system lies in two elementary elements, i.e., the optical cavity and the mechanical resonator. Despite the intrinsic difference in the physical implementation between the two, their description follows the same outline. In this section, we include only a summary of the main parameters to introduce the notation used in the following, leaving a complete description of the topic to any standard optics textbook or review paper [19].

2.2.1 Fabry-Pérot cavity

Optical resonators can assume different experimental realizations, but their properties can be derived from the basic case of a Fabry-Perot resonator. We will thus focus on reporting the mathematical description of a cavity pumped with a single monochromatic laser source. A Fabry-Pérot resonator consisting of two highly reflective mirrors, separated by a distance L. The phase-matching conditions of the propagating light create constructive interference patterns between the two mirrors, leading to a series of resonances given by the angular frequency

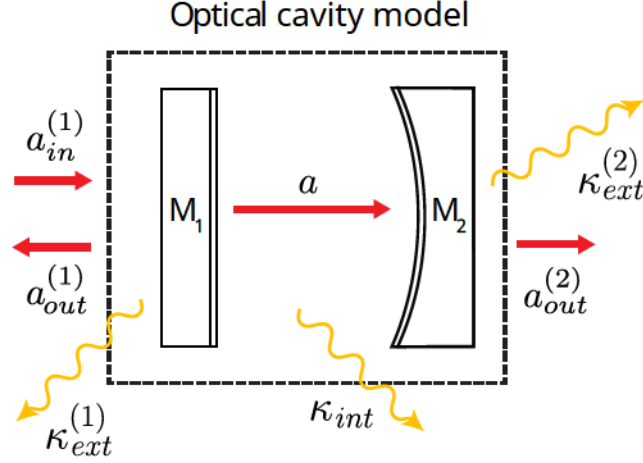$$\omega_j \approx j\pi\frac{c}{L} \tag{2.1}$$

FIGURE 2.2: Scheme of the fundamental elements of a Fabry-Perot resonator. The optical cavity comprises two mirrors M_1 and M_2, which define the cavity mode a and the respective input-output interfaces. The input field is identified with $a_{in}^{(1)}$, whereas $a_{out}^{(1)}$ and $a_{out}^{(2)}$ represents the reflected and transmitted fields. Three different types of losses contribute to the total decay rate of the cavity mode κ: the light propagating through the two mirrors $\kappa_{ext}^{(1)}$ and $\kappa_{ext}^{(2)}$, and the intrinsic losses κ_{int}.

with j the integer mode number. We also characterize the separation between the resonances as the free spectral range (FSR) of the cavity

$$\text{FSR} = \omega_{j+1} - \omega_j = \pi \frac{c}{L}. \tag{2.2}$$

Even in the ideal case where all the behavior is frequency-independent, we can identify two contributions that limit the photon lifetime within the optical cavity. In fact, both the light escaping from the mirrors κ_{ext} (confinement of external losses) and the scattering or absorption inside the cavity κ_{int} (intrinsic or internal losses) sum up to the total cavity decay rate $\kappa = \kappa_{int} + \kappa_{ext}$. We can finally define the optical finesse $\mathcal{F}$ as the average number of round-trips before a photon leaves the cavity:

$$F = \frac{\text{FSR}}{\kappa} \tag{2.3}$$

and the quality factor of the optical resonator,

$$Q = \omega\tau = \frac{\omega}{\text{FSR}}\mathcal{F} \tag{2.4}$$

where $\tau = \kappa^{-1}$ is the photon lifetime.

A more precise analysis of the cavity losses identifies different sources for the intrinsic and external contributions that are worth mentioning for further analysis. Within the confinement losses, we identify the coupling efficiency of the input field to the cavity as the contribution of the input mirror finite transparency, whereas the intrinsic ones can originate from the energy dissipated within the cavity elements or the one coupled to other optical modes, where the difference lies the scope of the phenomenon we are analyzing. As a pertinent example, in an optomechanical system, the optical power coupled from the optical modes to the mechanical system k_{opt} is usually described as couple efficiency because of its centrality in the phenomenon description. However, in other optical systems, k_{opt} and other scattering contributions are all parts of the intrinsic losses because we give a diverse system description.

Finally, we define a cavity critically coupled when the input coupling losses $k_{ext}^{(1)}$ equal all the other contributions denoted with κ_0, i.e., they are half the total losses

$$\kappa = k_{int} + k_{ext}^{(1)} + k_{ext}^{(2)} = k_0 + k_{ext}^{(1)} = 2k_{ext}^{(1)}. \tag{2.5}$$

A quantum mechanical description of the Fabry-Pérot cavity response underlies the input-output theory framework, where the input and output modes are described by the Quantum Mechanics operators $\hat{a}_{in}$ and $\hat{a}_{out}$ identifying the amplitude of the electromagnetic fields. This abstract description is related to the previous model when we define the input mode as the monochromatic light impinging the optical cavity and the output mode as the reflected one $\hat{a}_{out}^{(1)}$, while the transmitted field $k_{ext}^{(2)}$ is absorbed within the loss contribution κ_0. In the same way, we could also focus on the transmitted mode $\hat{a}_{out}^{(1)}$ by absorbing the input port coupling coefficient $k_{ext}^{(2)}$ in the cavity internal losses. From this starting point, it is easy to describe the time evolution of the field inside the optical cavity $\hat{a}$ using the Heisenberg-Langevin equations of motions [38] and the previously described loss contributions.

$$\dot{\hat{a}} = -\frac{\kappa}{2}\hat{a} + i\Delta\hat{a} + \sqrt{\kappa_{ext}^{(1)}}\hat{a}_{in} \tag{2.6}$$

In (2.6), we identify the contribution from the external field coupling inside the cavity $\hat{a}_{in}$ and the decay rate of the internal field $\kappa/2$. Furthermore, we can define the laser detuning with respect to the central frequency of the cavity mode ω_0 as $\Delta = \omega_L - \omega_0$ as the result of employing the Heisenberg picture with a rotating frame at frequency ω_L, i.e., the laser frequency.

To complete the description, we should include the definition of the input power P_{in} as the expectation of the number of photons $\langle \hat{a}_{in}^\dagger \hat{a}_{in} \rangle$ multiplied by the energy of each photon $\hbar\omega_L$

$$P_{in} = \hbar\omega_L \langle \hat{a}_{in}^\dagger \hat{a}_{in} \rangle = \hbar\omega_L |\alpha_{in}|^2, \tag{2.7}$$

where α is the amplitude of the electromagnetic field. The transmitted field is defined as

$$\hat{a}_{out}^{(1)} = \hat{a}_{in} - \sqrt{\kappa_{ext}^{(1)}}\hat{a} \tag{2.8}$$

while the output field reflected by the Fabry-Pérot resonator

$$\hat{a}_{out}^{(2)} = \sqrt{\kappa_{ext}^{(2)}}\hat{a} \tag{2.9}$$

together with their corresponding powers

$$P_{out}^{(1)} = \hbar\omega_L \langle \hat{a}_{out}^{(1)\dagger} \hat{a}_{out}^{(1)} \rangle = \hbar\omega_L \left| \alpha_{out}^{(1)} \right|^2 = \hbar\omega_L \left| \alpha_{in} - \sqrt{\kappa_{ext}^{(1)}}\alpha \right|^2 \tag{2.10}$$

$$P_{out}^{(2)} = \hbar\omega_L \langle \hat{a}_{out}^{(2)\dagger} \hat{a}_{out}^{(2)} \rangle = \hbar\omega_L \left| \alpha_{out}^{(2)} \right|^2 = \hbar\omega_L \kappa_{ext}^{(2)} |\alpha|^2. \tag{2.11}$$

Finally, we define the steady-state intracavity field as a function of the input mode $\hat{a}$ by solving the motion equation:

$$\hat{a} = \frac{\sqrt{\kappa_{ext}^{(1)}}\hat{a}_{in}}{\kappa/2 - i\Delta}. \tag{2.12}$$

Its corresponding intracavity photon number N in the steady-state population is

$$N = \langle \hat{a}^\dagger \hat{a} \rangle = \left| \frac{\sqrt{\kappa_{ext}^{(1)}}\alpha_{in}}{\kappa/2 - i\Delta} \right|^2 = \frac{\kappa_{ext}^{(1)} |\alpha_{in}|^2}{\kappa^2/4 + \Delta^2}. \tag{2.13}$$
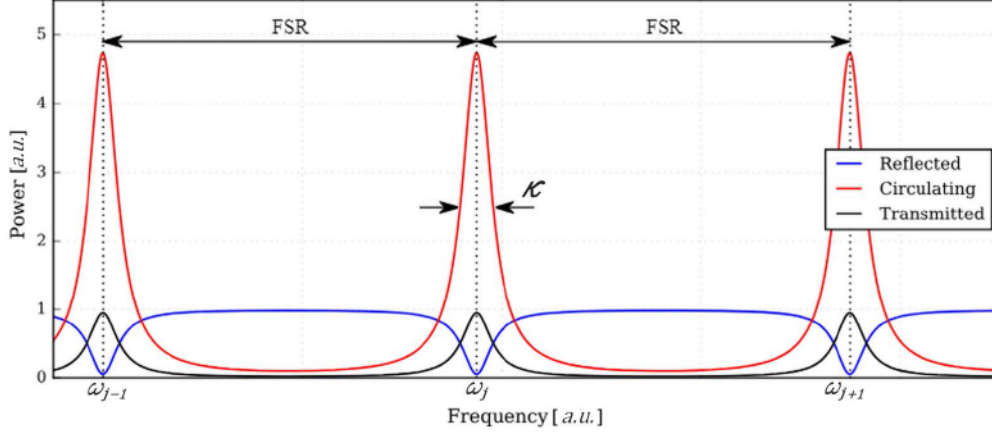
FIGURE 2.3: The spectral response of a Fabry-Perot cavity is periodic in frequency and displays the characteristic transmission windows in correspondence with the cavity mode frequencies. The modes represent a build-up of power inside the cavity because of the constructive interference of the electromagnetic waves, normalized to the input cavity power. The separation between the transmission peaks is the FSR and depends on the geometry of the optical cavity. Together with the linewidth κ of the modes, it defines the cavity Finesse $\mathcal{F}$, i.e., the average number of rounds inside the cavity before the light can escape. Image from [39].

A final remark should consider that this expression accounts only for the behavior of a single resonance and thus is valid when the decay rate κ is much smaller than the FSR, i.e., the frequency response of the different modes does not overlap.

2.2.2 Mechanical resonator

Mechanical resonators are physical systems that exhibit vibrational motion at specific frequencies. They can be realized in various forms, such as micro- and nanoscale structures, where their mechanical vibrations are confined to specific modes. This property makes their mathematical model similar to the one of an optical cavity where the photon number evolution is substituted with phonon, i.e., the quantum of vibrational motion at a given frequency Ω_m. The difference compared to an optical system lies in the physical properties of this energy propagation. Talking about vibration is equivalent to analyzing the displacement of single atoms or larger structures, and we can thus formalize the behavior of the system through a simple equation of motion of a harmonic oscillator of effective mass m_{eff}:

$$m_{eff}\frac{dx^2(t)}{dt^2} + m_{eff}\Gamma_m\frac{dx(t)}{dt} + m_{eff}\Omega_m^2 x(t) = F_{ext}(t) \tag{2.14}$$

where $F_{ext}(t)$ denotes the sum of all forces acting on the mechanical oscillator and comprises the radiation pressure, in addition to the intrinsic thermal Langevin force, when describing the interaction in an optomechanical system. In the model, we again consider a frequency-independent dumping rate Γ_m related to the different energy dissipation types: external, like viscous dumping and dumping losses, in particular when we study trampolines and cantilevers, and internal, like thermoelastic dumping and material-induced losses (defect atom states).

In analogy to expressing the intracavity field of an optical cavity in terms of the photon number evolution, the displacement of a mechanical resonator can be defined both in terms of the phonon number evolution $\hat{b}$ and mechanical displacement $\hat{x}$. This allows for the quantization

of mechanical motion and enables the study of quantum mechanical effects in these systems. Using the same formalism as before and substituting the external force with a phonon mode $\hat{b}_{in}$, we can express the phonon mode temporal evolutions as

$$\dot{\hat{b}} = -\frac{\Gamma_m}{2}\hat{b} + i\Omega_m\hat{b} + \sqrt{\Gamma_m}\hat{b}_{in}, \tag{2.15}$$

which leads to a steady state of the number of phonons. In the absence of external contributions, the steady-state population $N_{th} = \langle \hat{b}^\dagger \hat{b} \rangle$ corresponds to the thermal equilibrium of the system, which can be approximated in the high-temperature limit as

$$N_{th} \approx \frac{k_B T}{\hbar \Omega_m}, \tag{2.16}$$

where k_B is the Boltzmann constant and T is the environment temperature.
The relation between the phonon formalism and the mechanical oscillator equation lies in the creation and annihilation operators of the phonon field that is derived from the quadrature components of the mechanical displacement, i.e., the position $\hat{x}$ and the momentum $\hat{p}$, in the same way as the quadrature components of the electromagnetic field are obtained (Figure 2.4). We can thus write

$$\hat{x} = x_{\text{ZPF}}(\hat{b} + \hat{b}^\dagger), \qquad \hat{p} = -im_{eff}\Omega_m x_{\text{ZPF}}(\hat{b} - \hat{b}^\dagger) \tag{2.17}$$

where x_{ZPF} is the zero-point fluctuation amplitude of the mechanical oscillator

$$x_{\text{ZPF}} = \sqrt{\frac{\hbar}{2m_{eff}\Omega_m}}. \tag{2.18}$$
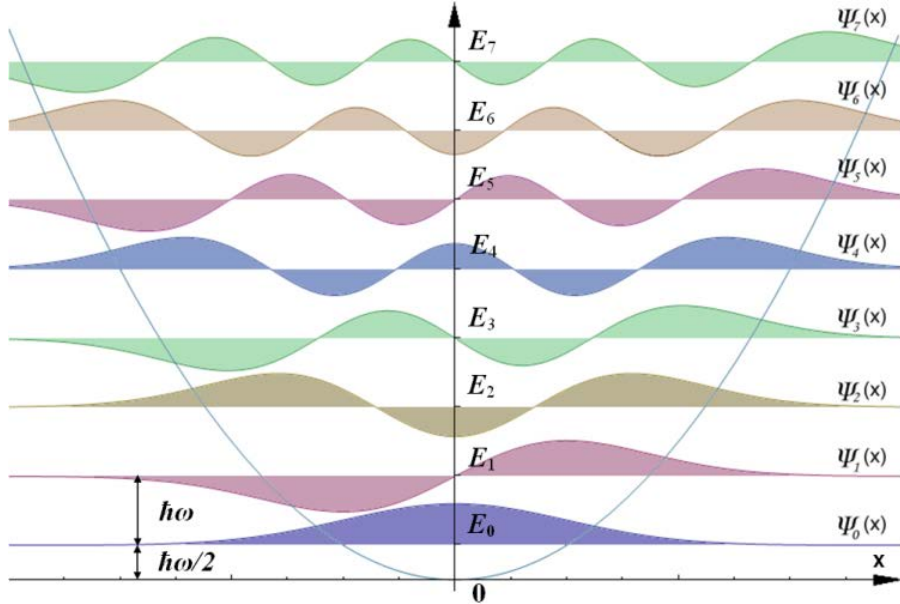
FIGURE 2.4: Representation of the energy distribution inside a mechanical resonator. The wavefunction ϕx is confined within the structure and a finite-energy level structure appears. The lowermost level represents the ground state, and the spatial distribution of the mode $\phi_0(x)$ defines the zero-point fluctuation of the system. Above this state are all the excited states created by the absorption of phonons from the external environment until thermal equilibrium is reached. Image from [40].

As expected, we can also define the mechanical quality factor Q by accounting for all the dumping contributions. Nevertheless, a mechanical vibration has a much lower frequency compared to an optical system, and the number of coherent oscillations is thus highly limited by thermal decoherence in room-temperature environments. For this reason, various techniques, such as material engineering, device design optimization, and cryogenic cooling, are employed to minimize these losses and enhance the quality factor of mechanical resonators. In this experiment, we cannot create a mechanical cavity because, in addition to the limited lifetime of the phonons, the propagation speed in the material and the length of the crystal prevent a standing wave from forming. We are thus limited in the ability to increase the strength of the interaction between the optical and mechanical modes, and we can only rely on the cavity-enhanced photons population. Despite not being able to create a mechanical resonator, we still have to match the correct frequency and direction of propagation to couple power into and out of the mechanical modes, since the physical constraints for the propagation of the acoustic wave must be complied with.

2.3 Coupled mode theory and optomechanical coupling

In an optomechanical system, the fundamental mechanism that couples the cavity radiation field to the mechanical motion depends on the system's specific mechanical structure. This coupling can manifest in different ways, such as direct momentum transfer from radiation pressure to movable objects, a dispersive frequency shift caused by a membrane within the cavity, near-field effects due to entrapped particles in a laser beam, or strain-optical effects that modulate the refractive index and lead to acoustic wave scattering. Regardless of the physical interpretation of the force, the interaction between a radiation mode and a vibrational mode can always be understood by considering the shift in the cavity resonance frequency as a function of displacement and the intensity of the optical beam. This common description (Figure 2.2) allows for a general framework to study optomechanical systems using the coupled mode theory.

Both optical cavities and mechanical resonators can be described in terms of the time evolution of photon ($\hat{a}$) and phonon ($\hat{b}$) numbers in their respective modes (Figure 2.5). With this understanding, we can establish a common framework to describe the interaction between the two systems. This approach, known as the coupled mode theory, recognizes that a probability exists for the two systems to interact and exchange energy quanta.

Without losing in generality, we restrict our attention to one of the many optical modes ω_0,
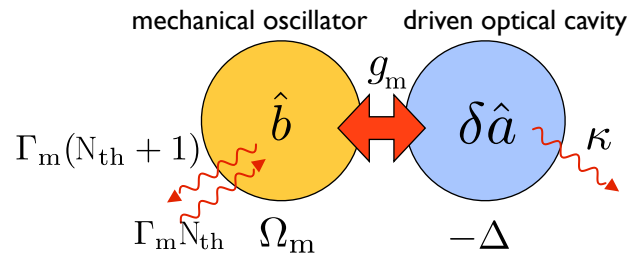
FIGURE 2.5: Pictogram of a basic optomechanical system. On the left, a mechanical oscillator $\hat{b}$ interacts with the environment to maintain thermal equilibrium. On the right, the optical cavity $\hat{a}$ is excited through an external field and shows fluctuation $\delta\hat{a}$ around its equilibrium. The optomechanical interaction g_m between the two systems creates hybrid photon-phonon modes and enables us to sense or control the mechanical side through the optical field. Image adapted from [19].

i.e., the one closest to resonance with the driving laser. Moreover, we also describe only one of the many mechanical normal modes Ω_m. Starting from the Hamiltonian $\hat{H}_0$ of the uncoupled optical and mechanical modes without external fields (free-evolution Hamiltonian) from (2.6) and (2.15)

$$\hat{H}_0 = i\hbar\frac{\kappa}{2}\hat{a}^\dagger\hat{a} + \hbar\omega_0\hat{a}^\dagger\hat{a} + i\hbar\frac{\Gamma_m}{2}\hat{b}^\dagger\hat{b} + \hbar\Omega_m\hat{b}^\dagger\hat{b}, \tag{2.19}$$

we can define the optical frequency shift per displacement as

$$G = -\partial\omega_0/\partial x \tag{2.20}$$

after acknowledging that the optical resonance frequency depends on the position of the mechanical moving element ($\omega_0(x) = \omega_0 + x\partial\omega_0/\partial x + ...$). Furthermore, by using a first-order expansion for the displacement, we have that the Hamiltonian becomes

$$\hat{H}_0 = i\hbar\frac{\kappa}{2}\hat{a}^\dagger\hat{a} + \hbar(\omega_0 - G\hat{x})\hat{a}^\dagger\hat{a} + i\hbar\frac{\Gamma_m}{2}\hat{b}^\dagger\hat{b} + \hbar\Omega_m\hat{b}^\dagger\hat{b} \tag{2.21}$$

with $\hat{x}$ as in (2.17). Thus, the interaction part of the Hamiltonian can be written

$$\hat{H}_{int} = -\hbar g_0\hat{a}^\dagger\hat{a}(\hat{b} + \hat{b}^\dagger), \tag{2.22}$$

where

$$g_0 = Gx_{\text{ZPF}} \tag{2.23}$$

is the vacuum optomechanical coupling strength, expressed as a frequency, and quantifies the interaction between a single phonon and a single photon. The radiation-pressure force is derived from the interaction Hamiltonian as

$$\hat{F} = -\frac{d\hat{H}_{int}}{d\hat{x}} = \hbar G\hat{a}^\dagger\hat{a} = \hbar\frac{g_0}{x_{\text{ZPF}}}\hat{a}^\dagger\hat{a}. \tag{2.24}$$

As we already described before, the full Hamiltonian should also include the dissipation terms of the optical and mechanical modes, the fluctuation of the number of phonons due to thermal influx, and the driving external optical field. In the same rotating frame following the laser frequency, we can thus express the complete Hamiltonian as

$$\hat{H} = i\hbar\frac{\kappa}{2}\hat{a}^\dagger\hat{a} - \hbar\Delta\hat{a}^\dagger\hat{a} + i\hbar\frac{\Gamma_m}{2}\hat{b}^\dagger\hat{b} + \hbar\Omega_m\hat{b}^\dagger\hat{b} - \hbar g_0\hat{a}^\dagger\hat{a}(\hat{b} + \hat{b}^\dagger), \tag{2.25}$$

where $\Delta = \omega_L - \omega_0$ is the optical frequency detuning as before.

Even if this Hamiltonian provides a complete description of an optomechanical system, its usage is limited by the non-linear terms in the interaction part that prevent an analytical (and often even a numerical) solution for the optical and mechanical evolution. In the following section, we employ the perturbation theory to linearize the interaction Hamiltonian and simplify the modeling of the phenomenon.

2.4 Linearized Hamiltonian of the optomechanical interactions

The general interacting Hamiltonian reported in (2.22) represents all the possible energy exchange contributions comprising the optomechanical interaction between an optical and an acoustic mode. To extract information from this expression, we introduce the linearized approximate description of cavity optomechanics that assumes the optomechanical response is a perturbation of the optical mode, i.e., the optical mode has high power to not being

depleted by the optomechanical interaction transferring of power. With this first assumption, we can rewrite the optical cavity field as an average coherent amplitude $\alpha = \langle \hat{a} \rangle = \langle \hat{a}^\dagger \hat{a} \rangle$ and a fluctuating term $\delta \hat{a}$

$$\hat{a} = \alpha + \delta \hat{a}, \tag{2.26}$$

thus rewriting the interaction Hamiltonian as

$$\begin{aligned} \hat{H}_{int} = & -\hbar g_0 (\alpha + \delta \hat{a})^\dagger (\alpha + \delta \hat{a})(\hat{b} + \hat{b}^\dagger) \\ = & -\hbar g_0 |\alpha|^2 (\hat{b} + \hat{b}^\dagger) - \hbar g_0 (\alpha^* \delta \hat{a} + \alpha \delta \hat{a}^\dagger)(\hat{b} + \hat{b}^\dagger) - \hbar g_0 \delta \hat{a}^\dagger \delta \hat{a}(\hat{b} + \hat{b}^\dagger) \end{aligned} \tag{2.27}$$

The first term identified in (2.27) is proportional to $|\alpha|^2$ and thus also to the average radiation-pressure force $F = \hbar G |\alpha|^2$ from (2.24) that shifts the optical mode resonance frequency because of the mechanical displacement and can be omitted after compensating for it. As anticipated in the previous section, the mechanical motion induces a shift of the optical resonance frequency, which results in a change of circulating light intensity and, therefore, of the radiation pressure force acting on the motion, creating a feedback loop known as optomechanical "back-action". The second term is $-\hbar g_0 (\alpha^* \delta \hat{a} + \alpha \delta \hat{a}^\dagger)(\hat{b} + \hat{b}^\dagger)$ and corresponds to the linearized interacting Hamiltonian. When we rewrite the coherent field intensity as a function of the cavity photon number N, we obtain

$$\hat{H}_{int}^{(lin)} = -\hbar g_m (\delta \hat{a} + \delta \hat{a}^\dagger)(\hat{b} + \hat{b}^\dagger) \tag{2.28}$$

where

$$g_m = g_0 \sqrt{N} \tag{2.29}$$

is known as the effective optomechanical coupling strength and depends linearly on the amplitude of the optical field inside the cavity. Finally, the third term $\propto \delta \hat{a}^\dagger \delta \hat{a}$ can be neglected if the fluctuations in the optical field are small enough. As an additional remark, the linearized description is usually accurate even if the average photon number inside the cavity is not large since the mechanical system can't resolve the individual photons if the decay rate κ is sufficiently large.

A further analysis of the linearized interacting Hamiltonian can lead to splitting the description of the optomechanical response into two separate terms. It brings particular significance to this experiment because, as we will amply discuss in the following chapter, we can efficiently suppress one of the two interactions thanks to the particular property of our system. The first term is

$$\hat{H}_{BS} = -\hbar g_m (\delta \hat{a} \hat{b}^\dagger + \delta \hat{a}^\dagger \hat{b}) \tag{2.30}$$

and identifies a process in which a photon is absorbed(emitted) in exchange for an emitted(absorbed) phonon, i.e., a beam-splitter interaction. On the other hand, the second term is

$$\hat{H}_{TMS} = -\hbar g_m (\delta \hat{a} \hat{b} + \delta \hat{a}^\dagger \hat{b}^\dagger) \tag{2.31}$$

and represents a two-mode squeezing since a photon and a phonon are created(annihilated) at the same time.

In giving this description, one should remember there is a third mode involved in the equations. In fact, the energy conservation principle implies that the energy before and after the interaction is the same, i.e., since phonons and photons carry different amounts of energy because of the different frequencies, the scattered photons must have higher or lower energy from the incoming one, constituting a separate optical mode. In our case, we are considering a linear cavity, and it has a frequency higher or lower than the first one, such as the difference between the two optical mode energy corresponds to the mechanical one, i.e., $\omega_1 - \omega_2 = \pm \Omega_m$.

To conclude this description, we report the optomechanical equations of motion (this time

also reporting the external field contributions) that are linearly coupled in the optical and acoustic field operators

$$
\begin{cases}
\dot{\hat{a}} = -\dfrac{\kappa}{2}\hat{a} + i\left(\Delta + \dfrac{g_0}{x_{\text{ZPF}}}\hat{x}\right)\hat{a} + \sqrt{\kappa_{ext}^{(1)}}\hat{a}_{in} \\
\dot{\hat{b}} = -\dfrac{\Gamma_m}{2}\hat{b} + i\Omega_m\hat{b} + g_0\hat{a}^\dagger\hat{a} + \sqrt{\Gamma_m}\hat{b}_{in}.
\end{cases}
\tag{2.32}
$$

3.1   From an optical resonator to an optomechanical cavity

In the previous chapter, we discussed a general framework to describe an optomechanical system, whereas, in the following two chapters, we start to focus on the actual physical system we use to realize the optomechanical interaction, i.e., a centimeter-scale crystal enclosed in an optical cavity. Before entering into the details of the optomechanical process arising from the interaction between light and the quartz crystalline structure, which is the main topic of the following chapter, we must develop a formalism to derive the optical response of the system from the simplified model of a Fabry-Pérot cavity. When we work in the bulk cavity optomechanics field, a macroscopic object is introduced in the optical system, and even neglecting the mechanical interactions, we still have to expand the depiction of a trivial two-mirror cavity.

In our experiment, the optomechanical system we analyze comprises a flat-flat z-cut quartz crystal of $L_q = 4\,\mathrm{mm}$ placed inside a $L = 10.23\,\mathrm{mm}$ flat-concave optical cavity with an offset $d \approx 1\,\mathrm{mm}$ as depicted in Figure 3.1. The two mirrors are shaped to confine the light inside
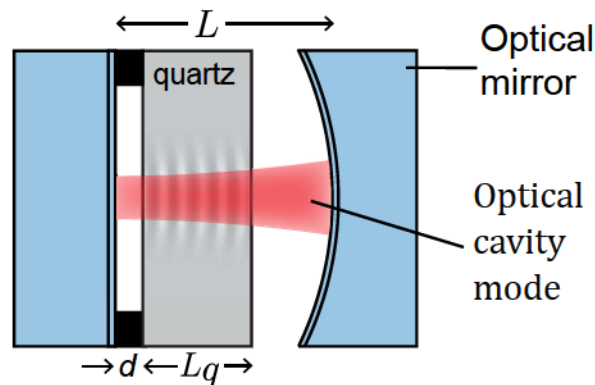

FIGURE 3.1: Scheme of the optomechanical cavity. Starting from a Fabry-Perot cavity composed of flat and curved mirrors with high reflectivity, we insert a flat-flat quartz crystal, affecting the resonance cavity modes. The resulting system enables to study of the crystal vibrational modes by coupling them to the optical field through Brillouin interactions. Image adapted from [32].

the resonator, and their high reflectivity enables a high-finesse optical cavity that enhances the electromagnetic field. Before providing a complete analysis of the changes in the optical response, one could intuitively understand that the optical spectrum must undergo some changes because the light must transit in a material with a higher refractive index n, thus increasing the optical length, slowing down the round-trip-time, and reducing the FSR of the optical cavity.

A closer look could give more insight into the new cavity behavior: the difference between the crystal and the surrounding refractive index is expected to usher some reflection at the crystal surfaces, impacting the steady state of the propagating field. Even neglecting the anisotropy of the crystal by using a polarized beam along one of the optical axes and the increased absorption inside the quartz and assuming perfect alignment between the crystal and the light direction of propagation, we still expect a considerable impact on the mode spacing. The 4.36-% reflectivity of the quartz-vacuum interfaces form several low-finesse cavities (see Figure 3.2) that are coupled between each other since the electromagnetic fields overlap [41]. Moreover, the constructed and destructive interference between the cavity fields will act differently at different frequencies, thus creating an asymmetric behavior among the resonant mode. In fact, we can anticipate that the presence and position of the crystal modulate the linewidth of the cavity modes and the spacing between them. The result is the creation of a so-called asymmetric cavity.

In the next section, we formalize the description of the optomechanical cavity using the scattering matrix approach. Despite being unable to give a complete closed-form relation, the description of the input-output relations is enough to justify the results provided in the final section of this chapter and numerically simulate the system response.

Uniform density of states in absence of crystal reflections
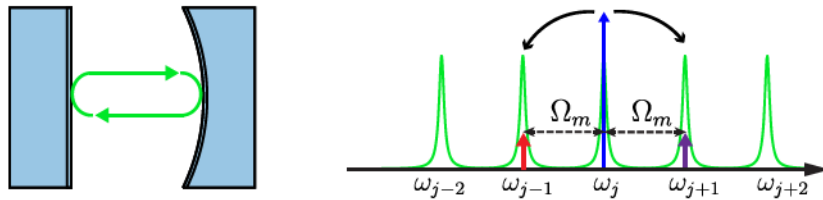
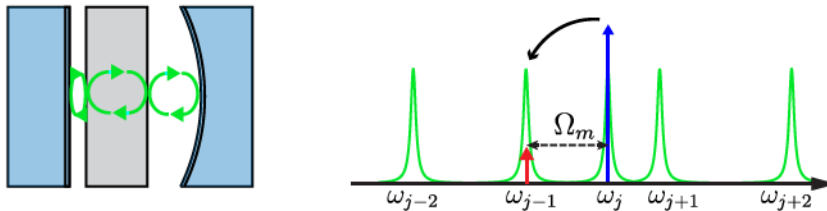Nonuniform density of states in presence of crystal reflections

FIGURE 3.2: The picture shows the main difference between an optical and an optomechanical cavity. Adding a crystal inside, the simple Fabry-Perot cavity on top becomes a three-cavity coupled system because of the crystal surface reflections. The uniform spectral response transforms into a nonuniform density of modes. The main advantage is the ability to resonate phenomena in the cavity, i.e., select the interaction Hamiltonian part under analysis and limit the interaction to only two optical modes. In the case of Brillouin scattering, we can thus suppress Stokes or Anti-Stokes scattering. Image adapted from [32].

3.2 Transfer matrix of a multi-cavity system

Suppose we focus only on the optical response of our optomechanical cavity. In that case, we can reduce the system complexity to a linear optical system composed of three optical cavities, one between the first mirror and the crystal, one within the crystal faces, and one between the crystal and the second mirror. One approach to deriving a comprehensive analysis of the system is the coupled cavity theory [42]. This theory wants to decouple the different cavity responses by considering all the possible light paths and analyzing them independently before superimposing the solutions to get the global response. It allows obtaining a closed-form analytical solution for the system, but the computations required for a three-cavity system are not trivial. A second approach widely used to analyze complex optical systems is deriving the system transfer matrix by analyzing the transmission matrix of each constituting element. Deriving a numerical characterization of the system frequency response is thus reduced to some matrix multiplication if we focus only on describing fields outside the optical cavity.

In deriving the transfer matrix of the asymmetric cavity, we assume plane wave propagation and a one-dimensional model for the beam propagation, as in the simple Fabry-Pérot cavity analysis. These assumptions lead to some limitations on the predictive ability of the model, as we will analyze in Chapter 7. Nevertheless, they provide meaningful insides into the behavior we aim for in our cavity. In the transfer matrix framework, we must define the input and output field amplitudes (with a classical light model) as $a_{in}^{(1,2)}$, and $a_{out}^{(1,2)}$ with the meaning reported in Figure 3.3 [32].
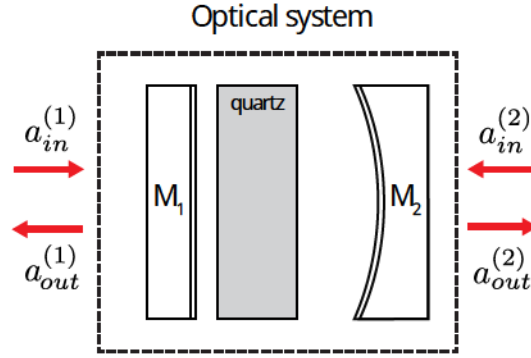

FIGURE 3.3: Scheme of the optical system. We can identify the input and output modes at the two ports $a_{in}^{(1,2)}$ and $a_{out}^{(1,2)}$ and define the transfer matrix T which completely characterize the system linear response.

The relation between the fields is given by the transfer matrix T as

$$\begin{pmatrix} a_{out}^{(1)} \\ a_{in}^{(1)} \end{pmatrix} = T \begin{pmatrix} a_{out}^{(2)} \\ a_{in}^{(2)} \end{pmatrix}, \qquad T_1 = \begin{pmatrix} s_{11}^{(1)} & s_{12}^{(1)} \\ s_{21}^{(1)} & s_{22}^{(1)} \end{pmatrix} \tag{3.1}$$

After analyzing the several elements of the cavity, we can identify two recurring relations that are expressed through the propagation matrix T_{prop}

$$T_{prop} = \begin{pmatrix} \gamma e^{i\phi} & 0 \\ 0 & \gamma e^{-i\phi} \end{pmatrix}, \qquad \phi = n\frac{\omega L}{c} \tag{3.2}$$

that represents the phase delay ϕ and the absorption γ of the electromagnetic field propagating through a material with thickness L and refractive index n (dependent on the oscillation frequency), and the interface matrix T_{ref}

$$T_{ref} = -\frac{i}{t} \begin{pmatrix} -1 & r \\ -r & 1 \end{pmatrix}, \qquad r = \frac{1-n}{1+n}, \qquad t = \sqrt{1-r^2} \tag{3.3}$$

which reports the phase and amplitude relation between the fields across an interface where r is the surface reflectivity and t is its transmissivity. We should remark that the transfer matrix method allows us to use the complete relation of the dielectric mirrors without characterizing the multilayer structure when placed in vacuum/air.

The total transmission matrix for our optical system consisting of the bulk crystal inside the Fabry-Pérot optical cavity is then given by

$$
\begin{aligned}
T =& T_{ref}(\text{mirror}_1)\, T_{prop}(\text{vacuum})\, T_{ref}(\text{quartz})\, T_{prop}(\text{quartz})\cdot \\
& \cdot T_{ref}(\text{quartz})^{\dagger}\, T_{prop}(\text{vaccum})\, T_{ref}(\text{mirror}_2) \\
=& \frac{-i}{t_1}\begin{pmatrix} -1 & r_1 \\ -r_1 & 1 \end{pmatrix}\begin{pmatrix} e^{i\phi_1} & 0 \\ 0 & e^{-i\phi_1} \end{pmatrix}\frac{-i}{t_0}\begin{pmatrix} -1 & r_0 \\ -r_0 & 1 \end{pmatrix}\begin{pmatrix} \gamma e^{i\phi_0} & 0 \\ 0 & \gamma e^{-i\phi_0} \end{pmatrix}\cdot \\
& \cdot \frac{-i}{t_0}\begin{pmatrix} -1 & -r_0 \\ r_0 & 1 \end{pmatrix}\begin{pmatrix} e^{i\phi_2} & 0 \\ 0 & e^{-i\phi_2} \end{pmatrix}\frac{-i}{t_2}\begin{pmatrix} -1 & r_2 \\ -r_2 & 1 \end{pmatrix}.
\end{aligned}
\tag{3.4}
$$

Here the first and second mirror reflectivities $r_{1,2} = \sqrt{R_{1,2}}$ and transmissivities $t_{1,2} = \sqrt{T_{1,2}}$ are obtained from the mirror characteristics, and the propagation phase delays are $\phi_0 = n\omega L_q/c$, $\phi_1 = \omega d/c$, and $\phi_2 = \omega(L - L_q - d)/c$. The optical power reflected $P_{out}^{(1)}$ and transmitted $P_{out}^{(2)}$ from the optical cavity can then be calculated from the total transmission matrix (3.4) and the input power $P_{in}^{(1)}$ as

$$
P_{out}^{(1)} = \left|\frac{T_{12}}{T_{22}}\right|^2 P_{in}^{(1)}, \qquad P_{out}^{(2)} = \left|\frac{1}{T_{22}}\right|^2 P_{in}^{(1)}.
\tag{3.5}
$$

3.3 Simulation of the optical properties of an optomechanical cavity

When we compare the simulated results of this optomechanical cavity with the Fabry-Pérot resonator, we can verify that the quartz crystal leads to significant modifications in the cavity's optical properties. Without the quartz crystal, the cavity modes are equally spaced based on the cavity length, and the free spectral range (FSR) follows a well-known pattern (see equation (2.2)). On the other hand, when the quartz crystal is inserted, the average spacing between the optical modes becomes narrower due to the increased optical path length caused by the crystal, and asymmetry in the mode spacing arises. In Figure 3.4, we report the simulated reflectance spectrum.

As we can recognize in the Figure, the FSR undergoes a modulation depending on the mode frequency, the cavity length, and the offset in the crystal position. When considering small changes in the crystal position, these variations are periodic with a period equal to half of the light wavelength (Figure 3.5). It results from the crystal surfaces passing through the nodes and antinodes of the standing wave optical cavity modes. If an asymmetric FSR is the most evident impact, we should underline that the mode linewidth and maximum transmission (i.e., minimum reflection) undergo the same modulation. Figure 3.6 displays the reflectance variations for some modes as a function of the crystal position inside the cavity, while Figure 3.7 shows the mode linewidth that undergoes the same modulation. Even in the ideal case of perfect alignment between the incoming beam and the standing wave along the cavity's central symmetry axis, a given mode can change its properties depending on the crystal displacement or mirror distance. This aspect will have a crucial impact on understanding the experimental results, where a slight misalignment of the entire structure limits the performance of the whole system [30].

Another remarkable note is related to the different behavior of the resonances depending on their frequency. In Figure 3.5, we can observe a diverse behavior for even and odd modes,
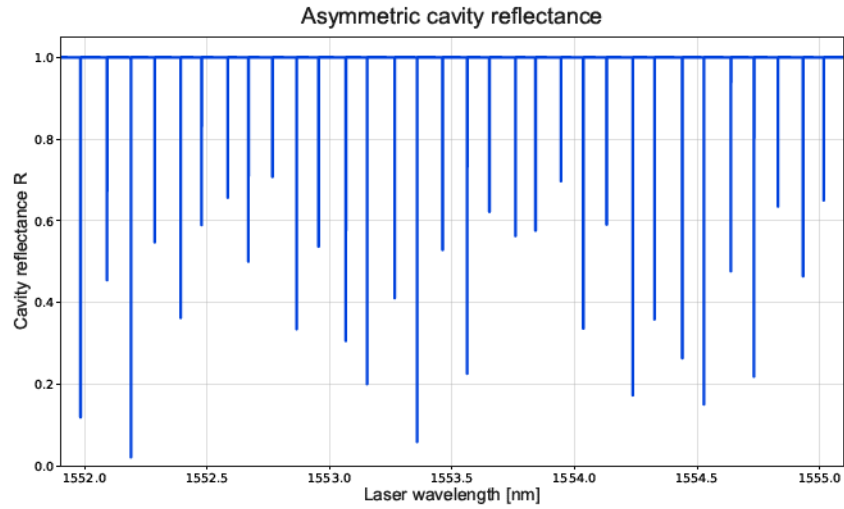
FIGURE 3.4: Simulated spectral response of the three-cavity system. The reflectance is aperiodic, with a difference in FSR between the modes and a different extinction ratio of the modes themselves. This behavior results from the constructive and destructive interference between the standing waves of the single cavity, leading to a modulation of the response.

where the amplitude and phase delay of the oscillations is different between the two. A justification for this behavior is not trivial, but it is probably related to having three coupled cavities between the two mirrors that could compensate for each other behavior. Once again, this consideration will help us understand the experimental data (Section 7.1) and, in particular, the effects of the crystal misalignment on the modes (Section 7.3).

Looking at the relation between the wavelength and the FSR (Figure 3.8), the difference between even and odd modes is again evident. Moreover, we can recognize a pattern formed by two sine waves of different amplitude, one modulating the odd modes and the other the
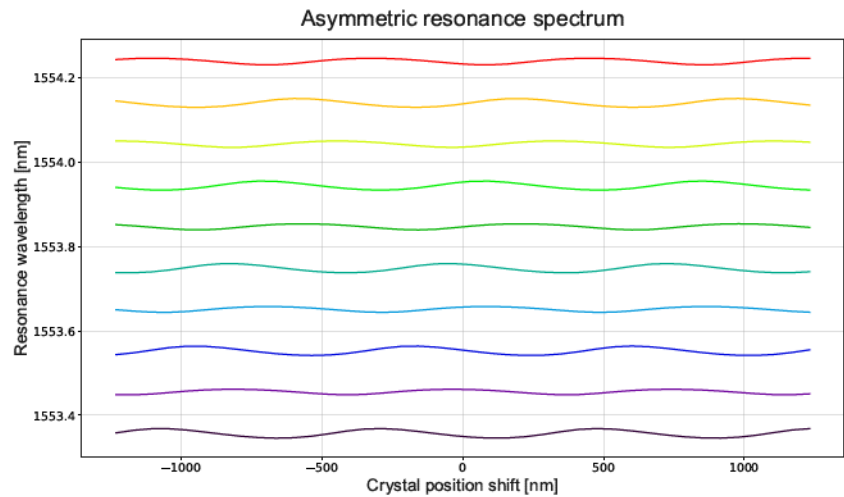

FIGURE 3.5: Simulation of the cavity resonant modes with different offsets in the crystal position. The frequencies are modulated because of the phase-matching condition on the crystal surface. Each mode has a different phase delay in the oscillation, but the period is constant and corresponds to half of the light wavelength.
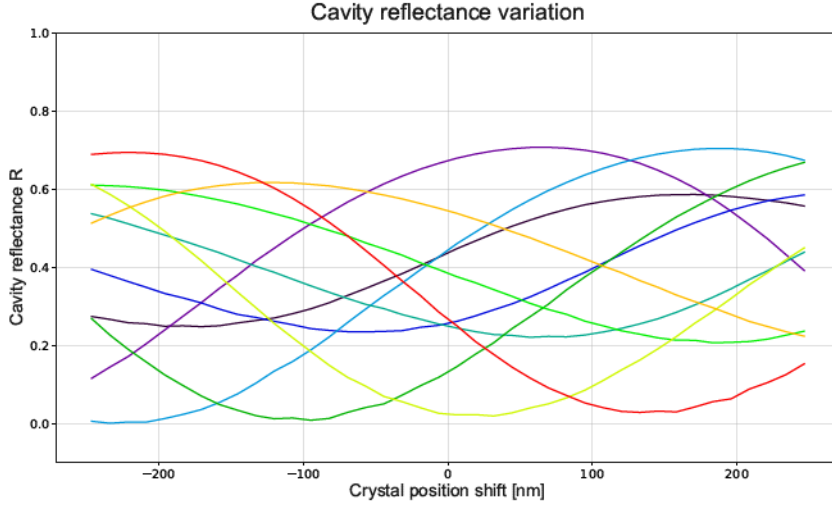
19

FIGURE 3.6: Simulation of the reflectance of 10 different modes. The maximum amount of light coupled inside the cavity depends on the specific mode (e.g, dark blue vs yellow) while the modulation of the peak height depends on the crystal position.

even ones. In the Figure, we can also notice how the crystal position affects the relative distance between the cavity modes that in practice enable a fine-tuning of the FSR. Most importantly, the variation speed depends on the position of the point on the modulating waveform: the top and bottom fringes are more stable than the central rapid drift of the FSR, enabling less altering, but better response stability [30]. If we analyze Figure 3.9 comparing FSR and ΔFSR, defined as the difference between two consecutive FSRs

$$\Delta\text{FSR} = FSR_{j+1} - FSR_j = w_{j+2} + w_j - 2w_{j+1}, \tag{3.6}$$

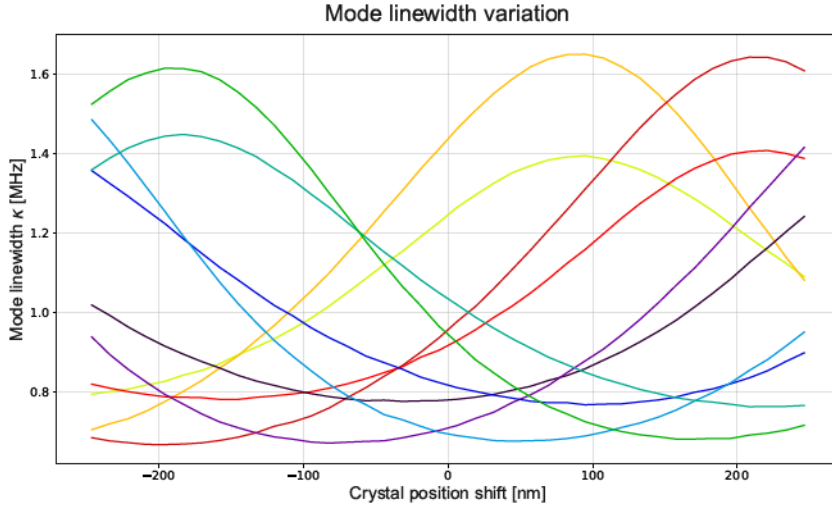FIGURE 3.7: Simulation of the mode linewidth as a function of the crystal offset. The peak height and width are related, so the same modulation affects both of them. When a peak is high, it is also narrow, and vice versa. The minimum and maximum depend on the specific cavity modes, however, the absolute minimum linewidth is related to the pure optical cavity one, since the crystal can only increase the losses.
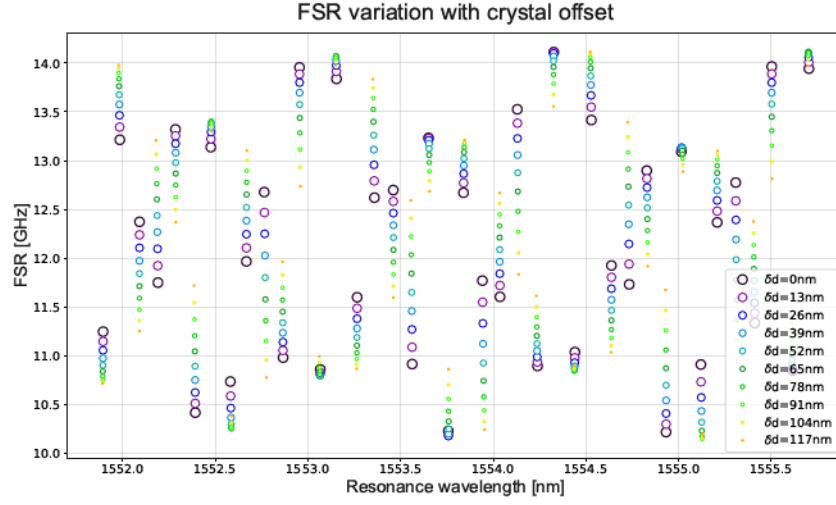
FIGURE 3.8: Simulation of the FSR as a function of the crystal offset inside the cavity and the resonance wavelength. The spectral response is modulated in frequency because of the crystal reflectivity, with a periodic envelope around an average value that is slightly smaller than the pure optical cavity one. The crystal position makes the pattern varies, with different drift speed with different modes. This drift is periodic and corresponds to the oscillation of the mode frequency reported in Figure 3.5.

we notice a double-elliptical pattern for the even and odd modes. The ellipse eccentricity depends on the crystal offset inside the cavity [31], and its axis drifts with the laser frequency (the phase delay on the crystal facets depends on the laser wavelength, thus the interference with the reflected wave drifts with it). Having ΔFSR $\neq 0$ allows exciting a single mode pair when stimulating the optomechanical response in the crystal (see Section 4.3).
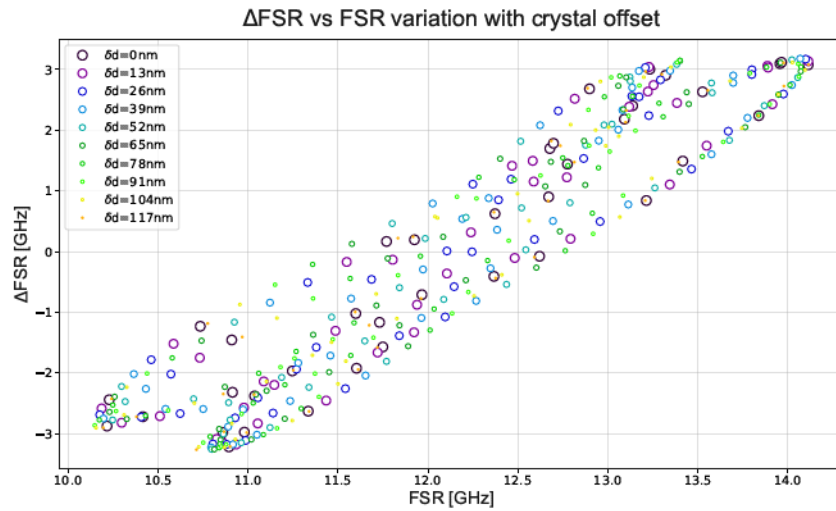

FIGURE 3.9: Simulation of the relation between consecutive FSRs as a function of the crystal position inside the cavity. The points are distributed along two ellipses which rotate with the frequency. The ellipticity depends on the macroscopic crystal position, with larger values closer to the mirrors. On the other hand, the microscopic crystal shifts make the points move along the ellipses.
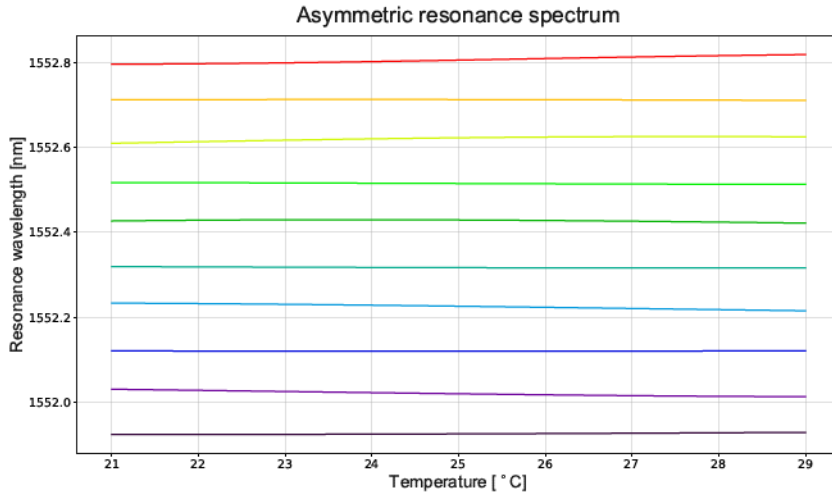
FIGURE 3.10: Simulation of the cavity resonant frequencies when the cavity temperature increases. Since the crystal and the cavity holder have different lengths and expansion coefficients, the crystal dimension, its offset, and the cavity length undergo superimposed changes. The picture shows the behavior over a typical operation range in the laboratory.

Finally, we should stress that the nanometric changes in the crystal position or cavity length are not outside the ability of a standard optics laboratory. Precisely, the metal expansion and contraction with temperature is more than enough to generate significant drifts in a room temperature setup. The ability to tune the system is enabled once we provide a strategy to modify and stabilize the temperature of the elements keeping the mirrors and the crystal in position.

In Figure 3.10, we report the same analysis of 3.5, but taking into account the thermal expansion coefficients of the quartz crystal and the brass cavity [43]. In fact, with the temperature rising, the cavity length increases as well as the length of the crystal and its
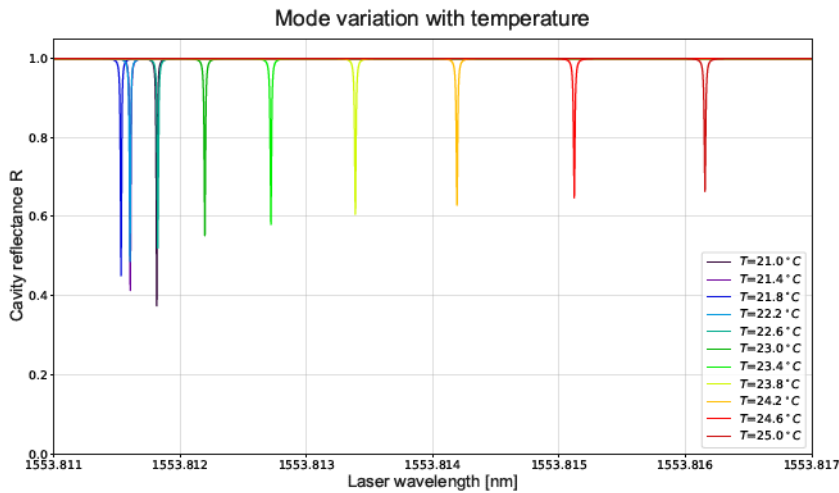

FIGURE 3.11: Example of a mode drift with temperature. The macroscopic drift depends on the cavity length variation because it is accumulated in frequency. At the same time, the crystal position and expansion mainly impact the mode shape and the inversion of direction on the left of the picture.
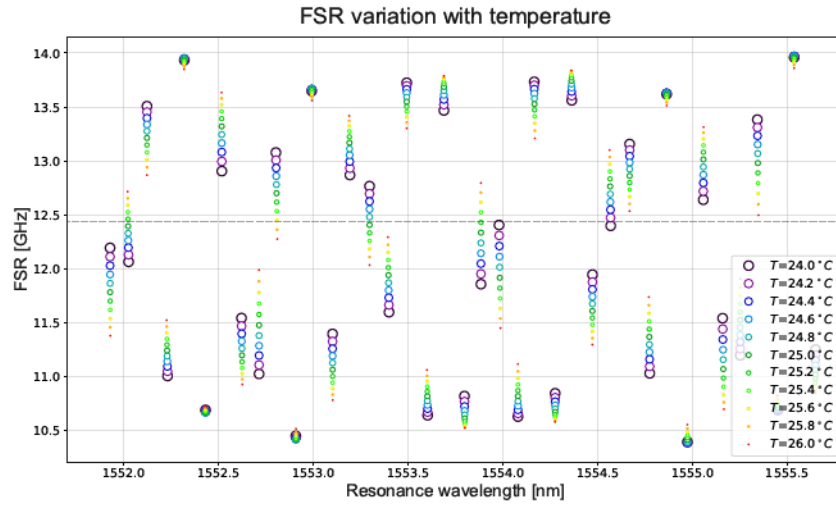
FIGURE 3.12: Simulation of the impact of temperature on the FSR pattern. Slow drifting points appear on the top and bottom of the modulation pattern, in accord with the sinusoidal oscillations of the points. The dotted line represents the Brillouin frequency we aim at to stimulate the optomechanical interaction. Regarding the points crossing the line, we show that temperature stability and control are required to steady the cavity behavior.

offset with respect to the first cavity mirror. In Figure 3.11, we displayed the mode frequency drift, dominated by the cavity length variation, together with the changes in its reflectance, caused by the crystal shift as shown in 3.6.

At last, in Figure 3.12 and Figure 3.13 we report the FSR behavior as a function of the cavity temperature. The same considerations as in the case of simple crystal position changes apply.
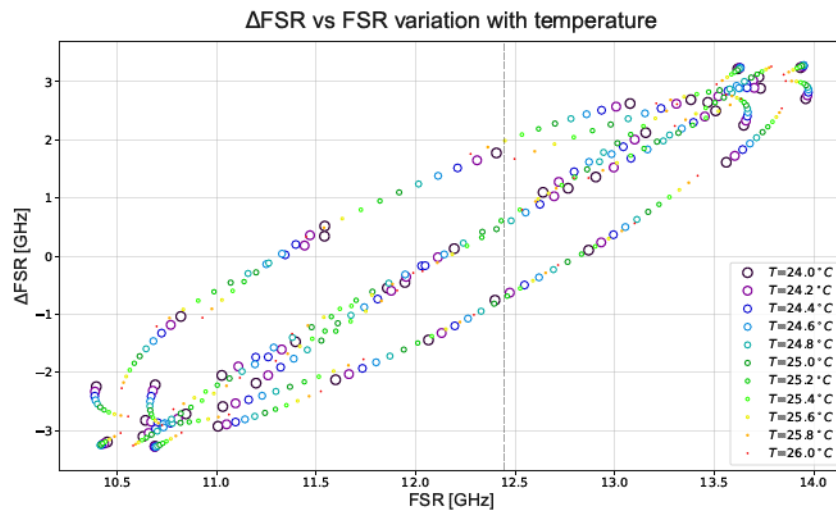
FIGURE 3.13: Simulation of the ΔFSR against FSR pattern as a function of the cavity temperature. The temperature impact is the same as the crystal offset since the phase-matching condition drifts with temperature while the macroscopic crystal position is stable, assuming good equilibrium among the thermal stress forces, i.e., the alignment of the crystal faces is not compromised.

23

In addition to anticipating the comparison between simulation and experimental data, this analysis wants to justify this setup's utility in studying the optomechanical response of the quartz crystal. In particular, the previous Chapter has clarified the requirements of having multiple optical modes separated by the vibrational frequency allowed by the crystal and a strategy to suppress part of the interaction to obtain recognizable Hamiltonians. In this Chapter, we demonstrated how both conditions are met when placing a crystal inside an optical cavity thanks to the modulation of the cavity's FSR and the ability to tune the system through temperature variations, thus providing a strong theoretical backing for the experiment.

Brillouin scattering 4

4.1 Light-matter interactions in a Quartz crystal

In the previous Chapter, we justify the choice of the experimental setup and how a macroscopic optomechanical cavity can be used to study the interaction between an optical and an acoustic mode. We will now focus on understanding how the acoustic wave can be generated inside a crystal and can enable optomechanical interaction to transfer power between different optical modes.

Starting from the material choice for the experiment, a quartz crystal is an arranged structure of Silicon and Oxygen atoms according to a hexagonal lattice. The crystalline structure has a refractive index $n = 1.5276$ @ $T = 298\,\mathrm{K}$ [44] and presents two optical axes, i.e., when the material is cut along the x-y plane (z-cut) and the light impinging orthogonally to the crystal face, twp linearly polarized modes can be transmitted without perturbation. On the other hand, the other incoming beams will be affected depending on the incoming polarization, with a deviation in the optical path if the impinging angle is different from zero. Nevertheless, quartz crystals are often used in optics because of their stability in frequency ($dn/d\lambda = -9\,\mathrm{ppm/nm}$) and temperature $dn/dT = 10\,\mathrm{ppm/K}$, and low absorption $\gamma < 10\,\mathrm{ppm/cm^{-1}}$ at optical wavelengths. Moreover, their birefringence $\Delta n = 8.47 \times 10^{-3}$ is usually neglected by operating along the crystal optical axis, as in this experiment.

In quantum optics, when discussing the optical properties of the different materials, we are often interested in the capability of arising non-linear phenomena because they imply the interaction between multiple quantum entities and thus enable, for example, the creation of entangled and squeezed light. Quartz crystals do not show remarkable high-order dielectric coefficients and can still favor Raman and Brillouin scattering. Raman scattering describes the properties of the atomic nuclei of absorbing and re-emitting photons at different energies after going through a transition of the bounded electrons to a different energy level. Brillouin scattering involves an acoustic wave propagating through the crystalline structure and an organized displacement of the lattice atoms.

Pristine quartz crystals are employed for their optomechanical properties because a precise lattice structure without defects and impurities enables the long propagation of vibration across the material and, when the system is cooled down to cryogenic temperature, can constitute a mechanical cavity with small linewidth ($\Gamma_m/2\pi = 100\,\mathrm{kHz}$ [32]). Furthermore, the acoustic modes are considered at high-frequency in the optomechanics field with bulk acoustic waves at about $\Omega_m/2\pi = 12.44\,\mathrm{GHz}$, allowing them to easily reach ground state for the mechanical oscillator at $T = 100\,\mathrm{mK}$ and involve a large motional mass of about

25

$m_{eff} \approx 20\,\mu g$, increasing the interest for fundamental physics experiments.

In the rest of the chapter, we will focus on the Brillouin interaction, starting with a phenomenological description of Stokes and Anti-stokes scattering to conclude by formalizing the interaction in the framework of Optomechanics we introduced in Chapter 2.

4.2 Brillouin interactions: Stokes and Anti-Stokes scattering

Among the energy-transfer mechanisms in quartz crystals, Brillouin scattering is the prominent optomechanical interaction (Figure 4.1). From a classic optics point of view, Brillouin scattering is a three-wave mixing interaction arising from the inelastic scattering of light from elastic waves, i.e., bulk acoustic waves. Brillouin scattering occurs due to electrostriction, a phenomenon where materials become denser under the influence of an electric field [45]. More in detail, the coupling between the optical field and the local displacement of the dielectric medium occurs through a Brillouin-like optomechanical process when the time-modulated electrostrictive optical force distribution, produced by the interference between distinct modes of the Fabry-Pérot cavity, matches the elastic profile (and frequency) of a bulk acoustic phonon mode. By creating a time-modulated photoelastic grating, these acoustic waves mediate energy transfer between distinct longitudinal modes of the optical cavity.

From the given definition, the requirement of exciting at least two optical modes which
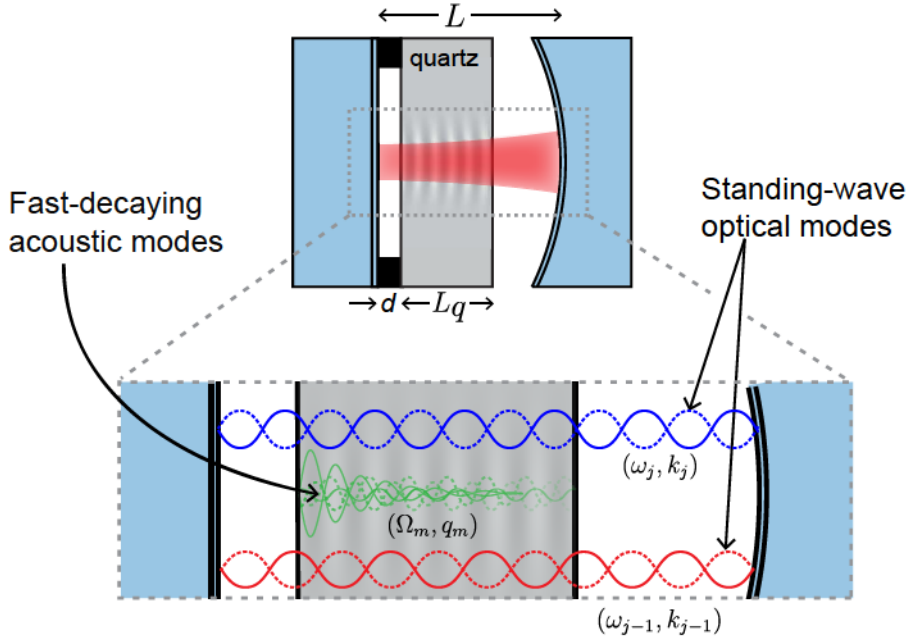
FIGURE 4.1: The picture shows the optical and acoustic modes inside the optomechanical cavity. The phase-matching conditions for acoustic modes generate standing waves between the two mirrors. When considering the reflection from the crystal too, the waves can show different intensities in the different regions because of constructive and destructive interference with the reflected fields. On the other hand, the phonon modes have a lifetime smaller than round-trip-time inside the crystal, preventing the creation of an acoustic cavity. The acoustic modes have fast decay rates and the phase-matching conditions are loosened. The interaction between the modes is allowed when energy and momentum conservation is guaranteed, and the overlapping integral between the modes is non-zero. Image adapted from [32].

spatially overlap within the crystal is evident. Moreover, energy and momentum conservation determines the set of phonon modes $(\Omega_m, \vec{q}_m)$ that can mediate resonant coupling between adjacent optical modes $(\omega_j, \vec{k}_j)$ and $(\omega_{j+1}, \vec{k}_{j+1})$ of the Fabry-Pérot cavity. When working at room temperature, we cannot create an acoustic cavity within the crystal because of the quick decoherence of the lattice vibrations $(\exp(-\Gamma_m L_q) \ll 1)$. The result is that these conditions are easily met, i.e., the linewidth of the cavity resonances can be much smaller than the mechanical linewidth of the optomechanical interaction. Moreover, assuming propagation of the optical beam orthogonal to the z-cut facet, the conservation of energy and momentum

$$\begin{cases} \hbar\omega_{j+1} = \hbar\omega_j + \hbar\Omega_m \\ \vec{k}_{j+1}(\omega_{j+1}) = \vec{k}_j(\omega_j) \pm \vec{q}_m(\Omega_m) \end{cases} \tag{4.1}$$

is satisfied when the frequency spacing between adjacent optical resonances matches the Brillouin frequency (FSR $= \Omega_m$), i.e., the acoustic wave frequency.

Considering these requirements, the Brillouin frequency Ω_m can be calculated as a function of the propagation speed of light v_o and sound v_a in the material [46]

$$\Omega_m = \frac{2\omega_p v_a/v_o}{1 \pm v_a/v_o} \approx 2\omega_p v_a/v_o, \tag{4.2}$$

where $\omega_p = \omega_j \approx \omega_{j+1}$ is the frequency of the laser pump, and the plus-sign takes into account the different directions of propagation of the acoustic waves compared to the optical ones as the given approximation is valid with $v_o \gg v_a$. The speed of sound in the longitudinal direction is $v_a = \sqrt{c_{33}/\rho}$, where $\rho = 2650 \, \text{kg/m}^3$ is the density, and $c_{33} = 106.1 \times 10^9 \, \text{Nm}^{-2}$ is the relevant elastic constant. The speed of light in a given material, $v0 = c/n$ where the refractive index n depends both on the pump wavelength $\lambda \approx 1550 \, \text{nm}$ and the temperature, and it is found using the Sellmeier formula [47]. The Brillouin frequency for crystalline z-cut quartz is estimated at $\Omega_m = 12.47 \, \text{GHz}$.
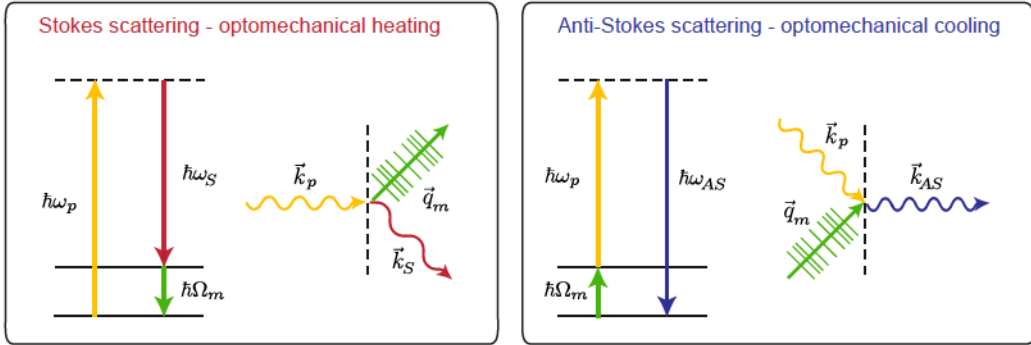
FIGURE 4.2: Energy and momentum conservation diagram for Stokes and Anti-Stokes processes. In Stokes scattering, a high-energy photon interacts in the material, releasing a new phonon that propagates across the lattice structure and a lower-energy photon. In Anti-Stokes scattering, a photon and a phonon interact together and emit a new higher energy photon. The two interactions are known as optomechanical heating and cooling because they impact the number of phonons in the system, thus changing its thermal equilibrium.

Since two conditions can define Brillouin interactions, two different processes involving the three waves can arise, i.e., Stokes and Anti-stokes scattering. In a Stokes process, a photon from the incident laser pump field at frequency ω_p is converted into a lower frequency Stokes photon at frequency ω_S and an acoustic phonon at frequency Ω_m in the inelastic scattering process, where $\omega_p = \omega_S + \Omega_m$, shown in Figure Figure 4.2 (left). On the other hand, a photon from the laser field can also absorb the energy of an acoustic phonon and

FIGURE 4.3: The dispersion relations between the optical and acoustic modes imply that the scattered field is always back-propagating with respect to the pump mode. On the other hand, the generated Stokes phonons differ from the ones that can be absorbed through Anti-Stokes scattering because of the different directions of propagation. We should also notice that the momentum of the interacting phonons q^+ and q^- is slightly different because of the dependence on $N_{th} + 1$ and N_{th}, respectively. Image from [31].
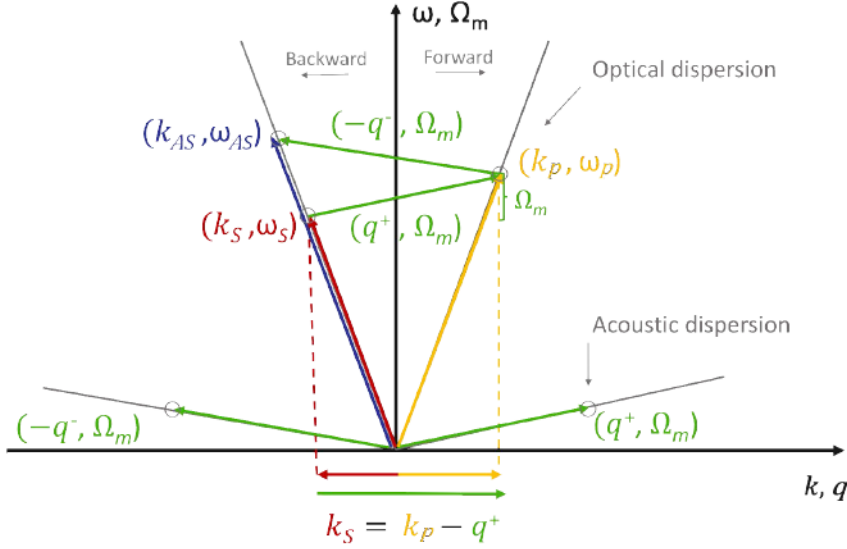
produce a higher frequency anti-Stokes photon at frequency $\omega_{AS} = \omega_p + \Omega_m$, as shown in Figure Figure 4.2 (right). To grant momentum conservation, the two interactions generate respectively forward- and backward-propagating phonon waves known as forward and backward Brillouin scattering. Figure 4.3 pictures the dispersion relation of the different waves, and it provides a graphical explanation for the difference between the Stokes q^+ and Anti-stokes q^- momentum at the same frequency Ω_m.

An additional remark should include the phase-matching conditions between the generated waves: only if the pump wave coherently excites the crystal, the resulting photons will be able to constructively interfere with each other in the interaction region and generate a propagating scattered wave [45, 48]. It is indeed the case inside an optical cavity, where the pump mode is in a steady state because of resonance with the cavity modes.

4.3 Optomechanical description in the scattering picture

If, in the previous section, we have described the Brillouin scattering and its interpretation through optical and acoustic waves, we are still missing the theoretical link with an optomechanical interaction. An intuitive explanation could recall that Brillouin scattering implies the energy exchange between an optical and an acoustic wave, thus complying with the definition of optomechanical interaction. Nevertheless, a more precise analysis of the results shown in Chapter 5 can draw a complete picture of both interpretations of the phenomenon.

We have shown that we can distinguish the two-mode squeezing and the beam-splitter interactions by suppressing part of the linearized optomechanics interaction Hamiltonian. These two processes are equivalent to Stokes and Anti-stokes scattering, respectively, once described as single energy quantum transfer (Figure 4.4). In fact, the decay of a single high-energy photon into an entangled state between a photon and a phonon clearly describes
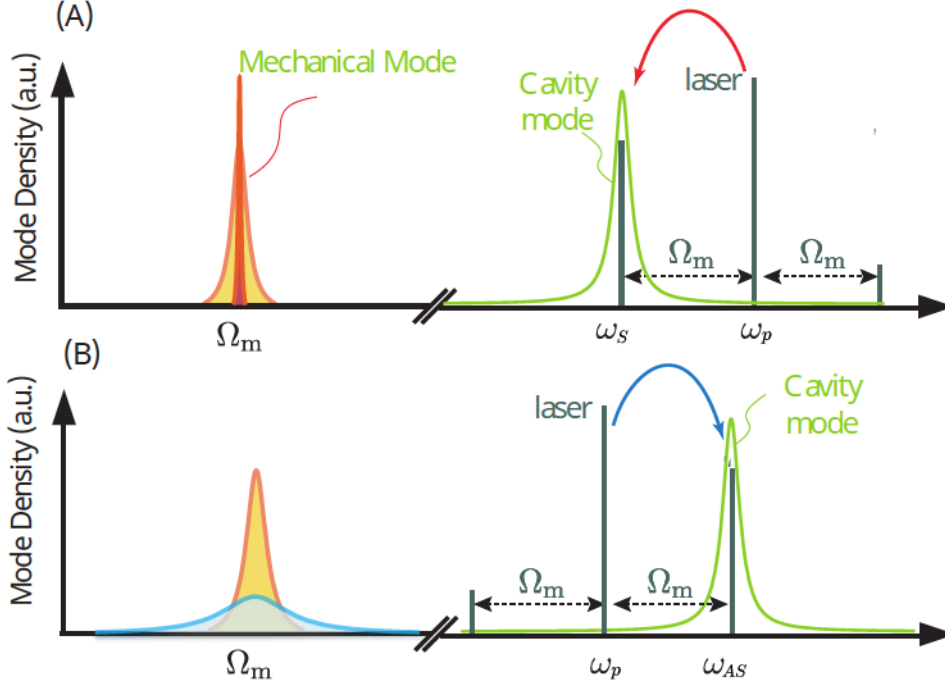
FIGURE 4.4: The diagram displays the Stokes (A) and Anti-Stokes (B) interactions, remarking on the role of the mechanical and optical modes. When we neglect the pumping laser that could have a higher or lower frequency compared to the optical cavity mode, the power is always scattered into the cavity mode. The difference lies in the narrowing or spreading of the mechanical state distribution because of the creation or absorption of phonons at a precise frequency. Image from [19].

Stokes scattering, and its interaction Hamiltonian

$$\hat{H}_S = -\hbar g_0 (\hat{a}_p^\dagger \hat{a}_S \hat{b} + \hat{a}_p \hat{a}_S^\dagger \hat{b}^\dagger) \tag{4.3}$$

is equivalent to the probabilistic generation of a two-mode squeezed state (2.31), where the probability is given by the strength of the optomechanical interaction g_0. In the same way, Anti-stokes scattering relies on the probabilistic absorption of a phonon, together with a photon, to create a higher energy photon and constitute a beam splitter interaction when neglecting the pump mode providing energy for the transition

$$\hat{H}_{AS} = -\hbar g_0 (\hat{a}_p^\dagger \hat{a}_{AS} \hat{b}^\dagger + \hat{a}_p \hat{a}_{AS}^\dagger \hat{b}). \tag{4.4}$$

The parallelism is also evident after recalling that the acoustic waves in a system are directly proportional to its temperature, thus the creation of phonon through Stokes scattering heats the mechanical system while the absorption through Anti-stokes scattering cools the system down. When recalling that the two optomechanical interactions are indeed named laser heating and laser cooling because of their effect on the amplitude of the displacement of the mechanical oscillator, the equivalence is once again confirmed.

Furthermore, we can calculate the optomechanical single-photon coupling rate g_0 of the Brillouin interaction. The derivation actually requires introducing the quantization of the electromagnetic and acoustic fields and taking into account both the mode overlap of the Gaussian beams inside the crystal and the phase-matching condition because of the standing optical modes nodes and antinodes. The complete derivation can be found in the literature articles [32], while here we report only the upper limit for g_0 (noting that it assumes an

29

acoustic cavity being formed inside the crystal) as

$$g_0/2\pi \approx \frac{\omega n^5 p_{13}}{2n_{eff}^2 c} \sqrt{\frac{\hbar}{\Omega_m \rho A L_q}} \left(\frac{L_q}{L}\right), \tag{4.5}$$

where $n_{eff} \approx n = 1.5276$ is the effective refractive index for the optical mode, $\rho = 2650\,\text{kg/m}^3$ is the material density, $p_{13} = 0.27$ is elasto-optic constant along the optical axis, $A \approx \pi(72\,\mu\text{m})^2$ is the interaction area constrained by the optical mode waist, $L_q = 4\,\text{mm}$ is the crystal length, and $L = 10.23\,\text{mm}$ is the cavity length. We have also assumed the frequency of the two optical modes to be the same $\omega_j = \omega_{j+1} = \omega = 193.4\,\text{THz}$ to obtain a maximum single-photon coupling rate of $g_0/2\pi \approx 12.98\,\text{Hz}$.

In conclusion, in these introductory chapters, we discussed the theory behind the optomechanical interactions and its equivalence with the Brillouin Stokes and Anti-stokes scattering happening in quartz crystal, showing its feasibility as an optomechanics platform. Moreover, we explain how the interactions can be stimulated independently in a macroscopic optomechanical cavity thanks to the modulation in the FSR when placing a crystal inside the cavity, and we are now ready to describe the experiment and its goal.

5.1 High-frequency optomechanics: resolved-sideband regime

The topic of this project could be said to be within the "bulk cavity optomechanics" because of the macroscopic nature of the optomechanical system compared to the more commonly used membranes and trampolines. The "cavity" feature arises from using the resonant modes of an optical cavity to enhance the optomechanical interactions in the quartz crystal. Another classification could be discerned from the nature of the interaction given the topic name of "Brillouin optoacoustics" since the lattice vibrations generated by Brillouin-scattered phonons lead to bulk acoustic waves propagating in the crystal. Finally, another characterization of the system under analysis is the property of allowing "high-frequency phonons". In fact, "high-frequency optomechanics" denominates a specific subfield focused on studying the optomechanical interactions within the limits of the resolved-sideband regime.

In contrast with the Doppler regime, i.e., the unresolved-sideband regime, in which the frequency of the mechanical modes is several orders of magnitudes smaller than the optical linewidth ($\Omega_m \ll \kappa$), thus limiting the cooling rate of the optomechanical interaction because of quantum back-action [19, 49], the resolved-sideband regime presents a mechanical
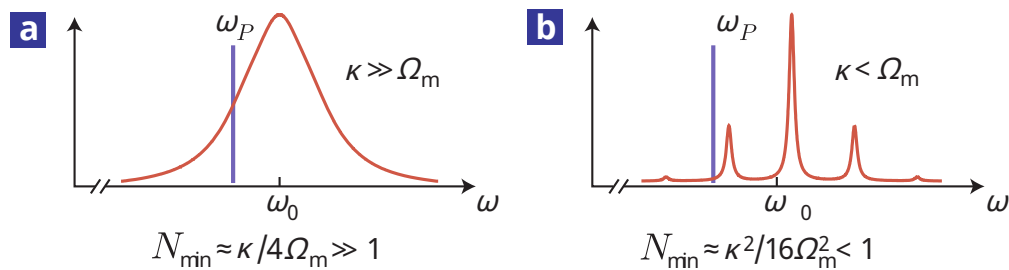
FIGURE 5.1: Comparison between unresolved (a) and resolved (b) sideband regime. In the first case, the stimulation of the sideband also transfers energy into the principal mode, preventing the cooling of the system into the mechanical ground state. In the second case, the separation between the sidebands allows exciting only the Anti-Stokes interaction, thus decreasing the phonon number and cooling the system below the single-phonon level $N_{min} < 1$. We also noticed that we could have high-order sidebands, but their strength is usually too low to be used. Image from [49].

frequency much larger than the cavity decay rate ($\Omega_m \gg \kappa$), as shown in Figure 5.1. In this regime, the optomechanical scattering generates a series of sideband peaks spaced at multiples of the mechanical frequency (only the first order is usually considered, in particular with a low optomechanical coupling rate) that are separated from the pumping mode peak. In this experiment, the advantage is evident: we not only can analyze the frequency response of these modes independently of the main one by filtering the spectral response, but we also can make both pumping and scattered beams in resonance with the cavity modes, increasing the number of photons in the pump that are available for the transition. The latter aspect is crucial for the experiment because it allows the system to reach the incredibly high effective coupling rate and reach the strong-coupling regime, i.e., the coupling rate overcomes the optical and mechanical losses inside the cavity, as it will largely explain at the end of this chapter.

In the following sections, we will formalize the Hamiltonian description of the optomechanical interaction in our system to derive a theoretical model of the variation in the optical response in terms of light intensity reflected from and transmitted through the cavity. Then, we will analyze the effects of power for the Stokes and the Anti-stokes interaction, defining and characterizing the Brillouin lasing and the strong-coupling regime.

5.2 Optomechanically Induced Amplification (OMIA) and Transparency (OMIT)

The optomechanical response of the system affects the optical properties of the cavity, leading to a change in reflectivity when the Brillouin frequency matches the difference between the two cavity modes. As we discussed before, the transfer of energy between the optical modes through the acoustic wave arises in a change of the reflected and transmitted power. In particular, in the case of a strong control laser in resonance with a cavity mode (pump mode), we can perturb the response of a weak probe in an adjacent resonance (signal mode), impacting the transmittance of the optical cavity. It is the so-called optomechanically induced amplification and transparency (Figure 5.2).
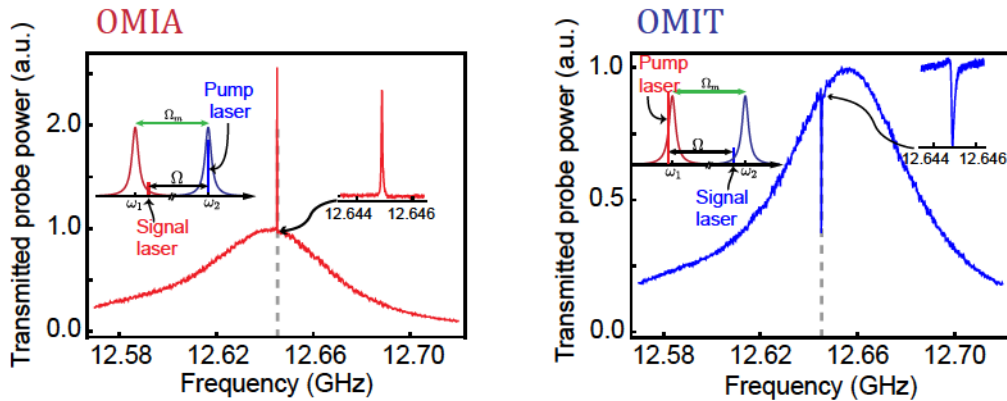
FIGURE 5.2: Optomechanically Induced Amplification (OMIA) and Transparency (OMIT). When analyzing the transmission of the signal mode, mechanical resonances impact the transmission of the optical mode because of the scattering of photons from the pump, which interferes constructively or destructively with the probing mode. If the system is at cryogenic temperatures and an acoustic cavity is formed, the mechanical linewidth can be much smaller than the optical one, leading to an amplification or absorption window in the cavity response. Image adapted from [32].

When the frequency of the probe mode is lower than the pump one, the power transfer is carried out through Stokes scattering, thus amplifying the amount of power inside the cavity and overcoming the mode decay. It means that, despite most of the light being transmitted through the optical cavity because in resonance with the cavity modes, part of the light is still reflected as if the reflectance of the cavity is increased and its amount is comparable to the incident intensity leading to a visible change in the spectral response. In the same way, when the probe mode has a higher frequency than the pump, it is depleted because of Anti-stokes interaction. In fact, the scattered photons are phase-coherent with the probe fields and destructively interfere with them, leading to a cancellation of the intracavity field. As a result, we no longer have a reflected light from the cavity that can interfere with the impinging one, transforming the cavity response as the one encountered out of resonance, i.e., the light appears to be transmitted through the cavity as the cavity resonance is made transparent. From an optomechanical point of view, the physical origin of both the amplification and the transparency windows underlies the beating between the probe field and the pumping laser that, when coherent, induces a time-varying radiation pressure force. When the mechanical oscillation frequency is met, the mechanical oscillator is driven resonantly, creating sidebands in the intracavity field that interfere constructively or destructively with the probe signal. Even if amplification and transparency can be described with the same set of equations in the theoretical discussion, the dumping of the mechanical oscillator in the Stokes scattering will be reduced by increasing the pump power. This aspect leads to an intrinsic limit for a coherent response before parametric oscillatory instability occurs, i.e., the noise is coherently amplified by the mechanical motion overcoming the lasing threshold.

5.3 Optomechanical cavity spectral response model

In trying to characterize the optomechanical response of our system, we should start by detailing the unidimensional transfer matrix model presented in Chapter 3. To have a more accurate description of the experimental results, we need to take into account another fundamental element. Whereas the modes $a_{in}^{(1,2)}$ and $a_{out}^{(1,2)}$ in (3.1) represent the input and output modes of the cavity, those do not, in general, describe the input and output modes of our transmission optics. Even if the difference in polarization alignment can be overlooked and the complete modeling of the misalignment of the incoming beam is an overreaching approach, we can still account for the mode mismatch through additional losses between the
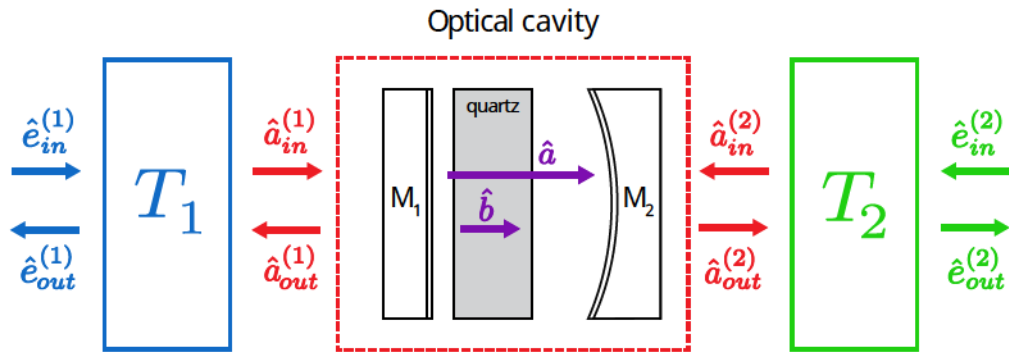
FIGURE 5.3: The scheme identifies the input $a_{in}^{(1,2)}$ and output $a_{out}^{(1,2)}$ modes from the optical cavity. These modes directly couple inside the cavity with the steady-state field $\hat{a}$. However, if we consider the mode-matching conditions, we must take into account the difference between them and the free-space optical modes $\hat{e}_{in}^{(1,2)}$ and $\hat{e}_{out}^{(1,2)}$ that can be collected and measured through the two interface matrices T_1 and T_2, i.e., coupling loss terms.

free-space optical modes and the cavity inputs and outputs [30]. Without loss of generality, we can thus define a real scattering matrix modeling the coupling coefficients between the modes. When we keep the denomination "1" for the port of the impinging laser and "2" for the one after the cavity, we define external modes $\hat{e}_{in}^{(1,2)}$ and $\hat{e}_{out}^{(1,2)}$, the input cavity modes $\hat{a}_{in}^{(1,2)}$, the output cavity modes $\hat{a}_{out}^{(1,2)}$ as reported in Figure 5.3. We also keep the same name for the optical pump $\hat{a}_p$ and signal $\hat{a}_s$ and mechanical $\hat{b}$ modes inside the cavity.
We can thus define the scattering matrix T_1 and T_2 as

$$
\begin{pmatrix} \hat{e}_{out}^{(1)} \\ \hat{a}_{in}^{(1)} \end{pmatrix} = T_1 \begin{pmatrix} \hat{e}_{in}^{(1)} \\ \hat{a}_{out}^{(1)} \end{pmatrix}, \qquad T_1 = \begin{pmatrix} s_{11}^{(1)} & s_{12}^{(1)} \\ s_{21}^{(1)} & s_{22}^{(1)} \end{pmatrix}
$$
$$
\begin{pmatrix} \hat{e}_{out}^{(2)} \\ \hat{a}_{in}^{(2)} \end{pmatrix} = T_1 \begin{pmatrix} \hat{e}_{in}^{(2)} \\ \hat{a}_{out}^{(2)} \end{pmatrix}, \qquad T_2 = \begin{pmatrix} s_{11}^{(2)} & s_{12}^{(2)} \\ s_{21}^{(2)} & s_{22}^{(2)} \end{pmatrix}
$$

(5.1)

where we assume $\langle \hat{e}_{in}^{(2)} \rangle = 0$, i.e., no optical field coupled from the second port, and $s_{22}^{(1,2)} = 0$, i.e., no further reflection of the output beams, to simplify the analysis. The normalized reflection $R_1(\Delta)$ and transmission $T_2(\Delta)$ optical spectra are then given as in (3.5) by

$$
R_1(\Delta) = \frac{\langle \hat{e}_{out}^{(1)\dagger} \hat{e}_{out}^{(1)} \rangle}{\langle e_{in}^{(1)\dagger} e_{in}^{(1)} \rangle}, \qquad T_1(\delta) = \frac{\langle \hat{e}_{out}^{(2)\dagger} \hat{e}_{out}^{(2)} \rangle}{\langle e_{in}^{(1)\dagger} e_{in}^{(1)} \rangle}
$$

(5.2)

with $\Delta = \omega - \omega_0$ the detuning of the optical signal compared to the resonance frequency ω_0. Recalling the Hamiltonians (2.25)(2.28) displayed in Chapter 2 and adapting them to take into account the several fields interacting with the cavity (Figure 5.4), we can rewrite the optomechanical Hamiltonian as

$$
\begin{aligned}
\hat{H} =& \hbar \left(i\frac{\kappa_p}{2} - \omega_p \right) \hat{a}_p^\dagger \hat{a}_p + \hbar \left(i\frac{\kappa_s}{2} - \omega_s \right) \hat{a}_s^\dagger \hat{a}_s + \hbar \left(i\frac{\Gamma_m}{2} + \Omega_m \right) \hat{b}^\dagger \hat{b} \\
&- \hbar g_m(\hat{a}_p^\dagger \hat{a}_s \hat{b} + \hat{a}_p \hat{a}_s^\dagger \hat{b}^\dagger + \hat{a}_p^\dagger \hat{a}_s \hat{b}^\dagger + \hat{a}_p \hat{a}_s^\dagger \hat{b}) \\
&+ i\hbar \sqrt{\kappa_{ext,p}^{(1)}} \alpha_{in,p}^{(1)} (\hat{a}_p^\dagger e^{-i\omega_p t} + \hat{a}_p e^{i\omega_p t}) + i\hbar \sqrt{\kappa_{ext,s}^{(1)}} \alpha_{in,s}^{(1)} (\hat{a}_s^\dagger e^{-i\omega_s t} + \hat{a}_s e^{i\omega_s t}),
\end{aligned}
$$

(5.3)

where we use the plane-wave approximation for the classical fields outside the optical cavity $\alpha e^{-i\omega t}$. Moreover, within the undepleted pump approximation, the dynamics of the mode at frequency ω_p are not influenced by the optomechanical coupling, and its Langevin equation of motion is

$$
\dot{\hat{a}}_p = - \left(i\omega_p + \frac{\kappa_p}{2} \right) \hat{a}_p + \sqrt{\kappa_{ext,p}^{(1)}} \alpha_{in,p}^{(1)} e^{-i\omega_p t}
$$

(5.4)

where $\kappa_x = \kappa_{ext,x}^{(1)} + \kappa_{0,x}$, $\kappa_{ext,x}^{(1)}$ is the loss rate at the first cavity mirror and $\kappa_{0,x}$ is the loss rate inside the cavity for the optical mode $x = p, s$. At the same time, we can adapt (2.12) to rewrite the steady state solution for mode $\hat{a}_p$

$$
\alpha_p = \sqrt{N_p} e^{-i\omega_p t} = \left| \frac{\sqrt{\kappa_{ext,p}^{(1)}} \alpha_{in,p}^{(1)}}{\kappa_p/2 + i\Delta_p} \right| e^{-i\omega_p t},
$$

(5.5)

where $N_p = |\alpha_p|^2 = \langle \hat{a}_p \rangle$ is the pump laser intra-cavity photon number for mode, and $\Delta_p = \omega_p - \omega_{0,p}$ is the pump detuning.
Following the same procedure presented in Section 2.4 and using the rotating frame of the pump laser, we can linearize the effective Hamiltonian respectively into two expressions for Stokes and Anti-stokes (with the only difference lying in the different use of the creation and
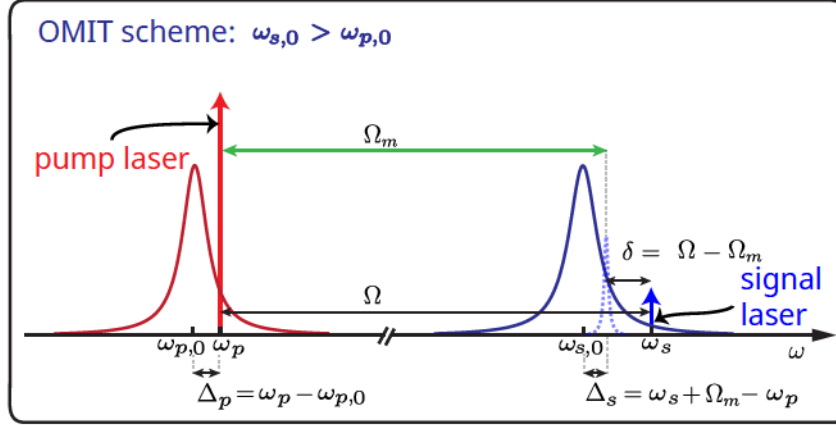
FIGURE 5.4: The scheme represents the several quantities impacting the OMIT response of the system. We usually assume driving the pump laser on resonance $\omega_p = \omega_{p,0}$, thus the main two parameters are Δ_s which represents the difference between the cavity mode frequencies and the Brillouin frequency Ω_m, and δ which is the detuning or the probing signal from the Brillouin frequency. Image adapted from [32].

annihilation operators)

$$\hat{H}_S = -\hbar\delta\hat{b}_m^\dagger\hat{b}_m - \hbar(\delta - \Delta_s)\delta\hat{a}_s^\dagger\hat{a}_s - \hbar g_m(\hat{a}_s\hat{b}_m + \hat{a}_s^\dagger\hat{b}_m^\dagger) + i\hbar\sqrt{\kappa_{ext,s}^{(1)}}\alpha_{in,s}^{(1)}(\hat{a}_s^\dagger - \hat{a}_s)$$

$$\hat{H}_{AS} = -\hbar\delta\hat{b}_m^\dagger\hat{b}_m - \hbar(\delta - \Delta_s)\delta\hat{a}_s^\dagger\hat{a}_s - \hbar g_m(\hat{a}_s^\dagger\hat{b}_m + \hat{a}_s\hat{b}_m^\dagger) + i\hbar\sqrt{\kappa_{ext,s}^{(1)}}\alpha_{in,s}^{(1)}(\hat{a}_s^\dagger - \hat{a}_s)$$

(5.6)

where $\delta = \omega_s - \omega_p - \Omega_m$ and $\Delta_s = \omega_{s,0} - \omega_p - \Omega_m$, and the cavity field-enhanced coupling rate $g_m = g_0\sqrt{N_p}$.
The Langevin linearized equations of motions are derived as

$$\begin{cases} \dot{\hat{a}}_s = -\dfrac{\kappa_s}{2}\hat{a} + i(\delta - \Delta_s)\hat{a} + ig_m\hat{b}_m^{(\dagger)} + \sqrt{\kappa_{ext,s}^{(1)}}\alpha_{in,s}^{(1)} \\ \dot{\hat{b}} = -\dfrac{\Gamma_m}{2}\hat{b} + i\delta\hat{b} + ig_m\hat{a}^{(\dagger)} \end{cases}$$

(5.7)

and the photon and phonon steady-state population is expressed as

$$\begin{cases} \hat{b}_m = \dfrac{ig_m}{\frac{\Gamma_m}{2} - i\delta}\hat{a}^{(\dagger)} \\ \hat{a}_s = \dfrac{\sqrt{\kappa_{ext,s}^{(1)}}\alpha_{in,s}^{(1)}}{-i(\delta - \Delta_s) + \frac{\kappa_s}{2} \mp \frac{g_m^2}{\Gamma_m/2 - i\delta}} \end{cases}$$

(5.8)

where the notation $(\dagger)$ remarks that the construction operation is used for the Stokes response while the annihilation one is for the Anti-stokes, in addition to the different $\mp$ sign.
Finally, we can write the complete expression for the output optical fields $\hat{a}_{out,s}^{(1)}$ and $\hat{a}_{out,s}^{(1)}$ at the two ports using (2.8)(2.9)

$$\hat{a}_{out,s}^{(1)} = \hat{a}_{in,s}^{(1)} - \sqrt{\kappa_{ext,s}^{(1)}}\hat{a}_s = \alpha_{in,s}^{(1)}\left(1 - \frac{\kappa_{ext,s}^{(1)}}{\frac{\kappa_s}{2} - i(\delta - \Delta_s) \mp \frac{g_m^2}{\Gamma_m/2 - i\delta}}\right)$$

(5.9)

$$\hat{a}_{out,s}^{(2)} = \sqrt{\kappa_{ext,s}^{(2)}}\hat{a}_s = \alpha_{in,s}^{(1)}\frac{\sqrt{\kappa_{ext,s}^{(1)}\kappa_{ext,s}^{(2)}}}{\frac{\kappa_s}{2} - i(\delta - \Delta_s) \mp \frac{g_m^2}{\Gamma_m/2 - i\delta}}$$

(5.10)

where the difference between OMIA and OMIT is in the sign $\mp$. For the external optical fields, we can report the transmittance and reflectance as the normalized reflected and transmitted power of the signal mode from (5.1)

$$
\begin{aligned}
R_1(\delta) &= \left| s_{12}^{(1)} s_{21}^{(1)} \frac{a_{out,s}^{(1)}(\delta)}{a_{in,s}^{(1)}(\delta)} + s_{11}^{(1)} \right|^2 \\
&= \left| s_{12}^{(1)} s_{21}^{(1)} \left(1 - \frac{\kappa_{ext,s}^{(1)}}{\frac{\kappa_s}{2} - i(\delta - \Delta_s) \mp \frac{g_m^2}{\Gamma_m/2 - i\delta}} \right) + s_{11}^{(1)} \right|^2 \\
&= \left| s_{12}^{(1)} s_{21}^{(1)} + s_{11}^{(1)} - \frac{s_{12}^{(1)} s_{21}^{(1)} \kappa_{ext,s}^{(1)}}{\frac{\kappa_s}{2} - i(\delta - \Delta_s) \mp \frac{g_m^2}{\Gamma_m/2 - i\delta}} \right|^2
\end{aligned}
\tag{5.11}
$$

$$
\begin{aligned}
T_1(\delta) &= \left| s_{12}^{(1)} s_{21}^{(1)} \frac{a_{out,s}^{(2)}(\delta)}{a_{in,s}^{(1)}(\delta)} \right|^2 \\
&= \left| s_{12}^{(1)} s_{21}^{(1)} \frac{\sqrt{\kappa_{ext,s}^{(1)} \kappa_{ext,s}^{(2)}}}{\frac{\kappa_s}{2} - i(\delta - \Delta_s) \mp \frac{g_m^2}{\Gamma_m/2 - i\delta}} \right|^2 = \frac{\left| s_{12}^{(1)} s_{21}^{(1)} \right|^2 \kappa_{ext,s}^{(1)} \kappa_{ext,s}^{(2)}}{\left| \frac{\kappa_s}{2} - i(\delta - \Delta_s) \mp \frac{g_m^2}{\Gamma_m/2 - i\delta} \right|^2}.
\end{aligned}
\tag{5.12}
$$

In the equations, we define the optomechanical cooperativity C as the expression

$$
C = 4g_m^2/(\kappa_s \Gamma_m).
\tag{5.13}
$$

In the resolved-sideband regime, the cooperative depends on the optical and mechanical linewidths and represents ta normalized metric for the strength of the optomechanical interaction. In fact, cooperativity of 1 is required to change the transmission of $50\,\%$, respectively, for OMIT or OMIA when the system is on resonance.

5.4 OMIA: Brillouin lasing

When considering the Stokes process, the power transfer from the pump to the probing mode leads to the parametric amplification of the latter. The continuous build-up of power can erupt into sustained oscillations when the scattered power overcomes the cavity losses, i.e., Brillouin lasing begins. In a Stokes process, the beating between the laser pump and the acoustic wave tends to reinforce the Stokes field, while the beating between the laser pump and the Stokes wave reinforces the acoustic wave. Under the right conditions, the two processes can generate positive feedback such that the Brillouin gain exceeds the round-trip losses and amplifies the signal exponentially.

This explanation based on a classical interpretation of the phenomenon agrees with the Quantum Mechanics derivation we obtained in the previous section. If we look at the expression of OMIA/OMIT transmitted field in resonance, we can see that the effective linewidth of the mode under analysis Γ_{eff} is given by a combination between the original mechanical linewidth and the optomechanical interaction as

$$
\Gamma_{eff} = \Gamma_{(\text{OMIA,OMIT})} = \Gamma_m \mp \Gamma_{opt} = \Gamma_m \mp \frac{4g_m^2}{\kappa_s}.
\tag{5.14}
$$

When the power increases, this expression is no longer constrained to a positive value for Stokes interaction, remarking a sudden change in behavior as we overcome the lasing

threshold. In fact, a negative peak linewidth is meaningless, but a negative decay rate represents an exponential increase in the mode energy. The lasing threshold is overcome when $C \geq 1$ and can be given in terms of intra-cavity photon number as

$$N_p \geq \frac{\Gamma_m \kappa_s}{4g_0^2} \tag{5.15}$$

or in external power, once taken into account the coupling efficiency

$$P_{th} = \frac{(\kappa_s/2)^2}{\kappa_{ext,s}^{(1)} \left| s_{21}^{(1)} \right|^2} \hbar \omega_s \frac{\Gamma_m \kappa_s}{4g_0^2}. \tag{5.16}$$

We should notice that since the lifetime of the phonons is much shorten than the photons ($\Gamma_m \gg \kappa_s$) because we are unable at room temperature to form an acoustic cavity, we are thus discussing optical Brillouin lasing that results from stimulated optical amplification. In contrast, in "mechanical lasing" or "phonons lasing" the phonons go through an instability process through a self-induced optomechanical oscillator, i.e., build-up of acoustic waves inside the cavity. In fact, in the absence of a mechanical cavity, the exponential increase of the optical field above lasing threshold interacts with the phonons through Anti-stokes scattering, preventing an accumulation of the mechanical mode.

Finally, we should notice that the derived expressions refer to an undepleted-pump regime. However, this condition cannot be met after lasing because the amount of scattered power is no longer negligible with respect to the pump intensity.

5.5 OMIT: strong-coupling regime and mode hybridization

If Brillouin lasing can be hard to characterize because of the exponential nature of the phenomenon, thus involving large amounts of power that make the system unstable, the opposite stands for the strong-coupling regime. Increasing the pump power while analyzing the OMIT response introduces different Quantum Mechanics effects broadly studied in the latest years in the literature because of their usage in quantum information processing.

Strong coupling is a specific condition where the interaction between the optical field and the mechanical vibrations becomes higher than the intrinsic decay rates of both the optical and mechanical modes. In particular, the efficient and coherent energy exchange between the two leads to the formation of collected excited states known as photon-phonon hybrid states. In addition to enhancing the sensitivity of equally optical and mechanical property changes [36], the strong-coupling regime enables the creation and manipulation of non-classical states of light and mechanical oscillators [50, 51]. Implementing quantum transducers to convert quantum information between optical and mechanical degrees of freedom and quantum logic gates to manipulate it leads to great interest in researching optomechanical systems.

The strong-coupling regime is reached by increasing the coupling strength through the build-up of power in the pump mode, and its mathematical formulation follows the equations given in Section 2.4. Starting from the Langevin equation of motions in the case of optomechanically induced transmitted reported in (5.7), we can formulate the free-evolution Hamiltonian (i.e., without stimulation from the input field $\hat{a}_{in}^{(1)}$) in matrix form

$$\begin{pmatrix} \langle \dot{\hat{a}}_s \rangle \\ \langle \dot{\hat{b}} \rangle \end{pmatrix} = -i \begin{pmatrix} -i\kappa_s/2 + \Omega_m - \Delta_s & -g_m \\ -g_m & -i\Gamma_m/2 + \Omega_m \end{pmatrix} \begin{pmatrix} \langle \hat{a}_s \rangle \\ \langle \hat{b} \rangle \end{pmatrix}, \tag{5.17}$$

where we assume the difference between the optical modes close to the Brillouin frequency, i.e., $\Delta_s \approx 0$. We can thus solve for the complex eigenvalues of this non-Hermitian matrix,

obtaining

$$\omega_{s\pm} = \Omega_m - \frac{\Delta_s}{2} - i\frac{\Gamma_m + \kappa_s}{4} \pm \sqrt{g_m^2 + \left(\frac{-\Delta_s + i(\Gamma_m - \kappa_s)/2}{2}\right)^2} \qquad (5.18)$$

When we analyze the eigenfrequencies of the system when stimulating the Brillouin interaction $\text{FSR} = \Omega_m$, i.e., $\Delta_s = 0$, we get

$$\omega_{s\pm} = \Omega_m - i\frac{\Gamma_m + \kappa_s}{4} \pm \sqrt{g_m^2 - \left(\frac{\Gamma_m - \kappa_s}{4}\right)^2}, \qquad (5.19)$$

and we can define two conditions: when $g_m < (\Gamma_m - \kappa_s)/4$, the two solutions have the same real part that corresponds to the frequency of the optomechanical response peak but different linewidths because of the imaginary part's effect on the decay rate; whereas when $g_m > (\Gamma_m - \kappa_s)/4$ the two solutions have different real part $\Omega_m + \zeta$ and $\Omega_m - \zeta$ hinting the presence of two absorption peaks with separation, i.e., the normal-mode splitting regime

$$2\zeta = 2\sqrt{g_m^2 - \left(\frac{\Gamma_m - \kappa_s}{4}\right)^2} \approx 2g_m, \qquad (5.20)$$

with the approximation valid when increasing the power. In particular, the position of the peaks is related to the spectral response of the system, making the mode splitting identifies a hybridization of the eigensolutions, i.e., the response is no longer dominated by the optical system, but by the whole optomechanical interaction thus involving the dynamics of hybrid photon-phonon modes with the eigenmodes as symmetric and antisymmetric superpositions of light and mechanics, associated to the new annihilation operators $(\hat{a}_s \pm \hat{b})/\sqrt{2}$.

With the increase of power, the two peaks keep the same linewidth equal to the average between optical and mechanical linewidth $(\Gamma_m + \kappa_s)/2$ while the separation between the
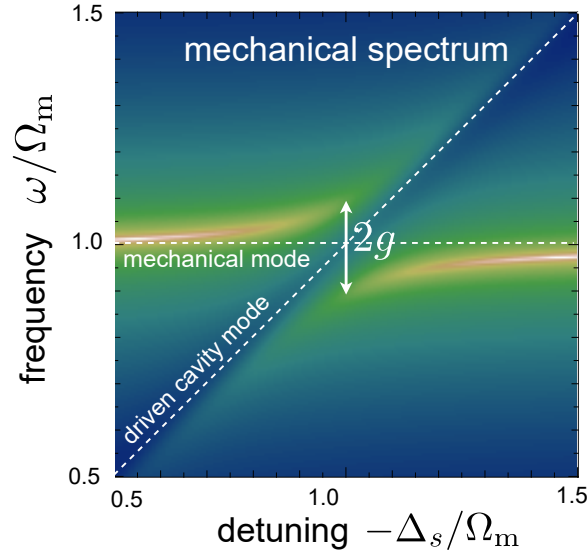

FIGURE 5.5: When the optomechanical interaction is strong enough, the optical response hybridizes and two peaks appear in the spectrum and keep separating as the pump power increases. When we enter the strong-coupling regime $g_m \gtrsim (\Gamma_m + \kappa_s)/2$, the two peaks are resolved, and we observe avoid crossing in the detuning plot. Image from [19].

peaks grows linearly with $g_m \propto \sqrt{P_{in,p}}$. As for Brillouin lasing, the strong-coupling regime is defined as the overcoming of the effective damping rate of the optical-mechanical hybrid modes $g_m \gtrsim (\Gamma_m + \kappa_s)/2$ [33] and corresponds to a total separation between the two peaks (they are completely resolved). The corresponding power threshold for the number of intra-cavity photons is

$$N_p \geq \frac{(\Gamma_m + \kappa_s)^2}{4g_0^2} \tag{5.21}$$

and for the input external power

$$P_{th} = \frac{(\kappa_s/2)^2}{\kappa_{ext,p}^{(1)} \left| s_{21}^{(1)} \right|^2} \hbar\omega_p \frac{(\Gamma_m + \kappa_s)^2}{4g_0^2}. \tag{5.22}$$

Under this regime, the two peaks never overlap even with detuning different from 0, giving the name of "avoid crossing" to the phenomenon (Figure 5.5).

Finally, we should mention that a "stronger" regime exists when the mutual coupling rate overcomes the thermal decoherence of the hybrid modes, and it corresponds to $g_m \geq \{\Gamma_m N_{th}, \kappa_s\}$. Within the Brillouin optomechanics field, it is only achievable at cryogenic temperature when the average number of thermal phonons N_{th} is lower than 1, i.e., the mechanical oscillation is in the ground state. This "quantum-coherent" regime enables quantum-state transfer between the cavity field and the acoustic mode, and thus it is a precondition for many quantum protocols.

This chapter concludes the theoretical analysis required for analyzing and discussing the experimental results and, in particular, provides a mathematical model for the system spectral response that accounts for the optomechanical one and its relation with the external fields that we can experimentally measure. The proposed model still contains several assumptions on the stability and alignment of the system. Nevertheless, it can predict the results to an adequate degree.

Experimental methods 6

6.1 Optomechanical cavity design for temperature tuning and stability

The cavity design focuses on the requirements described in Chapter 3 to match the Brillouin frequency of the quartz crystal with the cavity resonant modes. In this section, we explore the characteristics of the optomechanical cavity, remarking on the design choices to improve the cavity stability to temperature variation, a fundamental requirement for matching the cavity modes with the crystal Brillouin frequency, and performing detuning measurements. In Figure 6.1, we display the cavity model and its support, whereas Figure 6.2 contains some pictures of the assembled cavity in the laboratory. The system comprises several elements

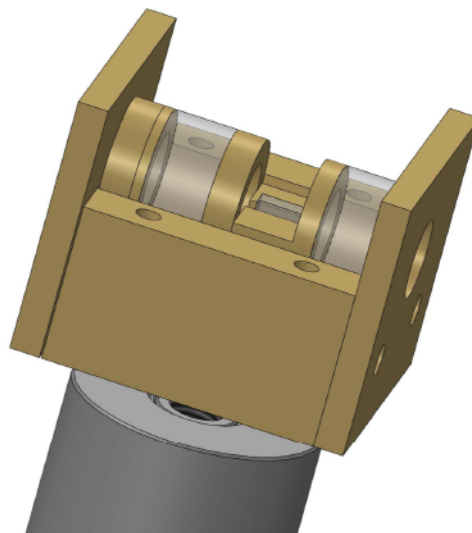
FIGURE 6.1: SolidWorks model of the optomechanical cavity and its support. Brass spacers place the mirrors 10.23-mm apart, while a bottom v-grove aligns them on the x-y plane. The crystal is positioned in the center at 1 mm from the front mirror. The remaining parts of the brass holder help thermalize the structure and constrain the thermal expansion of the cavity pieces along the z-direction.
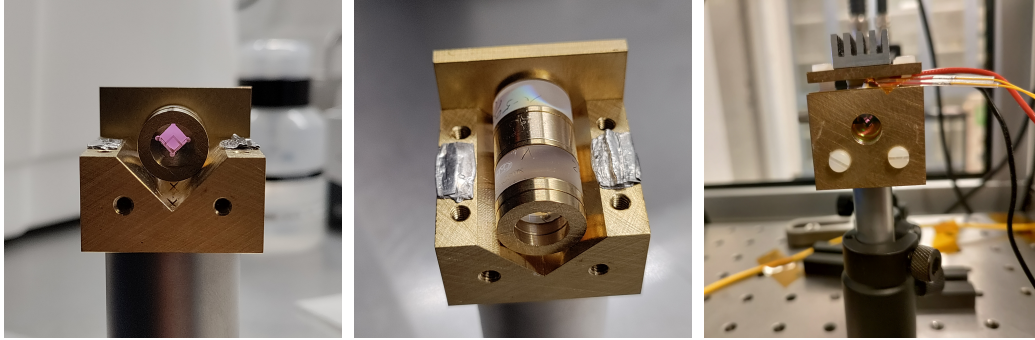
FIGURE 6.2: Photos representing some steps of the cavity assembly. On the left, we notice the v-groove that aligns all the components, with the front mirror and the crystal holder on top. The crystal lies on another groove to remain in the center of the cavity. In the center, the second mirror and the needed spacers are added. We can also notice some Indium scraps on the sides, which improve the thermal conductivity from the top to the bottom of the cavity holder. On the right, we have the entire cavity with the Peltier cell, heat sink, and temperature sensor above.

that can be grouped into optical elements, i.e., the ones that form the optomechanical cavity, and assembly elements that constitute the structure and are responsible for the alignment and temperature control.

Starting from the former, we should mention the 4-mm long z-cut flat-faceted quartz crystal produced by Shalom EO [52]. The crystal is placed in the center of the cavity thanks to v-grooved support at $1\,\mathrm{mm}$ from the first cavity mirror. The optimization of the crystal position and its length has already been analyzed in [31] to increase the spreading of the FSR variations and stimulate only Anti-Stokes scattering (see Section 3.3). The crystal is kept in position using a thermal paste that improves the thermal contact with the support.

The first cavity mirror is produced by LayerTec [53], has a radius of curvature (RoC) of $500\,\mathrm{mm}$ and a transmissivity of $500\,\mathrm{ppm}$. The second mirror has been custom coated by LaserOptik [54] because of the high curvature radius (RoC $= 20\,\mathrm{mm}$) and reflectivity ($T = 40\,\mathrm{ppm}$). Both silica mirrors have a diameter of $0.5\,\mathrm{inch}$. As we can see in Figure 6.2, the x-y alignment of the mirrors is obtained through another v-grooved brass piece, while the distance between the mirrors is guaranteed by filling the space with holed cylinders. The selection of mirror features acts to create an optically stable cavity. The distance between the mirrors of about $10\,\mathrm{mm}$ is required to match the Brillouin frequency of the crystal, and it constrains the mirror curvature. The cavity stability factor $g < 1$ is necessary to have stable cavity mode, i.e., a steady-state solution for the system with light trapped inside the cavity and exiting only through the mirrors and not the lateral surfaces. The stability parameter depends on the mode frequency, the cavity length, and the mirror curvature radii to focus the light inside the cavity and not have diverging modes that can escape the confinement. Caring about these features implies knowing the distribution of the beam waist inside the cavity that the incoming beam needs to improve the coupling coefficient.

Finally, we focus on the brass structure that encloses the optical elements. We have already presented how the v-grooves can help align the optical elements. We should add some remarks about the temperature expansion of the cavity. Firstly, all the elements touching the mirrors should have cylindrical symmetry to reduce the lateral stress when they expand. This feature cannot be easily achieved for the crystal holder, since the crystal itself needs to be placed in the cavity center. Nevertheless, using a holed cylinder allows uniform pressure over the entire circumference of the mirrors. A non-uniform pressure leads to material stress inside the mirrors, deforming the propagating beam and to misalignment due to the microscopic tilt ($\approx \mathrm{mrad}$) of the elements. The second aspect is related to the

thermal stability of the system. A good thermal contact improves the control through an external heat source, while a spatially symmetric heat transfer minimizes the temperature gradient inside the elements, a cause of mechanical deformation and misalignment. In our design, we place a Peltier cell on top of the cavity to maximize contact with the external environment, i.e., improve heat dissipation while cooling the system. The heating/cooling element is in thermal contact first with the top and then with the sides of the cavity to provide heat transfer to the optical elements only through the bottom. Not having the cavity top directly touching the optical elements favors a uniform temperature distribution, increases the holder's thermal mass, and restrains the pressure on the mirrors and spacers, which is detrimental to the cavity alignment. An increase in the thermal mass is crucial when increasing the laser power. The central power-dissipation element is the crystal because of its higher optical losses. We thus have a heat flux from the crystal to the rest of the cavity that needs to be absorbed or counteracted to keep the temperature stable. Failing in this aspect is the principal limit to the maximum power we can employ because the high instability of the cavity resonance frequencies prevents a steady lock and a constant pumping power to study the optomechanical response (see Section 6.3). A final remark should be that the initial uniform pressure requirements must be guaranteed after a temperature change. This is another primary limiting factor for the performances because we require a movement along the central symmetry axis of the cavity, but we must suppress later shift and tilting. A uniform pressure through the front and back panels helps to keep the mirrors in position despite the different expansion coefficients of brass and quartz, while the central v-groove should constrain the crystal movements. Section 7.2 contains a deeper analysis of the temperature-related behavior of the cavity through the optical response measurements.

6.2 Measurement setup description and characterization

After introducing the cavity features in the previous section, we proceed to describe the measurement setup and the acquisition procedure. During the following description, we also report the device calibration and their performances to demonstrate the reliability of the results provided in the next Chapter.

The experimental setup relies on unbalanced heterodyne detection to analyze the spectral response of the laser sidebands that constitute the signal mode in the Section 5.3 model through the beating with the local oscillator, which distinguishes which one we are measuring. In Figure 6.3, we have a schematic representation of the setup, picturing the operation on the light spectrum and the devices we employed. Describing the detected signals through the undergoing modification steps allows us to interpret the collected data and demonstrate the relation with the logical model we presented in the previous Chapter. Moreover, in Figure 6.4, we report the realization of the scheme on the optical table together with the external devices used to control the acquisition process and the setup itself,

Starting from the tunable laser on the top left of the Figure, we have the expected spectral distribution of the emitted light around a tunable frequency ω_p. The Toptica laser [55] can be tuned over a > 50-nm range with an emission linewidth $\delta\lambda < 10\,\mathrm{kHz}$. Together with the locking system, it provides the pump optical mode and the local oscillator for heterodyne detection. The precise laser frequency is tuned with an integrated piezoelectric module that keeps the laser frequency locked with the cavity resonance. Following the pump mode on the top path, we encounter an electro-optic modulator (EOM) [56] that creates the signal mode $\omega_s = \omega_p \pm \Omega$ by stimulating symmetric sidebands from the optical signal. The modulation frequency Ω is controlled by an AnaPico frequency synthesizer [57] and is swept around the Brillouin frequency Ω_m to characterize the spectral response of the cavity signal mode. The modulated signal is thus amplified to control the power of the pump mode, i.e., the strength of the optomechanical interaction. For this step, we employ an NKT photonics
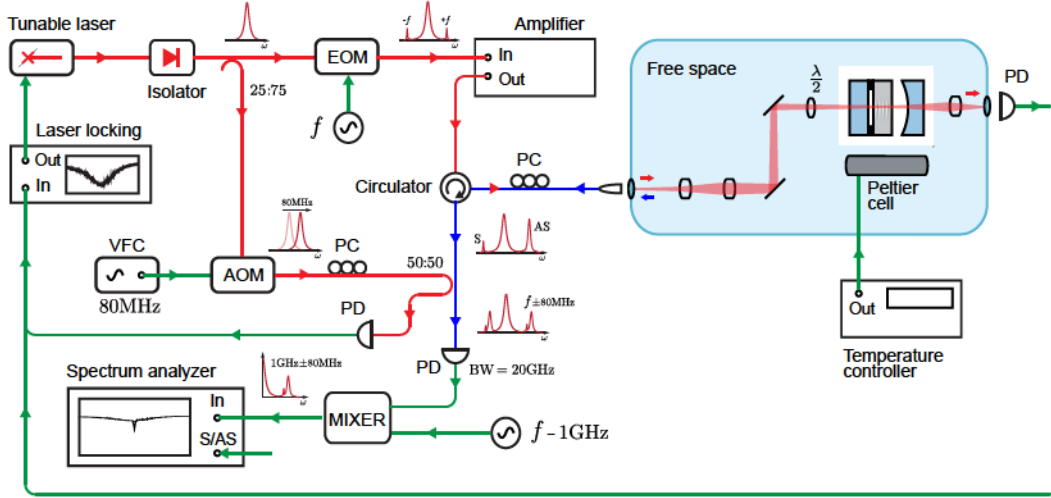
FIGURE 6.3: Scheme of the acquisition setup, including the main processing step of the optical (red and blue) and electrical (green) signals. The input laser is split into a local oscillator which is later offset by 80 MHz and the main beam. From the latter, we create two sidebands of frequency Ω before amplifying the signal and coupling it into free space. In the blue box, we can see the light coupled to the optomechanical cavity and reflected into the fiber. Here, a heterodyne detector mixes the Stokes and Anti-Stokes sidebands with the local oscillator and down-converts the signal to 920 MHz and 1080 MHz. The sideband frequency sweep and the temporal sampling of the spectrum analyzer recreate the spectral response of the cavity at different temperatures. Finally, we collect the pump beam transmitted and reflected signal to lock the laser with the cavity resonance.

amplifier [58], which reaches more than 300 mW of output power with ≈ 7 mW as input. The amplifier bandwidth is wide enough to impact both pump and signal mode and keep the ratio constant, thanks to a flat spectral response in the interested frequency range (see Figure 7.2). After being tuned in frequency and power, the light enters a circulator before a fiber polarization controller and a free-space coupler. These steps are required to extract the reflected signal from the free-space cavity to be sent to the measurement branch without affecting its polarization.

The free-space elements are the core of the setup. Here are two lenses with focal lengths $f_1 = -100$ mm and $f_2 = 150$ mm that control the mode-matching of the light to the cavity modes. After the lenses, two mirrors control the impinging angle and position of the beam to match the optical axis of the cavity. Finally, a half-wave plate (HWP) transforms the linear polarization (required by the mirrors) to excite only one crystal axis. The positions of the mirrors and the lenses are tuned by looking at the reflected and transmitted power of the pure optical cavity first and the complete optomechanical one later. The HWP is calibrated using the same spectrum by suppressing one of the two polarization peaks. Employing a polarization plate on a converging beam is not ideal because of the deformation on the wavefront. Nevertheless, the focal length is high enough to prevent detrimental effects, and we measured no significant differences in the response. A practical remark is that the two polarization peaks have very similar resonant frequencies if the crystal cut is correct, and both can be used to study the Brillouin response with minimal differences. After the optical cavity already discussed in detail, we have another lens that focuses the light on a free-space photodetector. This detector, jointly with the one we will discuss later, provides the transmitted and reflected from the optomechanical cavity to the laser locking apparatus. Finally, we should remark on the presence of the Peltier cell and the high-resolution ($\delta T = 1$ mK) temperature controller [59] that monitors and stabilizes the cavity temperature.

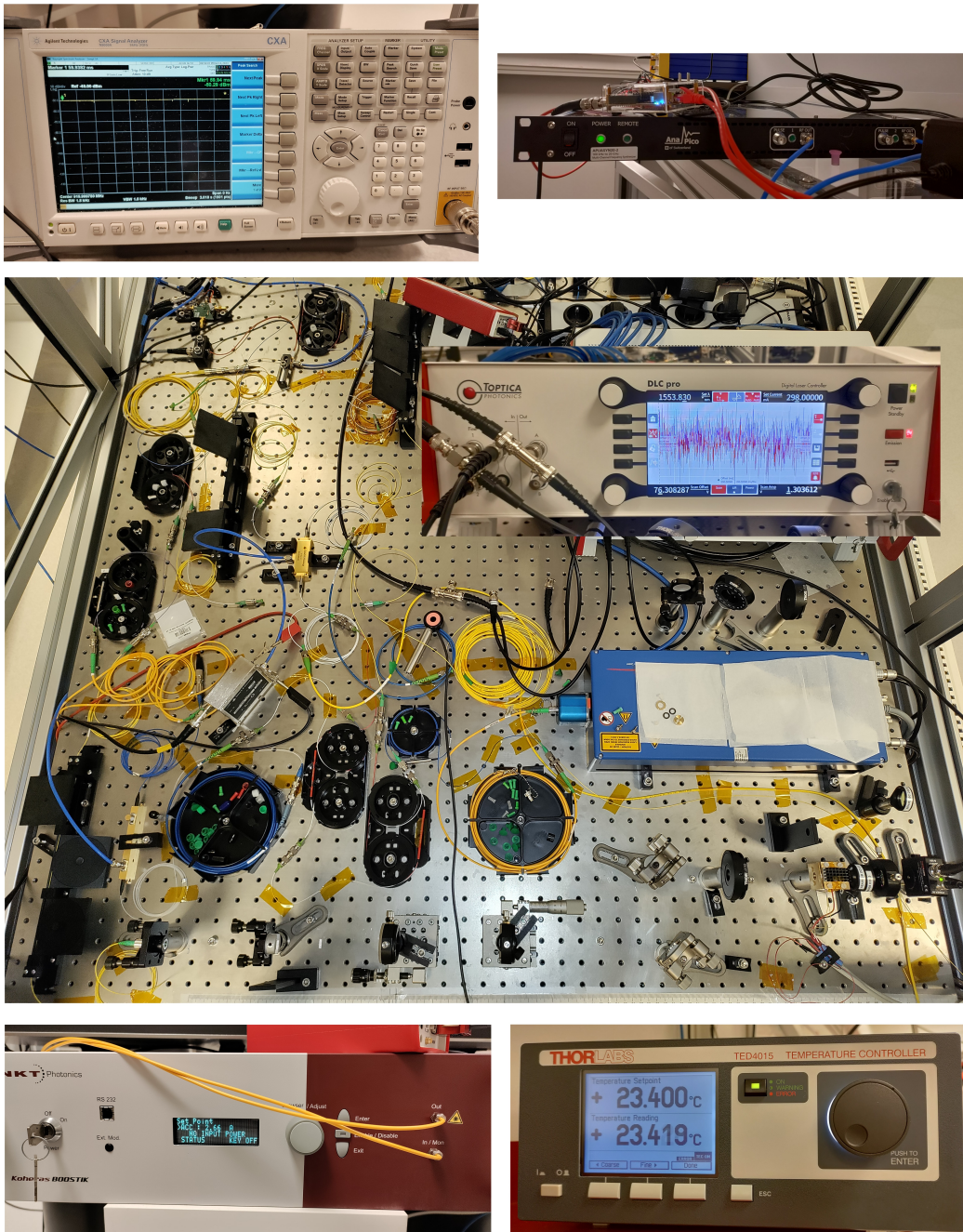FIGURE 6.4: Experimental setup comprises the optical table circuit and the several measurement devices introduced in the acquisition scheme. On top, we have the spectrum analyzer and the frequency synthesizer. On the optical table, we have the laser and the locking system. On the bottom, we have the laser amplifier and the temperature controller. The optomechanical cavity is in the bottom-right corner of the optical table.
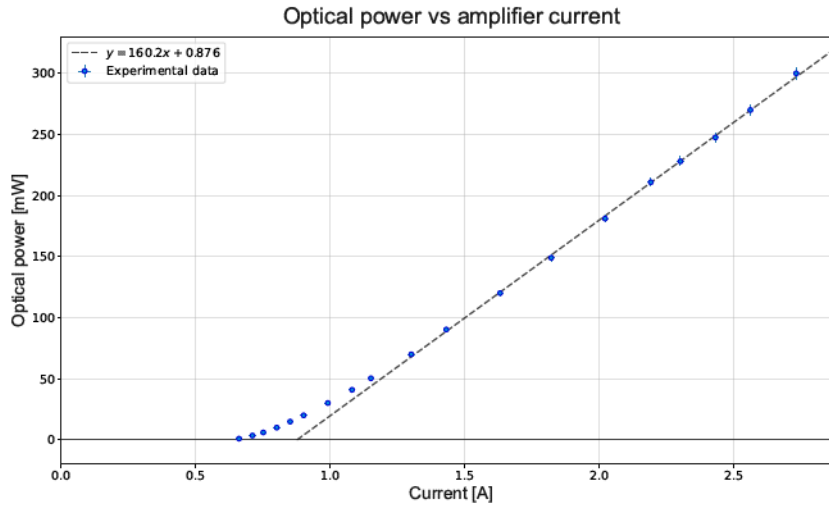
FIGURE 6.5: Amplifier response at 1550 nm. With fixed input laser power ($\approx 7\,\mathrm{mW}$), we control the output signal by increasing the amplifier input current. The gain g becomes positive at 0.76 A and can reach 50 without damaging the other optical components.

Talking about the local oscillator branch, we report the role of the acoustic-optic modulator and the polarization controller. The latter's function is easily explained through the requirement of matching the polarization of the reflected beam from the free-space setup. It is calibrated by maximizing the spectrum analyzer signal corresponding to the beating between the local oscillator and the considered sideband. On the other hand, the former is craftier to describe without first introducing the final part of the setup. The Gooch&Housego modulator [60] shifts the local oscillator frequency ω_{LO} of $\Delta\Omega/2\pi = 80\,\mathrm{MHz}$ to decouple the Stokes and Anti-Stokes spectra after the down-conversion of the detected high-frequency electrical signal. The frequency $\Delta\Omega$ is generated with a fixed voltage-to-frequency converter. The final section of the setup, which is in the bottom left of the pictogram, comprises the detection of the reflected signal power for the locking system and the heterodyne detection scheme. The local oscillator ω_{LO} and the reflected pump ω_p and sidebands $\omega_p \pm \Omega$ are merged with a fiber coupler before being detected through a high-frequency photodiode (BW = 20 GHz) [61]. The electrical signal is then mixed [62] with an electrical local oscillator at $\Omega_1 = \Omega - 2\pi \cdot 1\,\mathrm{GHz}$ from the frequency synthesizer, creating a low-frequency signal that can be detected with a spectrum analyzer [63]. Thanks to the effect of the shifting $\Delta\Omega$, the two sidebands are converted into two signals at 980 MHz and 1020 MHz, and thus, they can be measured separately.

Before discussing the dynamic performance of the setup in the next chapter, we want to report two calibration curves. Figure 6.5 shows the relation between the free-space optical power impinging on the optical cavity and the amplifier current. The other Figure 6.6 displays the relation between the previous free-space power and the measured power of the Anti-Stokes sideband with the spectrum analyzer. The two plots demonstrate that we can reach the interested power without saturating the acquisition chain or introducing power-related artifacts of deformation on the signals. These data will allow a better pump power estimation by looking at the reflected and transmitted light from the cavity, i.e., without relying on a free-space measurement performed before taking the data.
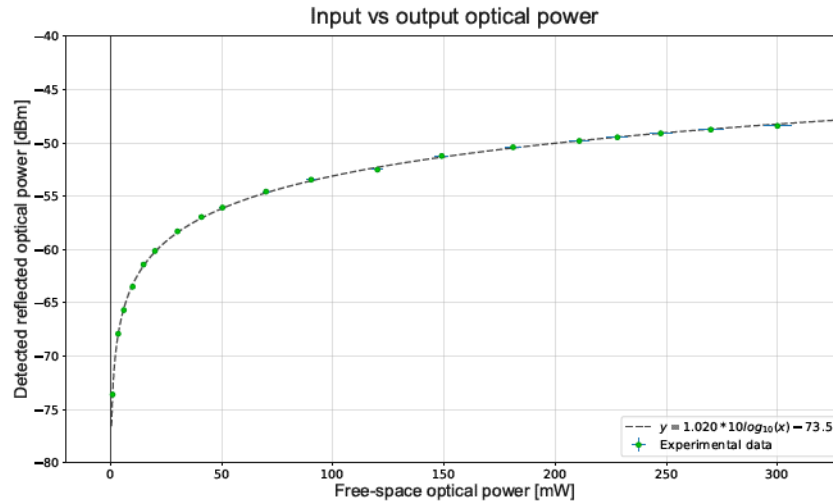
FIGURE 6.6: Trans-characteristic between the input power, measured in free-space before the optomechanical cavity, and the reflected sideband power estimated by the spectrum analyzer after heterodyne detection. The unitary relation between the two quantities in log-scale guarantees a linear behavior for the amplifier, optical components, and acquisition chain up to 300 mW.

6.3 Cavity locking and system stability over time

In the analysis of the cavity design, we presented different factors concurring with the temperature changes in the cavity, which directly or indirectly impact the resonance frequency. The discussion is now extended to the overall system stability during an acquisition at a given power when considering the laser locking module responsible for tracking the cavity resonance and maintaining the light inside the pump cavity mode.

The cavity lock relies on the transmitted or reflected signal from the low-band (BW = 100 kHz) photodetectors. Here, a PID controller monitors the detected power and changes the voltage applied to a piezoelectric component to tune the laser cavity length and resonance frequency accordingly. The limits on the performance of this system lie in the sampling speed of the lock module and the bandwidth of the detectors. In particular, the device cannot lock laser linewidths below 1 MHz because the scanning rate would be too low to provide a meaningful gradient around the central maximum/minimum, preventing a stable and consistent lock of the system. In the same way, when the peak frequency varies too quickly, the device will not track the changes and will "lose the lock".

In the typical operation of the device, this second condition rarely occurs. However, this is the opposite of our setup because of the high powers involved. The state changing from the laser unlocked to the laser locked causes a sudden change inside the cavity because a large amount of power starts dissipating in the crystal. Even assuming perfect alignment and only longitudinal expansion, the energy coming from the crystal will increase the temperature of the entire cavity by about 0.5 K at 300 mW before the temperature controller can start counteracting the change. Moreover, the Peltier cell power is limited and is unable to recover the previous condition of the system within a reasonable amount of time (e.g., 30 min). This behavior is critical and hard to prevent. A valid strategy includes two steps. Firstly, we want to set the controller at a lower temperature so that the FSR after the drift matches the Brillouin frequency range. Of course, we need to guarantee that the alignment before and after the temperature change is the same, and this is far from trivial because even if simulating a higher temperature of the system is not the same as having a heat flux from the crystal irradiating towards the other elements. Moreover, a lock-related sudden change is
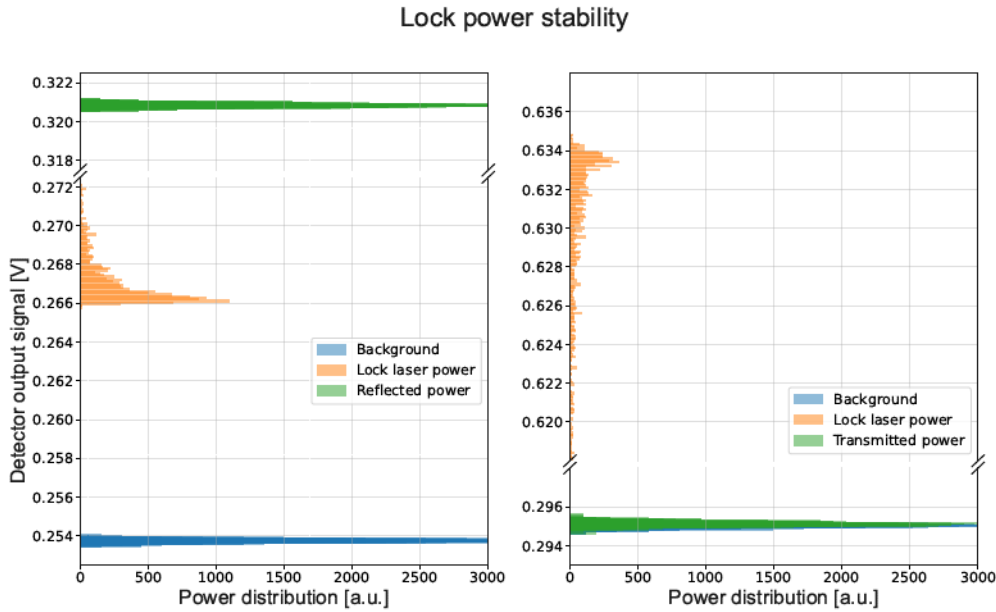
FIGURE 6.7: Example of analysis of lock signals using reflection (left) and transmission (right) signals. In green and blue, we have the voltage distribution of the background with and without laser power impinging the cavity. In red, we report the statistical distribution while locking the system on the reflected signal. The exponential statistics show the quality of the lock, with most of the instantaneous samples of the reflected signal close to the peak apex at 0.266 V. The transmitted signal distribution is typically more unstable because of the light passing through the cavity.

way faster than any temperature ramp we can simulate with the Peltier, so the impact on the alignment is unpredictable.

The other strategy involves a gradual laser power increase with the system locked. It reduces the cavity frequency drifting speed and prevents sudden changes in the cavity state. However, it is still tricky to implement, primarily because the laser locking parameters are diverse at different powers, and an error causes the loss of the lock and requires starting again from lower powers, after waiting for the cavity temperature to stabilize. If the lock is lost while measuring, we must restart the procedure. A slight modification of this step that we found viable is using a "poor lock", i.e., locking the laser far from the resonance peak with improved tracking capabilities and lower impact on the crystal temperature. After reaching the desired power, we can slowly improve the lock, thus increasing the light coupled to the cavity.

An additional remark regards the Stokes measurements. When we want to characterize the system lasing, we also rapidly increase power. However, it is a power transfer from the pump to the signal mode, keeping the overall energy inside the cavity constant. This measurement is critical for another aspect related to the depletion of the pump. If too much power is removed, the peak high will decrease, and if the lock cannot track it, we need to restart the acquisition.

Still related to the lock performance, we must discuss the power stability over time. Three aspects determine the amount of power coupled in the cavity: the amplifier, the locking system, and the interference pattern. The laser and the amplifier contribute to a slow drift in the cavity input power, mainly due to the long time required to stabilize the internal processes, and they can easily be minimized by waiting enough time after each power change. On the other hand, the lock system determines the instantaneous power, so a detailed characterization of its performance is due. When we lock the laser, we will have
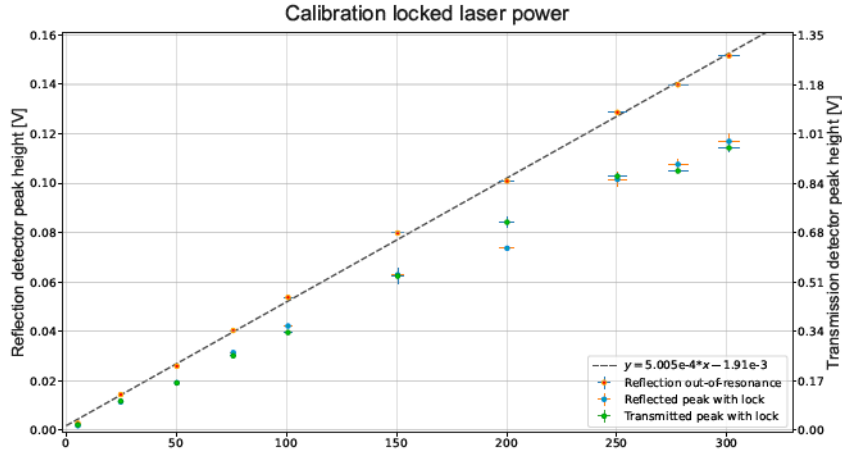
FIGURE 6.8: Analysis of the lock signals to estimate the light power impinging on the optical cavity for the cavity mode at $1553.83\,\mathrm{nm}$. In red, we report the height of the interference pattern, which is a measure of the reflected power when we are out of resonance with the cavity mode. In green and blue, we have the transmitted and reflected signal when the laser is locked. They are used in the analysis to estimate the intracavity photon number because they measure the power that couples into the optomechanical cavity. Increasing the power, the power variance increases because of the lock instabilities.
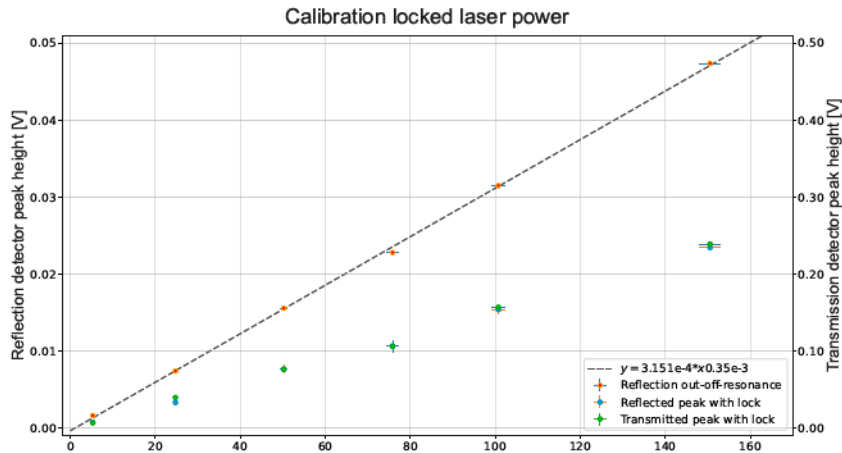
FIGURE 6.9: Same analysis of Figure 6.8 carried out for the mode at $1553.93\,\mathrm{nm}$. The coupled power is lower because the mode relative height is only $\approx 50\,\%$, compared to $\approx 80\,\%$ of the previous example.

a specific power distribution depending on the "lock quality". We define a perfect lock as the condition with a constant power corresponding to the resonant peak apex. We can now evaluate different performances in terms of distance between the average power and the apex one and stability as distribution width around the average value. In Figure 6.7, we report a sample analysis of a good lock quality. In this case, we have a relative height of the peak before of $81.2\,\%$, and after the locking, the average power is $\approx 79.6\,\%$ showing a relative decrease of 1 - $3\,\%$ with fluctuation of $0.5\,\%$ on the short term ($1\,\mathrm{s}$). The OMIA and OMIT measurements we will exhibit in the following chapter shows similar performances for all power range, and if we consider also the long-term stability ($10\,\mathrm{min}$), we have a change of less than $3\,\%$ for high power $P_{in} > 200\,\mathrm{mW}$ and $< 2\,\%$ for lower ones. This

49

information is summarized in Figure 6.8 and Figure 6.9, where we report an analysis of the relation between the measured power from the reflection and transmission detectors and the free-space one collected before starting the acquisition. In these plots, we characterize the modes employed in the OMIA and OMIT measurements (see Section 7.1). Moreover, we also display the corresponding condition when we lock the laser and acquire the data. We can thus improve the estimation of power impinging on the cavity by considering the actual power interacting when the system is locked. The decrease is in part related to the height of the chosen mode (see Section 2.2) and in part to the lock stability. The error bars correspond to the variance of the values over the measurement time.

Finally, we should discuss the interference pattern. The power impinging on the cavity is modulated by an interference pattern caused by multiple reflections between the free-space coupling lens and the first cavity mirror. The impact of the interference is typically a constant factor already integrated into the previous estimation of the impinging power, and it is regarded as part of the background in the measurements. However, when we perform a detuning measurement, we move the peak position over the interference pattern, which drifts because of changes in the first mirror position with temperature. These effects could be taken into account in the data analysis. Still, we will regard them as an additional noise source for the laser power because their impact is negligible compared to the lock-related one.

6.4 Data acquisition and analysis

In the previous sections, we have described and characterized the measurement setup and its performance under temperature variations because they are requirements not only to tune the system to the Brillouin frequency but also for the "detuning measurements" procedure. In this section, we will detail the data acquisition process, the optimization of some measurement parameters, and some related aspects of the data analysis.

As described in Section 5.3, we want to study the optomechanical response of the system at different powers to characterize the strong-coupling regime. From the model, there are two parameters we can tune, in addition to the pump power, i.e., the detuning of the cavity modes FSR from the Brillouin frequency $\Delta_s = \text{FSR} - \Omega_m = \omega_{s,0} - \omega_{p,0} - \Omega_m$ and the offset between the generated sideband Ω and the Brillouin frequency $\delta = \Omega - \Omega_m = \omega_s - \omega_p - \Omega_m$. The cavity temperature controls the former (see Section 3.3) while the frequency synthesizer sets the latter.

A single acquisition of the spectral response corresponds to a temporal sweep of the generated frequency Ω over the considered interval. We can control the number of steps, their duration, and the difference between them through the acquisition software. The frequency of the generated sideband is synchronized with the frequency of the down-conversion mixer to always have the Stokes and Anti-Stokes sidebands at $980\,\text{MHz}$ and $1020\,\text{MHz}$. This step is critical for the spectrum analyzer measurement because instead of scanning the whole sideband for each frequency step, the device generates a fixed beating signal at one of the two frequencies and performs a single power measurement over a small bandwidth. The advantage is a substantial increase in the acquisition speed because each measurement point requires as low as $1\,\text{ms}$. Several parameters of the spectrum analyzer, the frequency synthesizer, and the sideband generator can be optimized to reduce the noise in the data. Some examples include the power of the sidebands, the precise beating frequency of the spectrum analyzer, the measurement time, etc... The parameter optimization relies on multiple acquisitions of the background interference pattern and a comparison of the excess noise, i.e., the difference between the average variance of the data and the variance of the average $\sigma_e^2 = \sum \sigma_i^2 - \bar{\sigma}^2$. The difference is evaluated in two cases, the raw data and the filtered ones. It is worth mentioning that the filter minimum bandwidth is chosen to prevent any deformation of the signal features, so we want to reduce the excess noise within this
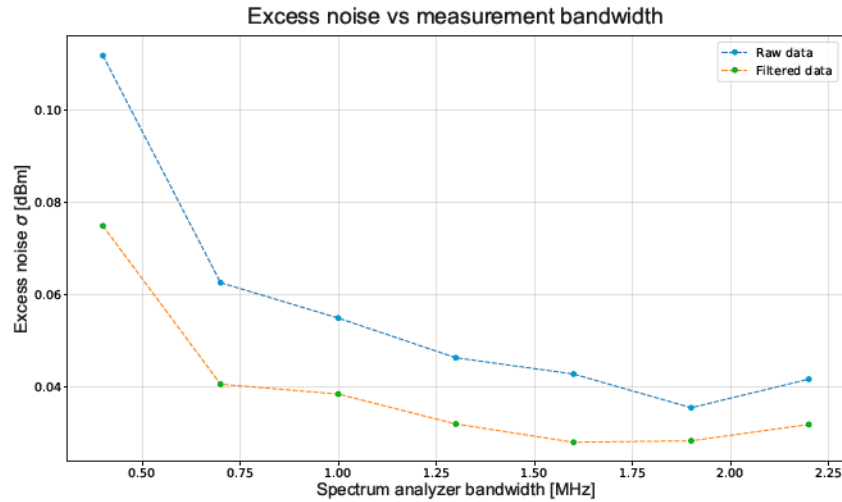
FIGURE 6.10: Optimization of the spectrum analyzer bandwidth at $100\,\text{mW}$. The blue (red) line shows the excess noise in the background acquisitions before (after) the filtering process. Increasing the bandwidth, we obtain more accurate samples even with the lock frequency fluctuations. However, the high-frequency noise also increases, creating a power-dependent minimum around 1.6 - $1.7\,\text{MHz}$.

bandwidth since it is the one we cannot filter out. Moreover, data at different powers must be considered since the system behaves differently. In Figure 6.10, we report the analysis for the measurement bandwidth for $P_{in} = 100\,\text{mW}$. When we increase the bandwidth, we will reduce the excess noise because the sampling region will easily include the sideband peak, even if it fluctuates because of the system's instabilities. However, when the bandwidth is too
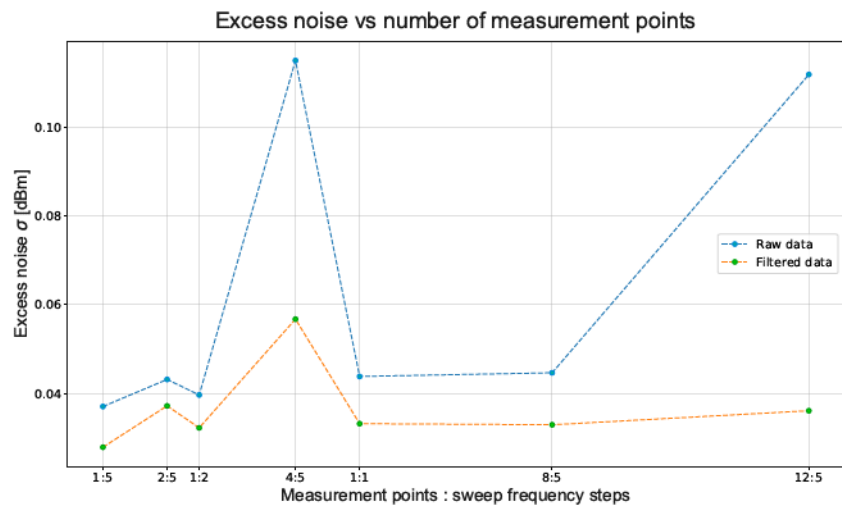
FIGURE 6.11: Optimization of the spectrum analyzer sample number at $100\,\text{mW}$. The blue (red) line shows the excess noise in the background acquisitions before (after) the filtering process. When we sample out of sync with the frequency sweeping, the noise increases because we are not waiting for the setting time of the amplifier and the optomechanical cavity. However, slowing down the frequency synthesizer sweeping rate will increase the measurement time and the system temperature fluctuations.
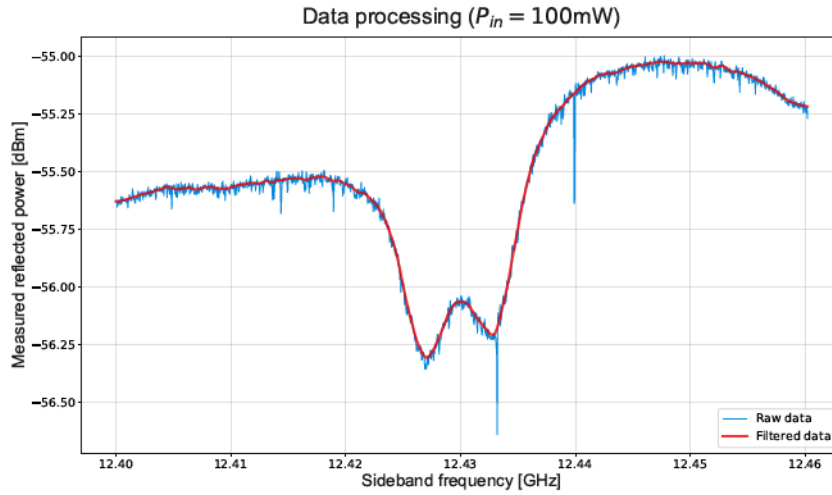
FIGURE 6.12: Example of data filtering for $P_{in} = 100\,\text{mW}$. In blue, we have the raw data from the spectrum analyzer. In red, we have the result of the data post-processing after applying a Gaussian filter with $\sigma = 7.5$ and a median filter with kernel $= 4$.
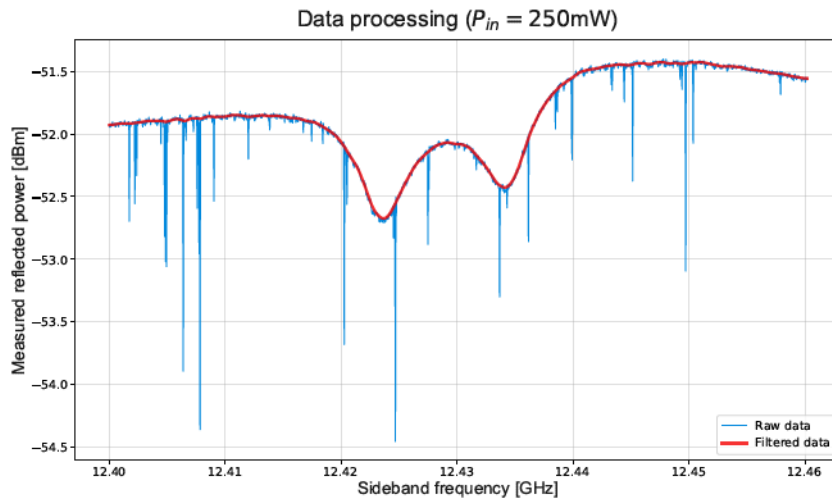
FIGURE 6.13: Example of data filtering for $P_{in} = 250\,\text{mW}$, with the same parameters as in Figure 6.12. At high powers, the number of negative spikes rapidly increases because of the lock instabilities. Nevertheless, the median filter can easily remove all the artifacts.

large, we will collect more background noise, thus increasing the variance. An optimal value has been found for the high-power measurements at $\approx 1.65\,\text{MHz}$. In Figure 6.11, we have another example where we compare the ratio between the spectrum analyzer's sampling points and the frequency steps of the frequency generator. Increasing the spectrum analyzer points will increase the acquisition time and improve the resolution of the response because the minimum sampling time is fixed at $1\,\text{ms}$. On the other hand, we need to guarantee that the cavity is stable over the acquisition time. About the laser sweeping points, we notice we should conserve a synchronization with the previous one to present the spectrum analyzer to sample the response during the settling time of the system. When this condition is not met, the noise will significantly increase, as shown in the plot. The chosen configuration comprises 1500 measurement points over $1.5\,\text{s}$ and 3000 frequency steps of $20\,\text{kHz}$. The number of steps is doubled to the number of sampling points to reduce the variation in the cavity state.

After discussing the single acquisition of the spectral response, we should address the complete characterization of the optomechanical cavity with a given power. The aim is to perform a "detuning measurement", which involves gradually changing the cavity's FSR by heating or cooling the system. The so-called out-of-resonance measurements help with the model parameter estimation since they allow decoupling the variables, e.g., the detuning Δ_s, while increasing the dataset dimension. The limits of this approach have already been mentioned. The temperature changes must be slow enough to have a stable system during each acquisition, and we need to guarantee constant pumping power in the cavity and a steady lock. A typical detuning measurement takes $\approx 10\,\text{min}$, which increases up to $1\,\text{h}$ when considering the setup time for the lock at high powers. Multiple detuning measurements form a dataset, which is analyzed together and fitted with the theoretical model to provide the best estimation for the parameters.

The post-processing of the data and the fitting algorithm are implemented with a Python script. The raw data are processed by removing the background interference pattern and filtering the data. Subtracting the interference collected before the system response using a different temperature is equivalent to normalizing the data with the signal mode impinging power. The resulting reflectivity data is filtered with two methods: a median filter is applied to remove the negative spikes on the trace, and a Gaussian filter reduces the white noise. The result of the filtering process can be shown in Figure 6.12 and Figure 6.13 for $100\,\text{mW}$ and $250\,\text{mW}$, respectively. In the pictures, we observe a significant increase in the number of spikes because they are probably caused by instabilities in the sideband frequency. When the power increases, the lock variations are faster, thus the synchronization between the generated sideband and the local oscillator frequency worsens. The result is the spectrum analyzer sampling outside the sideband peak and measuring only background noise. The number of spikes can be reduced by increasing the measurement bandwidth, with the disadvantages already discussed. Nevertheless, a median filter can easily remove them without impacting the quality of the filtered data.

The cavity reflectivity can be fitted with the model in (5.11) after removing the parameters which cannot be directly estimated

$$R_1(\Omega) = \left| 1 - A \frac{\kappa_s/2}{\frac{\kappa_s}{2} - i(\Omega - \Omega_m - \Delta_s) \mp \frac{g_m^2}{\Gamma_m/2 - i(\Omega - \Omega_m)}} \right|^2. \tag{6.1}$$

In this adapted model, the background subtraction allows us to assume $s_{12}^{(1)} s_{21}^{(1)} + s_{11}^{(1)} = 1$ while the normalization factor $A = s_{12}^{(1)} s_{21}^{(1)} \kappa_s/2/\kappa_{ext,s}^{(1)}$ consider the coupling coefficients which cannot be estimated independently. Regarding the latter coefficients, we could use the optical response of the system (2.10) and the analysis we reported in Figure 6.8 to identify the ratio between the external coupling coefficient and the cavity linewidth. In resonance, we have

$$P_r = P_{in} - \left| s_{12}^{(1)} s_{21}^{(1)} \right|^2 \kappa_{ext}^{(1)} P = P_{in} \left| 1 - s_{12}^{(1)} s_{21}^{(1)} \frac{\kappa_{ext}^{(1)}}{\kappa_s/2} \right|^2 \tag{6.2}$$

and can estimate assuming $s_{12}^{(1)} s_{21}^{(1)} < 1$

$$\frac{\kappa_{ext}^{(1)}}{\kappa_s} < \frac{1}{2} \sqrt{1 - \frac{P_r}{P_{in}}}. \tag{6.3}$$

As an example, for the pump mode in the OMIT response, we obtain $\kappa_{ext}^{(1)}/\kappa_s \approx 0.45$ that is close to the critical coupling condition we aimed for.

A meaningful remark about the fitting algorithm regards the choice of fitting the entire dataset. We have experimented with several strategies because of the model overfitting tendency and the instability of some parameters. As an example, if we want to estimate the

optical response of the system, we cannot use the data near the Brillouin frequency because of the high correlation between optical κ_s and mechanical Γ_m linewidth in determining the width of the peak. The typical solution is independently fitting the optical response further from the Brillouin response and using the estimated parameters to add constraints to the model. This process assumes that the parameters are constant between the two ranges, and it is difficult to guarantee in our cavity. Since each mode has a different linewidth, we need to change the temperature to acquire the optical data, and misalignment of the cavity (see Section 7.3) occurs, in addition to the different interference pattern region and input power, leading to an inaccurate estimate. Increasing the frequency range to improve the estimation is difficult because of the intrinsic drift in the mode shape we have already analyzed in our simulation. Finally, it is challenging to estimate independently A and κ_s because a slight change in the normalization factor leads to significantly different linewidths, affecting the fitting of the mechanical response. The same is true for the normalization factor A, the coupling strength g_m, and the mechanical linewidth Γ_m when we want to estimate the height of the peaks.

The intuitive reasoning behind the choice of fitting the entire dataset together can be summarized into two points: firstly, we want to decouple g_m and Γ_m using data at different power, then we decouple A by adding 10 - 20 % of data further from the Brillouin response; at the same time, now A depends also on the mechanical data so that the pure optical response can estimate κ_s more accurately. Among the disadvantages of this approach is the high computational power required to solve the optimization problem involving $> 600\,\mathrm{k}$ points and > 500 parameters. Moreover, the parameters common to all the measurements have extremely low gradients, i.e., low convergence speed, thus requiring > 1000 iterations of the error minimization algorithm. A valid solution to improve the performance and reduce the computation time of $5 - 10$ times relies on having good initial guesses for the parameters, which can be estimated after independently fitting the measurements at different power with some fixed parameters.

In this Chapter, we discussed several aspects of the setup implementation and measurement procedure, which we will rely on for discussing the experimental results in the next Chapter. In particular, the analysis wants to remark on the limits of the experimental setup and the consistency and calibration measurements we performed to demonstrate the accuracy of our results.

Results presentation and discussion 7

7.1 Optical spectrum and mode characterization

In this Chapter, we present the main results, comprising the optomechanical parameters of the system and a phenomenological description of the cavity behavior, which could help in a design improvement and implementation of the experiment at cryogenic temperature. We start in this Section by introducing some preliminary results about the optical response of the cavity with and without the crystal inside. We then move to the characterization of the temperature behavior (Section 7.2-7.3) and the actual OMIA and OMIT measurements (Section 7.4-7.5).

The alignment of the pure optical cavity relies on minimizing the high-order modes, thus exciting only the fundamental one. The alignment quality depends on the tilt and offset of the incoming beam controlled by the mirrors and the alignment of the mirrors themselves. The goal is to have a horizontal cavity by placing the mirrors vertically inside the groove so that gravity introduces no asymmetries in the pressure while heating and cooling the brass holder. For the mirrors and lenses, we want to maximize the visibility of the cavity modes in reflection and remove all the additional peaks caused by the coupling into high-order
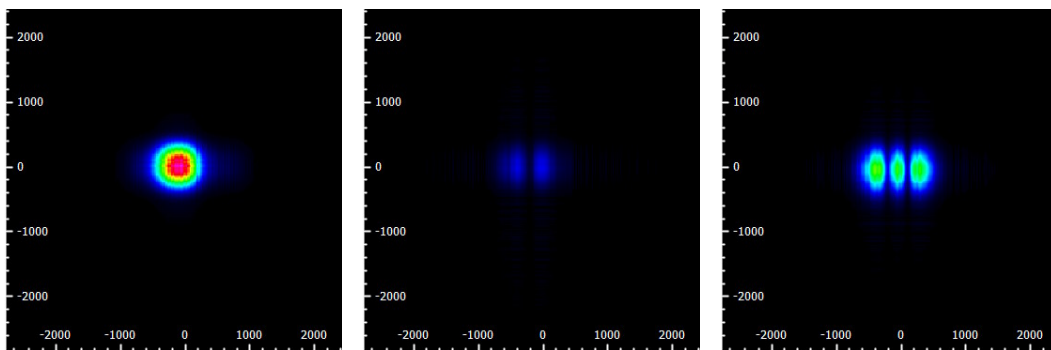
FIGURE 7.1: Beam profiler scans of (from left to right) fundamental, first, and second order Hermite-Gauss modes of the optical cavity without the quartz crystal, collected by measuring the transmitted light. The third plot has a different normalization factor. The fundamental mode is Gaussian, and its coupling efficiency can be optimized through the impinging beam alignment, reducing at the same time the height of the high-order peaks.
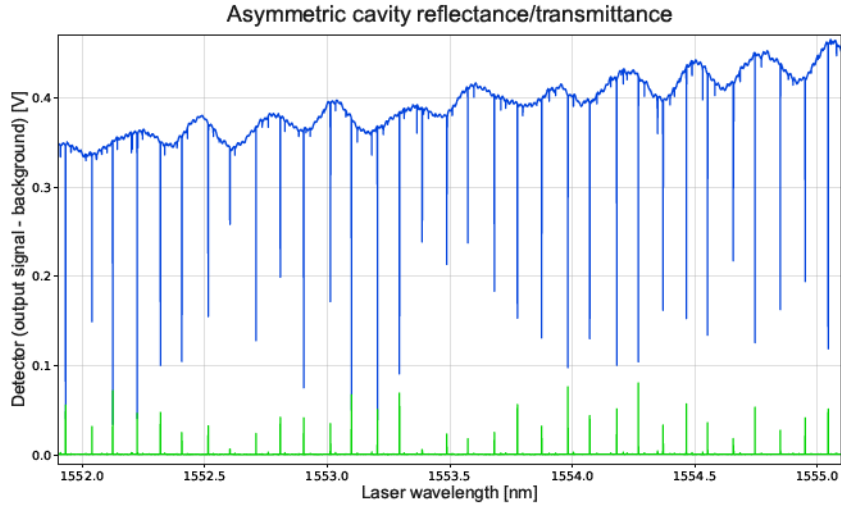
FIGURE 7.2: Laser wavelength scan of $3\,\mathrm{nm}$ around $1553.5\,\mathrm{nm}$ at $23.7\,°\mathrm{C}$ with $P_{in} = 100\,\mathrm{mW}$. In blue (green), there is the reflected (transmitted) signal from the optomechanical cavity. We can notice, the envelope of the amplifier spectral response, the interference pattern from the free-space optics, the high-order modes, and the fundamental mode. The peak height and FSR are modulated by the phase-matching conditions inside the cavity and the misalignment-related "mode shifts".

modes. In Figure 7.1, we display an example of some modes that resonate at different frequencies and so can be excited independently by locking the laser on the reflection peak. The pictures measure the x-y distribution of the transmitted light through the cavity using a beam profiler and represent the spatial distribution of the cavity modes. On the left, we have the Gaussian-shaped fundamental mode; in the center, and on the right, we have the first- and second-order modes (the intensity of the third mode has a different normalization factor compared to the others) with two and three lobes. We should notice the slight asymmetry of the fundamental mode with a broader spread along the x-axis is a cue of a misalignment of the mirrors along the same direction. In fact, even if the laser is perfectly aligned with the cavity axis, a tilt in the back mirror impacts the shape of the fundamental mode, with the reflected light slightly off the axis the more it bounces inside the cavity. On the other hand, this misalignment is extremely small, since we cannot resolve the multiple spots in the transmitted field, and it is related to an asymmetric pressure applied by the cavity panels and the mechanical tolerances of the brass components.

In Figure 7.2, we report a 4-nm frequency scan of the cavity at $I = 1.43\,\mathrm{A}$ ($P_{in} \approx 100\,\mathrm{mW}$) after adding the quartz crystal inside. The cavity reflected (blue) and transmitted (green) power show several features we already anticipated. Firstly, the amplification spectrum of the Raman amplifier causes a large envelope in the reflected light intensity. This modulation does not impact the system dynamics if the different amplification factor is compensated through the input current. Secondly, we have the interference pattern related to the multiple reflections between the first cavity mirror and the free-space optics. We can reduce the visibility of the interference by anti-reflection coating on the fiber tip and the lenses. Finally, we find the fundamental cavity modes separated by the asymmetric FSR and several small high-order misalignment peaks. When the cavity is well-aligned, the intensity modulation of the cavity modes is consistent with the simulations in Section 3.3. We should mention a difference in stability between the reflected and transmitted signals. As we can observe in the plot, when the mode height reduces in reflection, we easily completely lose the transmitted signal because of the increased sensitivity to misalignment due to the dependence on the
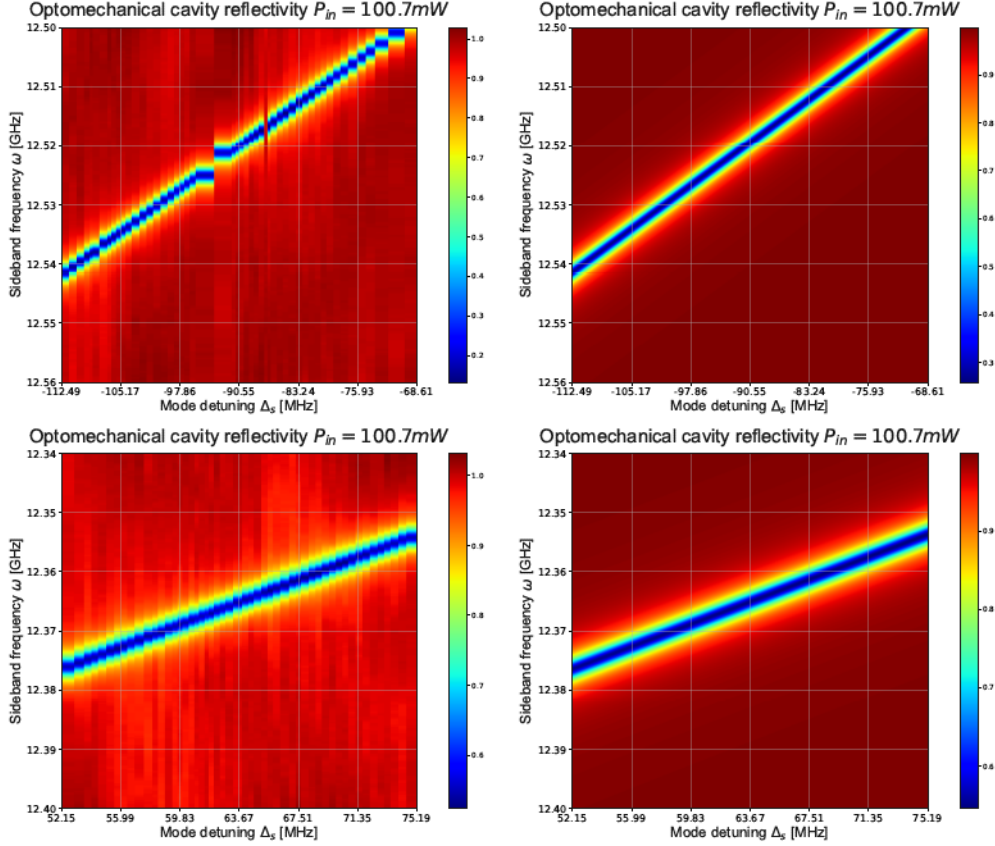
FIGURE 7.3: Experimental data (left) and mode fitting (right) of the spectral response of the cavity modes at 1553.83 nm (top) and 1553.93 nm (bottom) with $P_{in} = 100$ mW. During the measurement, the cavity is locked on the other mode, as for measuring the OMIT and OMIA. The detuning Δ_s follows from a drift in the cavity temperature.

coupling coefficients of both mirrors instead of just the input one. Moreover, out-of-axis light will not be focused on the detector plane, thus reducing the measured light intensity.

In this Section, we also report the reflectivity spectrum of two cavity modes (7.3) around 1553.8 nm and 1553.9 nm. These are the chosen resonances for collecting the OMIA and OMIT responses because of their suitable FSR, but mainly because they are stable with temperature variations. In Section 7.3, we will discuss the detrimental effects of cavity misalignment to explain the difficulty of finding "good" cavity modes to exploit. Even with good alignments of all the components, the drift of the optical linewidth is wider than expected for most of the modes because of the so-called "mode-shifts", i.e., changes in the spatial distribution of the fundamental cavity modes. In the Figure, we also report the dynamics of the two modes 50 - 100 MHz apart from the Brillouin response, with the system at ≈ 0.3 K from the calibration temperature. The estimated linewidth κ_s and normalization factor are reported in Table 7.1.

TABLE 7.1: Fit results considering only the optical response of the system in Figure 7.3.

Mode λ [nm]	OMIA role	OMIT role	$\kappa_s/2\pi$ [MHz]	A
1553.83	signal	pump	2.838 ± 0.002	-0.5790 ± 0.0005
1553.93	pump	signal	3.578 ± 0.002	-0.2641 ± 0.0001

7.2 Temperature-induced drift of the cavity modes

After introducing the optomechanical modes features, we should discuss their dynamics with temperature. In the theoretical simulation of an ideal and perfectly aligned cavity, we have already discussed how the cavity modes drift because of the thermal expansion of the cavity holder. In this short Section, we are presenting the macroscopic changes in the cavity spectrum with an increase in the temperature controller set point.

Starting from the reflected and transmitted signals in Figure 7.2, we can collect data at different temperatures after waiting 10 min for the system to stabilize and plot the FSR and its variation ΔFSR for the different cavity modes (Figure 7.4 and Figure 7.5). Within the Figures, the FSRs varies with different drift speed without an underlying pattern. Compared to the simulations (Figure 3.12) where the variation speed is consistent with a sinusoidal wave, these results show that the elements cannot expand freely because of the increasing pressure applied by the lateral panels. Other causes comprise poor thermal conductivity among the different elements, which prevents a homogenous stress distribution or misalignment of the system, affecting the phase-matching condition on the mirror's and crystal's surfaces. Another problematic aspect is related to the non-constant laser power during the sweeping because of the amplifier spectral response, which could cause an increase in the cavity temperature during the measurement. Despite the limitations, the data show a tuning capability for the cavity FSR with several modes crossing the Brillouin frequency line (dotted line in the plot). In Figure 7.5, we report the ΔFSR vs FSR diagram, which can be compared with the expected results in Figure 3.13. As for the previous plot, we can still observe the effects of temperature as a drift in the points despite several non-ideal behaviors. In fact, when we look at a given mode drift, we can observe a non-monotonic motion with temperature, in contrast with the simulations. Moreover, since this effect is not common to all the modes of the same acquisition, it is probably not correlated to a wrong estimated cavity temperature. A more accurate explanation includes the crystal misalignment and links the phenomenon with the "mode shifts" we introduced earlier. Since the processing algorithm considers the distance
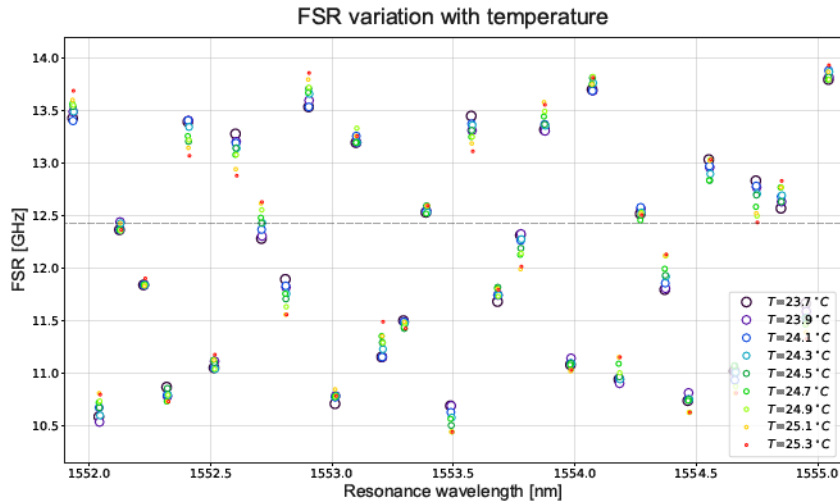
FIGURE 7.4: Example of FSR analysis from experimental data collected with laser wavelength scans around 1553.5 nm at different temperatures between 23.7 °C and 25.3 °C. The dotted line represents the Brillouin frequency Ω_m of the quartz crystal. Compared to the simulated results in Figure 3.12, we have a chaotic behavior of the points, with drifting speed and direction depending on the specific mode. The cause is a non-ideal thermal expansion of the cavity due to the optical elements' misalignment.
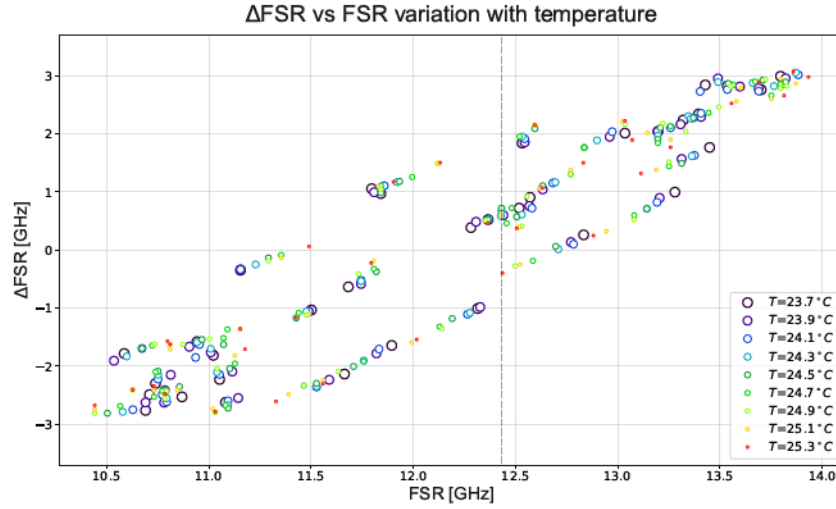
FIGURE 7.5: Example of ΔFSR vs FSR diagram from experimental data collected with laser wavelength scans around $1553.5\,\mathrm{nm}$ at different temperatures between $23.7\,^\circ\mathrm{C}$ and $25.3\,^\circ\mathrm{C}$. The dotted line represents the Brillouin frequency Ω_m of the quartz crystal. When comparing the plot with the simulations in Figure 3.13, the point trajectories can no longer be easily predicted because of the superposition of multiple effects not included in the 1D model.

between the highest peaks in each FSR frequency range, when multiple peaks are present with slightly different frequencies and their heights vary with the temperature, other scans can utilize other peaks, causing jumps in the monotonic behavior of the modes. We can anticipate the content of Figure 7.7 to demonstrate that multiple jumps can happen over a 1-K range, increasing the difficulty in comparing experimental and simulated results. The comparison can be improved by increasing the wavelength resolution above the current $0.5\,\mathrm{pm}$ and reducing the temperature step between each measurement.

7.3 Effects of the crystal misalignment on the cavity modes

In the previous Section, we introduce some distortions in the optical spectrum related to a possible system misalignment. The following content deepens the discussion to pinpoint the most probable cause.

Returning to the beam profiler measurements, we can discuss the quality of the cavity alignment by monitoring the x-y mode shape and its variation with temperature. Taking as an example the images in Figure 7.6, we can clearly distinguish between the left and the other pictures. On the left, the mode area is highly increased because the standing wave inside the cavity does not overlap when reflected by the mirrors. After each reflection, the bean is tilted and no longer propagates parallel to the cavity symmetry axis. We can identify several consequences of this dynamic based on the previous analysis of the cavity and the theoretical background. Firstly, a non-orthogonal propagation inside the crystal implies a shift in the Brillouin frequency because of the different propagation speed (4.2). In addition to not matching the optical axis of the crystal, the mode area increases, thus reducing the single photon coupling rate because of a lower overlapping integral (4.5). Secondly, the cavity temperature stability quickly worsens because the main thermal expansion is no longer along the light propagation direction. It is equivalent to shifting the concave surface of the mirror in the x-y plane, which strongly impacts the reflection angle and, thus, the spatial distribution of the mode and the coupling efficiency of the incoming light inside the
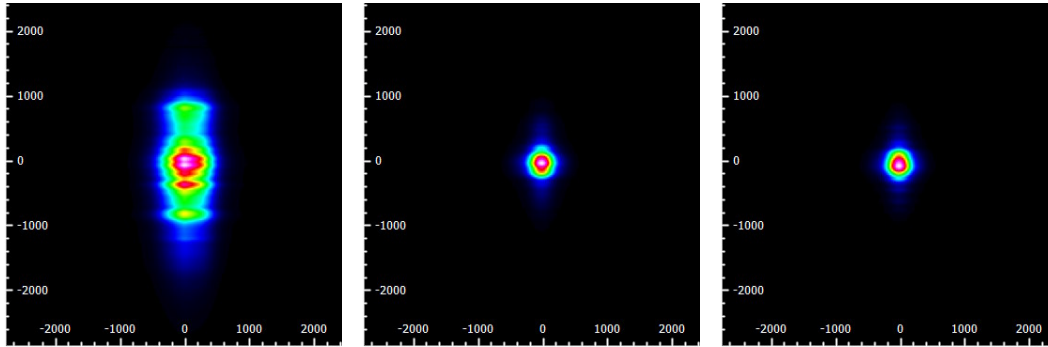
FIGURE 7.6: Beam profiler scans of the cavity modes with the quartz crystal, collected by measuring the transmitted light. On the left, the image shows the case of severe misalignment of the crystal and the mirrors. In the center and on the right, we report the mode transition as a change in the first-reflection spot compared to the zero-order one (below vs. above), induced by a $0.1\,\mathrm{K}$ temperature change.

cavity. Finally, even if we could neglect the stability and reliability problems caused by an out-of-axis fundamental mode, we still have a detrimental effect in acquiring the detuning measurements, i.e., the "mode shift".

When we focus on the remaining two pictures in Figure 7.6, we recognize a particular effect on the mode intensity distribution. The two pictures are collected from a well-aligned cavity and a mode with > 0.8 relative peak height at two temperatures $\approx 0.1\,\mathrm{K}$ apart. Despite the shape of the mode being close to Gaussian, which is a cue of good alignment between the mirrors and the crystal and in-axis beam propagating, we can still observe a change in the higher energy spot from the top in the center image to the bottom in the rightmost one. This change is what we identify as a mode shift or a mode transition. Both the pictures correspond to fundamental modes of the cavity, which can be excited with comparable efficiency from the incoming beam. With a misaligned cavity, the subsequent reflections spread further apart, influence the cavity mode shape, and reduce by several magnitudes the mode matching with the impinging light. Then, when the alignment is good, the spots are close to overlapping, and the spatial distribution is stable with temperature increments. However, the effect of temperature variation changes the phase-matching conditions, making the cavity mode transition from one to the other. The phenomenon is consistent and reproducible, present at different temperatures and affecting all the modes with different degrees.

In Figure 7.7, we can better understand the impact on the spectral response by analyzing the temperature-related drift of a cavity mode. From the simulations, in particular Figure 3.11, we can see how several degrees in temperature difference are needed to impact the peak height, consistent with the nanometric-scale variations of the cavity length over this range. However, the reported plot contains two fast transitions within $1\,\mathrm{K}$ with different characteristics. The one on the right (orange) only temporarily decreases the coupling strength inside the cavity, while on the left (blue), the peak splits, and we transition from coupling to the rightmost to exciting on the leftmost one. This behavior is not polarization-related and can easily comprise the appearance of several peaks separated by several linewidths when the cavity alignment degrades.

The mode shifts have two critical effects on the measurements, the first related to the power stability and the second to the mode frequency and locking. Starting from the power stability, we can clearly recognize that having a decrease in power in either the pump or the signal mode prevents a characterization of the optomechanical response. On one side, a transition in the pump can either change the coupling strength g_m or even lose the lock when the transmission peak disappears (for this reason, we chose to lock in reflect most of the time). On the other, the signal mode experiences power-independent transitions, which can be
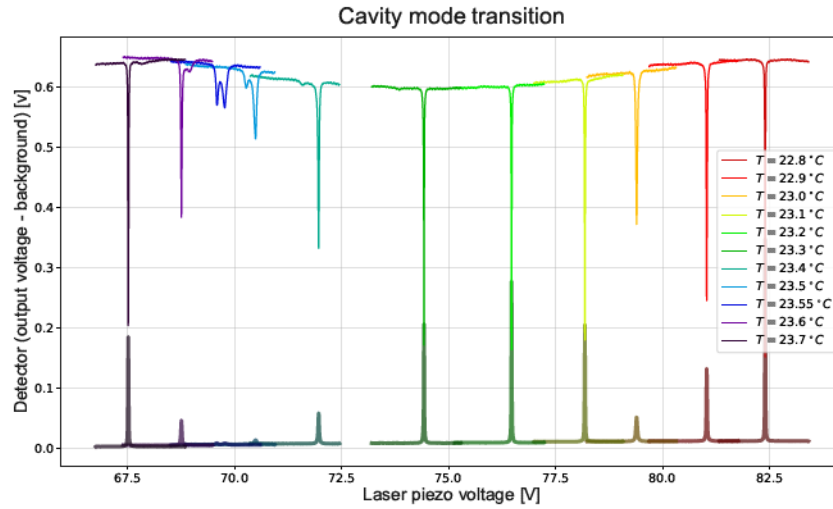
FIGURE 7.7: Example of a mode frequency drift with temperature between 22.8 °C and 23.7 °C. The peak height is modulated with its wavelength, with a larger sensitivity for the transmitted signal, compared to the reflected one. Centered on the orange peak, we observe a mode shift between modes with similar frequencies, which reduces the height by 50 % (80 % in transmission). The purple-blue-green region shows instead the mode transition when the frequencies are different, the transmitted peak disappearing below the noise threshold.

mistaken for mode splitting or impact the clarity of the plots with additional peaks and normalization factors modulated by the mode height. In addition, the temperature where the mode shift happens differs for each mode, often alternating between two consecutive resonances and preventing two stable ones over the required frequency range. Moreover, searching for the cavity modes with higher coupling rates is more challenging due to the rapid changes in the cavity modes, requiring a high-resolution sampling in temperature and frequency to identify the modes separated by the correct FSR and stable over a wide enough range around that interval.

Regarding the second aspect, a sudden change in the dominant mode frequency leads to an automatic loss of the lock when the mode affects the pump mode. It reduces the temperature range in which we can take stable measurements, or even it prevents the acquisition of entire portions of the spectrum. When we change the locking mode, the previous FSR varies by several MHz and could skip the range of the mechanical response. In addition, when working at high powers, we can no longer start from a different temperature to compensate for the mode drift happening when locking the laser (see Section 6.3), or the shift itself is as broad as to include a transition, preventing to even locking the laser in the interested region. Finally, unexpected behaviors can happen when the two frequencies are close. We have documented cases of bistable locking with the two modes at different heights, exchanging the lock from one to the other when the temperature increases because the higher mode sends more power inside the cavity before drifting and losing the locking in favor of the smaller one. Other cases include multiple locking points within the same peak, which help stabilize the lock trapping the power within the two levels or preventing locking a single one causing a broadening of the excited frequency, a decrease of the relative coupled power below 0.5, and a significant increase in the sideband noise (equivalent to the variation caused by high powers). We should remark that the excitation at the same time of multiple peaks is not a problem per se in studying the Brillouin response because both constitute photon sources with the right frequency and momentum; the meaningful aspect is to have a stable coupled power. The opposite consideration is valid for the signal mode because the two modes have

slightly different frequencies, thus broadening the optical linewidth and increasing the power requirements to reach the strong-coupling regime. If the peaks are further apart, the mode splitting is affected, with multiple modes, which earlier were not resolved, appearing and separating at different detuning.

To conclude the analysis, we want to report the main factors responsible for the mode shifts as far as our understanding goes. Because of the speed of the variations, the transitions must be caused by misalignment among the cavity elements. The tilt in the impinging beam and its polarization do not impact the behavior, and they can be optimized for each configuration without making the transition reduce or disappear. It is worth noting that it is the opposite; if the system does not require a continuous optimization of the impinging beam, the cavity modes have the same spatial distribution, and the frequency difference between the peaks is reduced. Looking at the alignment of the two mirrors is not a problem because the analysis of the pure optical cavity does not show the mode shift effect when increasing or decreasing the temperature. It is also straightforward from Figure 7.1, where the fundamental Gaussian mode is spotless, or at least more explicit than any acquisition involving the cavity with the crystal.

After excluding the main other elements, it is easy to guess that the misalignment-causing agent is the crystal itself. A tilt in the crystal compared to the optical axis of the cavity (Figure 7.8) leads to non-zero refractive angles for the impinging beam, which can affect the spatial shape of the cavity modes. The changed phase-matching conditions for constructive and destructive interference are greatly affected and cannot be compensated by the mirrors. If we try to improve the cavity alignment by steering the mirrors, we will destroy the temperature stability. For the reason explained earlier, the modes will spread out from the optical axis and can no longer be compensated. Moreover, the correction is only effective at specific frequencies, thus worsening the coupling efficiency of the overall spectrum. The mechanical tolerances of the brass pieces are most probably the cause of the crystal tilt. In particular, a non-parallel front and back surfaces, a non-orthogonal groove with respect to them, or some defects inside the groove can impair the correct positioning of the crystal with extreme results in the cavity alignment. It is worth noticing that, during the project, several efforts have been carried out to understand and improve the cavity configuration, with the presented results relying on a manual correction of the crystal tilt using the best-machined brass holder.
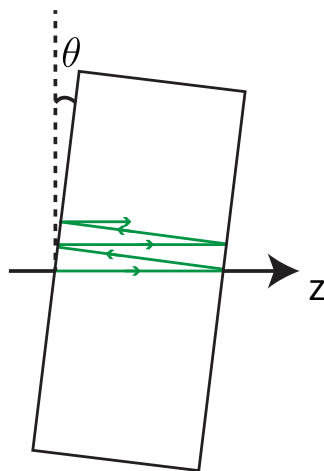

FIGURE 7.8: Pictogram of the multiple reflections arising when the crystal is tilted. The fundamental cavity mode is deformed in the spatial distribution and made more unstable to temperature changes.

7.4 OMIA and Brillouin lasing

In the previous sections, we widely discuss the features of the optomechanical cavity, focusing on describing the optical response of the system and its temperature dependence. In these two Sections, we will present the project's main results, collected after optimizing the cavity alignment and system configuration (see Chapter 6).

TABLE 7.2: Fit results for the OMIA dataset. The table above reports the estimated photon number as explained in Section 6.3, and the power-dependent parameters, i.e., coupling strength g_m. The table below shows the parameters common to all the measurements, i.e., normalization factor A, optical κ_s and mechanical Γ_m linewidth, and Brillouin frequency Ω_m. The single acquisition detuning Δ_s is omitted.

P_{in} [mW]	N_p [10^9]	$g_m/2\pi$ [MHz]
5.27	6.14 ± 0.29	0.60 ± 0.02
24.7	24.01 ± 0.09	1.291 ± 0.008
50.2	53.9 ± 3.6	2.064 ± 0.004
75.8	75.0 ± 2.2	2.465 ± 0.003
100.7	107.8 ± 3.3	2.578 ± 0.003
150.5	163.7 ± 2.0	X

$\kappa_s/2\pi$ [MHz]	$\Gamma_m/2\pi$ [MHz]	$\Omega_m/2\pi$ [GHz]	A
3.029 ± 0.003	10.85 ± 0.02	12.430498 ± 0.000001	-0.4755 ± 0.0006
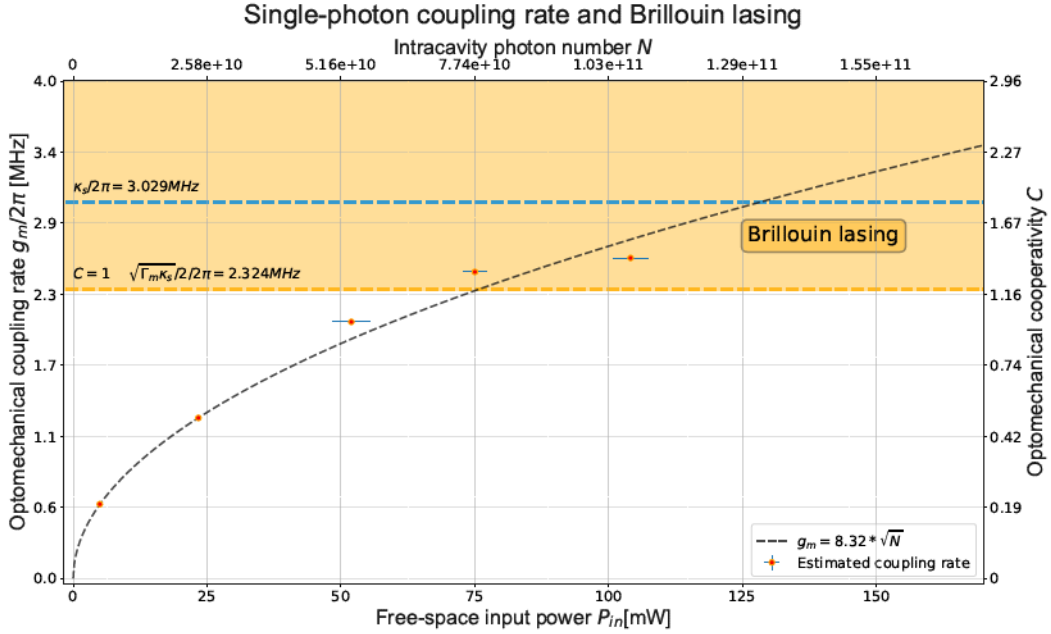
FIGURE 7.9: Power dependence of the optomechanical coupling rate estimated through the OMIA database fitting. The orange region represents the Brillouin lasing above the threshold $C = 1$. Note: the lasing threshold has been estimated using the mechanical linewidth from the OMIT fitting because of the meaningless value obtained from the OMIA fitting.

FIGURE 7.10: In-resonance (FSR = Ω_m) spectral response for OMIA at different powers between $5\,\text{mW}$ and $150\,\text{mW}$.

FIGURE 7.11: OMIA detuning measurements at $24.7\,\text{mW}$ and $50.2\,\text{mW}$. On the left, we have the filtered experimental data with detuning obtained from the fitting. On the right, we display the model prediction. Below the lasing threshold, the peak height increases near the Brillouin frequency, creating two dips that spread apart with increasing power.

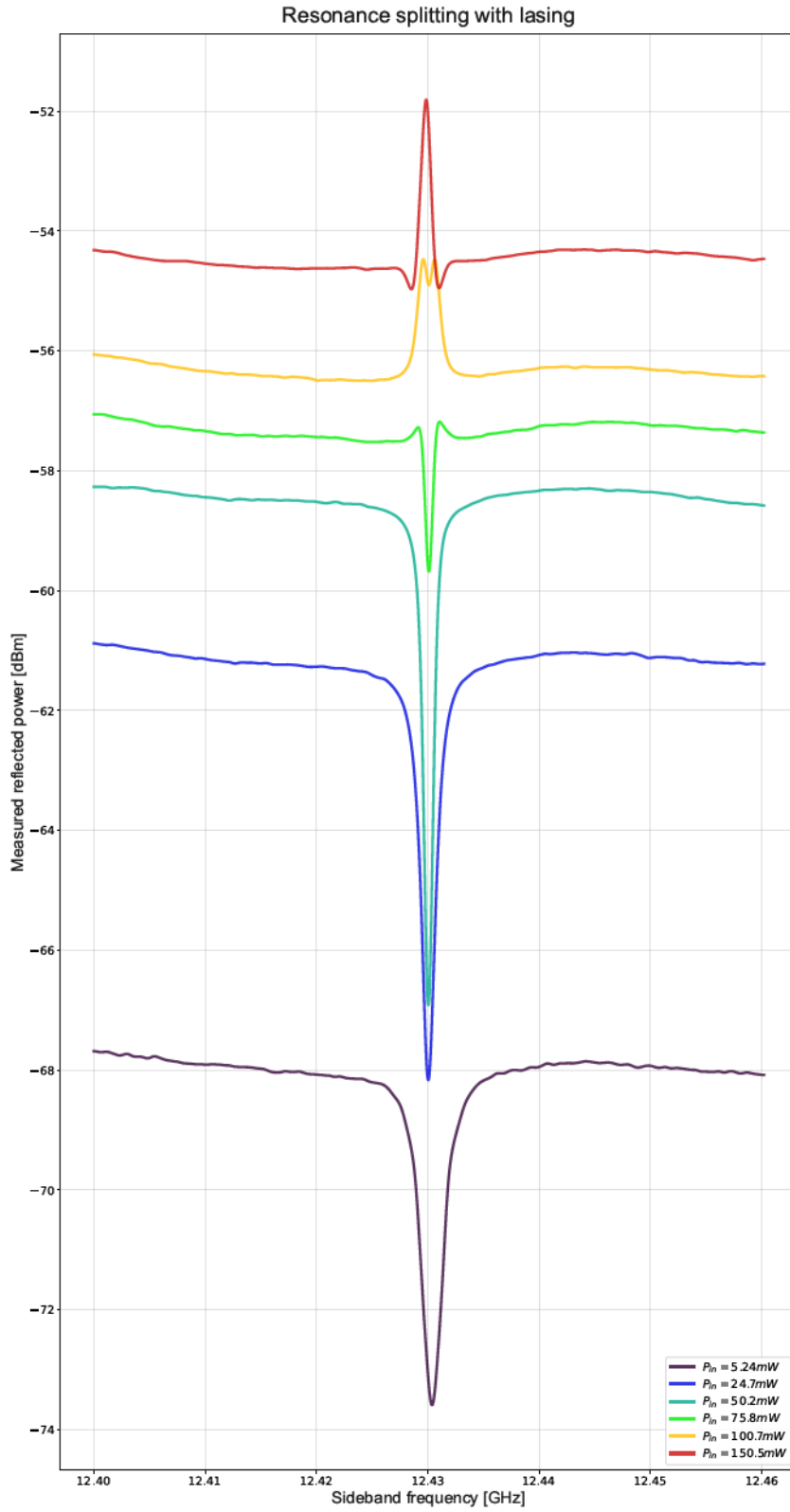The Optomechanical Induced Amplification (OMIA) involves the two cavity modes presented in Table 7.1 and different power between $5\,\text{mW}$ and $150\,\text{mW}$. For our cavity, studying the Stokes scattering is less demanding than the Anti-Stokes response because of the lower power requirements to affect the optical response, i.e., the Brillouin lasing threshold is lower than the strong-coupling one. Applying the acquisition process and the fitting procedure in Section 6.4, we can estimate the optomechanical parameters as reported in Table 7.2. The mechanical linewidth estimation is imprecise because the spectral response is affected by the depletion of the pump mode. In Figure 7.9, we use $\Gamma_m/2\pi = 7.130\,\text{MHz}$ obtained through the OMIT analysis to calculate the lasing threshold $g_m/2\pi = 2.324 \pm 0.002\,\text{MHz}$. The estimate $g_0/2\pi = 8.3 \pm 0.6\,\text{Hz}$ is also impaired, even if still compatible with the OMIT results (see Section 7.5). Moreover, we could not fit the measurement at $150\,\text{mW}$ with the current model because the emission peak is more than three times smaller than the predicted value.

In Figure 7.10, we display the in-resonance response of the optomechanical cavity at different powers. We can observe a decrease in the effective linewidth (5.14) up to $50\,\text{mW}$ before splitting in the dip and the appearance of an emission peak at $75\,\text{mW}$. Increasing the power, we start transferring a significant amount of power from the pump mode to the signal mode, breaking the undepleted assumption for the model. When we try to fit the high-power signals ($C > 1$) with (6.1), we notice a divergent behavior for $(\Omega_{+\infty}, \Delta_{+\infty})$ when the denominator
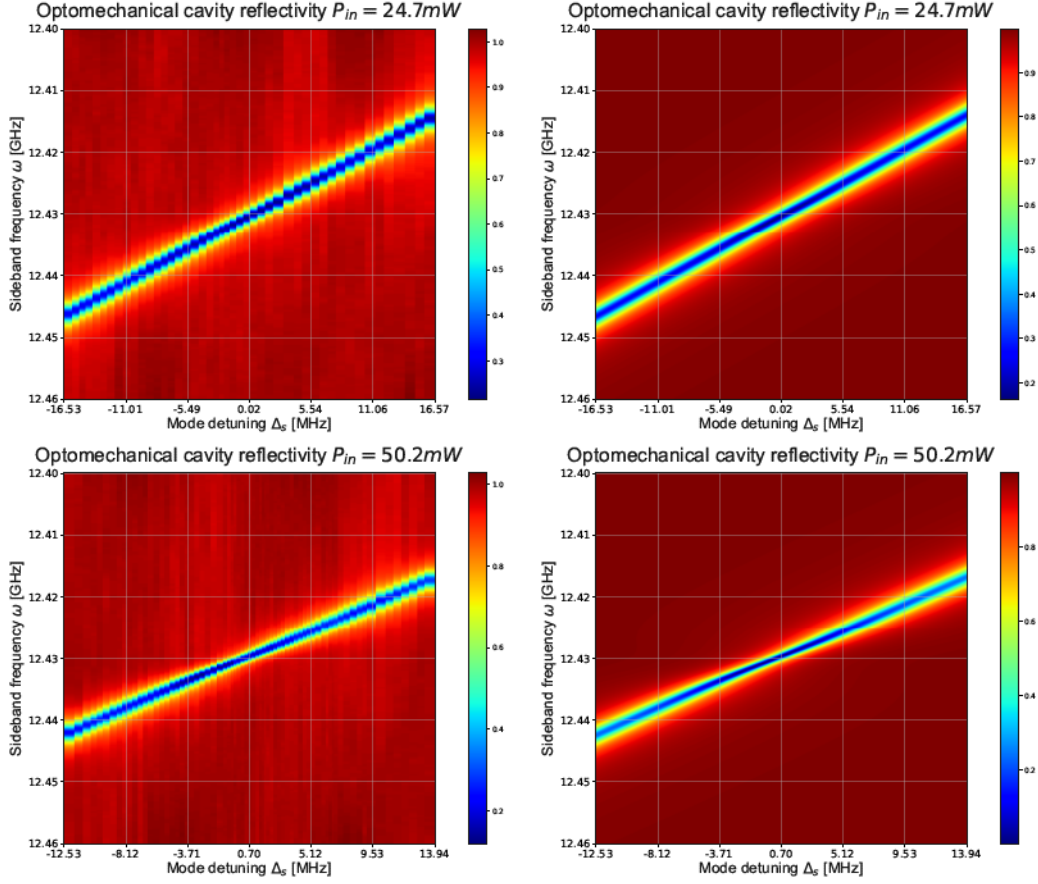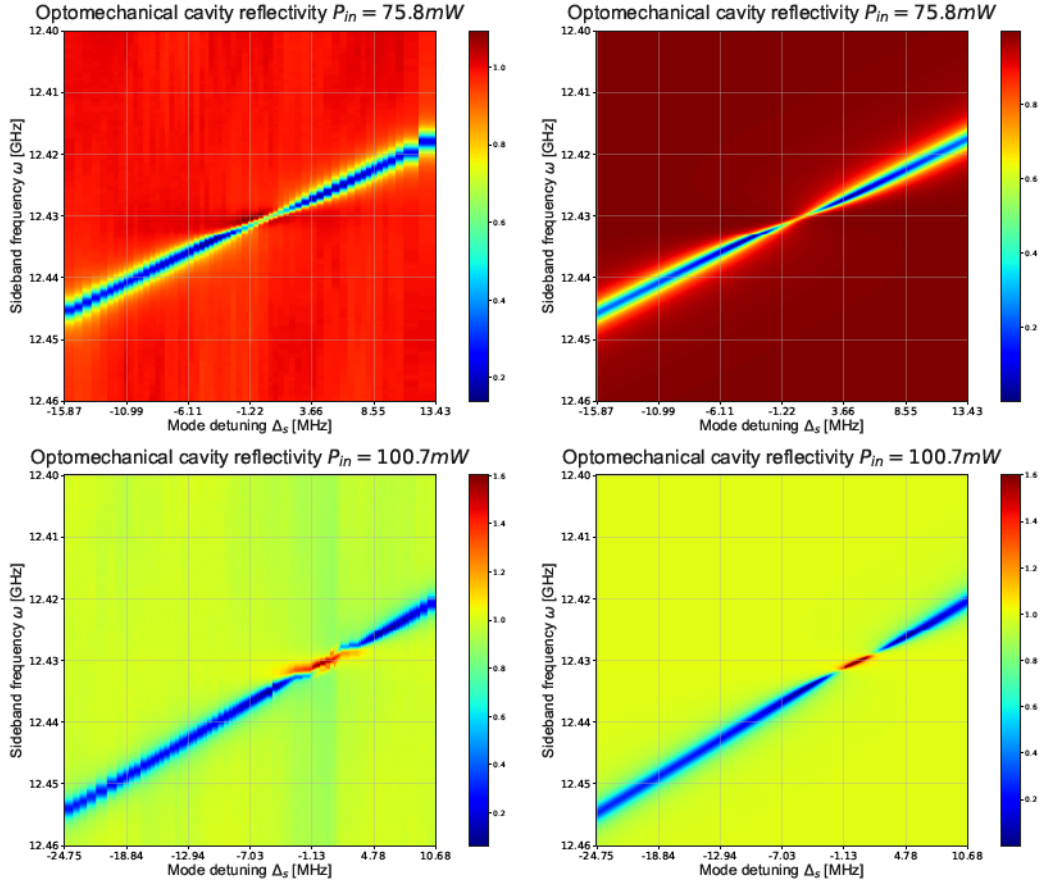
FIGURE 7.12: OMIA detuning measurements at 75.8 mW and 100.7 mW. On the left, we have the filtered experimental data with detuning obtained from the fitting. On the right, we display the model prediction. The spectral response transforms from below (top image) to above (bottom one) the lasing threshold, originating an emission peak while transferring power from the pump mode. The peak then splits with increasing power. Note: the model estimated plot in the bottom right is clipped to exclude the diverging peaks.

of the fraction goes to zero

$$\Omega_{+\infty} = \Omega_m \pm \frac{\Gamma_m}{2}\sqrt{C-1},$$
$$\Delta_{+\infty} = \mp\frac{\Gamma_m + \kappa_2}{2}\sqrt{C-1}.$$

(7.1)

This behavior is a limit of the model and does not appear in the experimental data, preventing an accurate estimation of the parameters when the power increases. Nevertheless, it affects only the OMIA measurements because of the different sign in front of the optomechanical coefficient in the case of OMIT, which prevents the fraction from diverging. The experimental data still show a peak but a finite height because the reduction of the pump mode intensity leads to a decrease in the optomechanical coupling strength that limits the maximum power. The scanning rate and the sampling time could also affect the value because the system transitory analysis must be included. It is worth noting that depleting the pump causes additional problems with the lock system (see Section 6.3), thus increasing the challenge of acquiring this data with enough detuning resolution. In particular, we should notice that Brillouin lasing tends to increase the cavity temperature, thus producing a frequency drift

that is hard to counteract efficiently. The result is the ability to scan the resonance only along one direction and with limited detuning resolution.

In Figure 7.11 and Figure 7.12, we report the detuning measurements corrected at different powers and the corresponding estimation through the model. In Figure 7.11, we are below the lasing threshold and notice an evident reduction of the mode linewidth with the shrinking of the blue trace. Then, in Figure 7.12, we observe a conversion from absorption to emission, with the top figures collected near the lasing threshold and the bottom one above it. The theoretical result in the latter has been clipped to exclude the diverging point and match the experimental data. In analyzing this measurement, we should notice that the emission peak comprises two separated apexes: it is the effect of having a mode shift in the signal mode with two frequencies differing by $\approx 0.5\,\mathrm{MHz} \ll \kappa_s$. The two modes have the same Brillouin frequency, but they resonate with different detuning, thus impacting the quality of the fitting even at lower power with artifacts characteristics of the interference between pulses. We are confident in the two peaks' nature because of the lock behavior when measuring the OMIT response, even if the two peaks are not resolved in the laser scan. We should remark that since the resonance frequency of the two is different, they will introduce a phase modulation in the response, observable through the local minima and maxima near the center and the side of the main peak. The results can be improved by taking into account the additional optical modes and the depletion of the pump mode, but it is not the focus of this project.

7.5 OMIT and strong-coupling regime

The second configuration we characterized is the Anti-Stokes scattering, where we swap the role of the pump and the signal modes. The Optomechanically Induced Transparency (OMIT) is collected for several powers between $25\,\mathrm{mW}$ and $300\,\mathrm{mW}$ to obtain the plot in Figure 7.13. We performed the same analysis and fit as before and summarized the estimated parameters in Table 7.3. We can also define the cooperativity threshold ($C = 1$) (5.13), that is the Brillouin lasing threshold (5.15) and (5.16), for the coupling strength $g_m/2\pi = 2.476 \pm 0.002\,\mathrm{MHz}$, cavity photon number $N_p = 1.055 \pm 0.002 \times 10^{11}$, and the input power $P_{in} = 51.53 \pm 0.08\,\mathrm{mW}$. The strong-coupling regime (5.21) (5.22) is then achieved for $g_m/2\pi = 5.284 \pm 0.006\,\mathrm{MHz}$, $N_p = 4.81 \pm 0.01 \times 10^{11}$, or $P_{in} = 238.7 \pm 0.5\,\mathrm{mW}$. We should report that we could not use the measurement at $25\,\mathrm{mW}$ in the minimization procedure because it seems to have a different normalization factor. It is probably related to some stability problems during the data collection because, at such low powers, the temperature gradient from the crystal toward the cavity holder is yet to be formed, thus the cavity alignment differs. The values reported in the table are obtained by fixing the parameters shared with the other powers and optimizing for A and g_m. For this reason, we will not employ them in the following analysis.

Finally, we can estimate the single-photon coupling rate by fitting the optomechanical coupling rate after calibrating the effecting input power for the system (see Section 6.2) and obtain $g_0/2\pi = 7.76 \pm 0.05\,\mathrm{Hz}$, accounting for the uncertainty of the fit estimate and of the data points. This result accords with the maximum estimated value of $12.98\,\mathrm{Hz}$ in the more favorable case of acoustic cavity formation. The difference between the two is also consistent with previous results [30, 32] measured at cryogenic temperatures. In Figure 7.14, we display the fitting results, with particular attention to the optical and mechanical linewidth estimate, other than the strong-coupling regime and the cooperativity threshold. We should remark the reported intracavity photon number N includes the locking effect and the pump mode estimate presented in Section 7.1. The effect is a scaling factor that improves the estimate of the single-phonon coupling rate g_0.
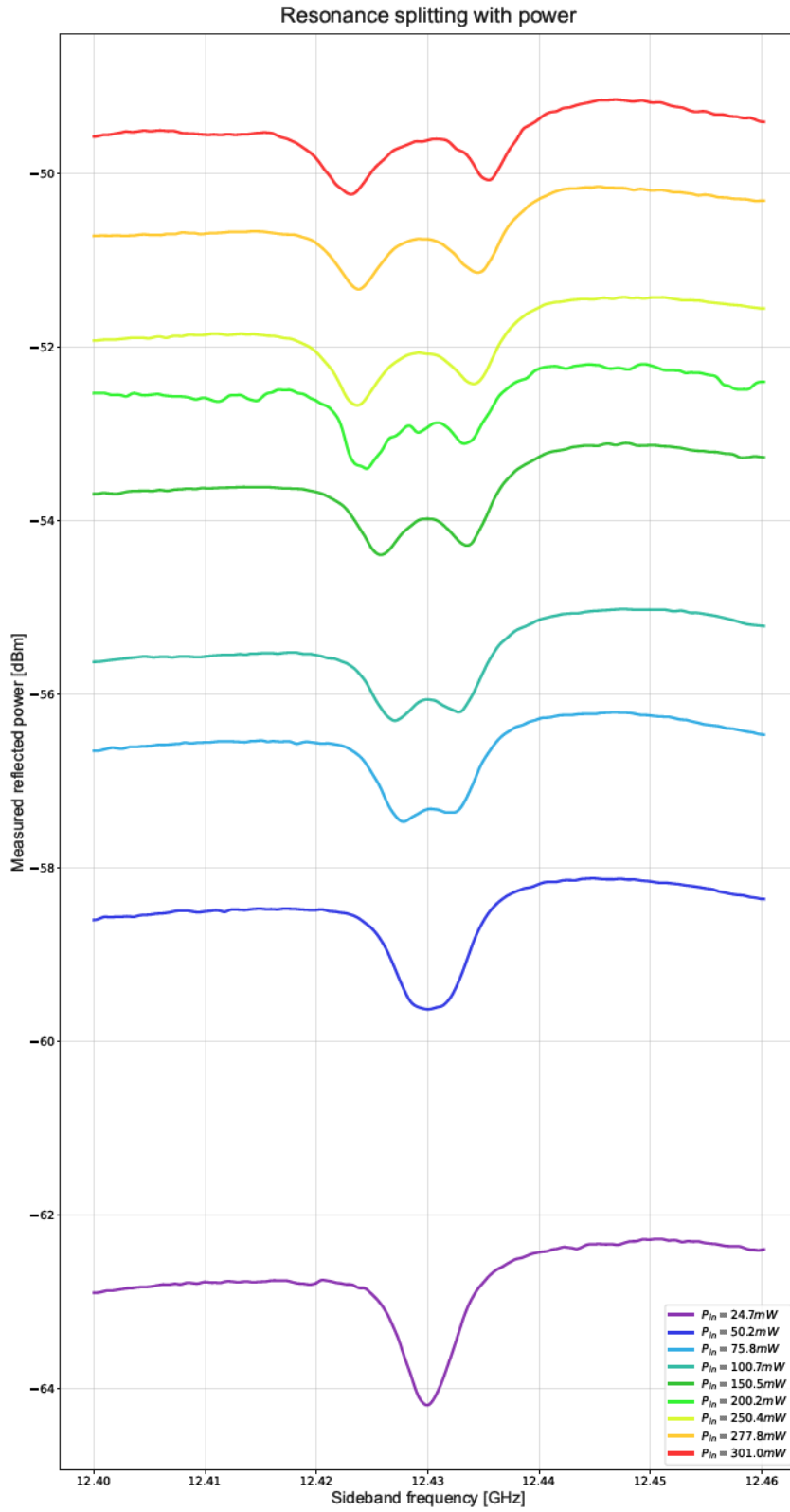
FIGURE 7.13: In-resonance (FSR $= \Omega_m$) spectral response for OMIT at different powers between $25\,\mathrm{mW}$ and $300\,\mathrm{mW}$.

TABLE 7.3: Fit results for the OMIT dataset. The table above reports the estimated photon number as explained in Section 6.3, and the power-dependent parameters, i.e., coupling strength g_m, and normalization factor A. The table below shows the parameters common to all the measurements, i.e., optical κ_s and mechanical Γ_m linewidth, and Brillouin frequency Ω_m. The single acquisition detuning Δ_s is omitted. Compared to the OMIA results, in this analysis, we used a different normalization factor for the first dataset at 24.7 mW, fitted independently after estimating the shared parameters.

P_{in} [mW]	N_p [10^9]	$g_m/2\pi$ [MHz]	A
22.7	55.03 ± 0.39	1.978 ± 0.007	-0.1914 ± 0.0001
50.2	98.4 ± 2.6	2.450 ± 0.004	
75.8	165.0 ± 2.6	3.122 ± 0.003	
100.7	224.2 ± 3.7	3.597 ± 0.003	
150.5	338.1 ± 7.1	4.180 ± 0.004	-0.2663 ± 0.0002
200.2	398.1 ± 6.9	4.937 ± 0.004	
250.3	550.8 ± 15.1	5.686 ± 0.004	
277.8	584.5 ± 9.6	5.743 ± 0.005	
301.0	635.7 ± 17.7	6.148 ± 0.007	

$\kappa_s/2\pi$ [MHz]	$\Gamma_m/2\pi$ [MHz]	$\Omega_m/2\pi$ [GHz]
3.438 ± 0.003	7.123 ± 0.008	12.429643 ± 0.000002
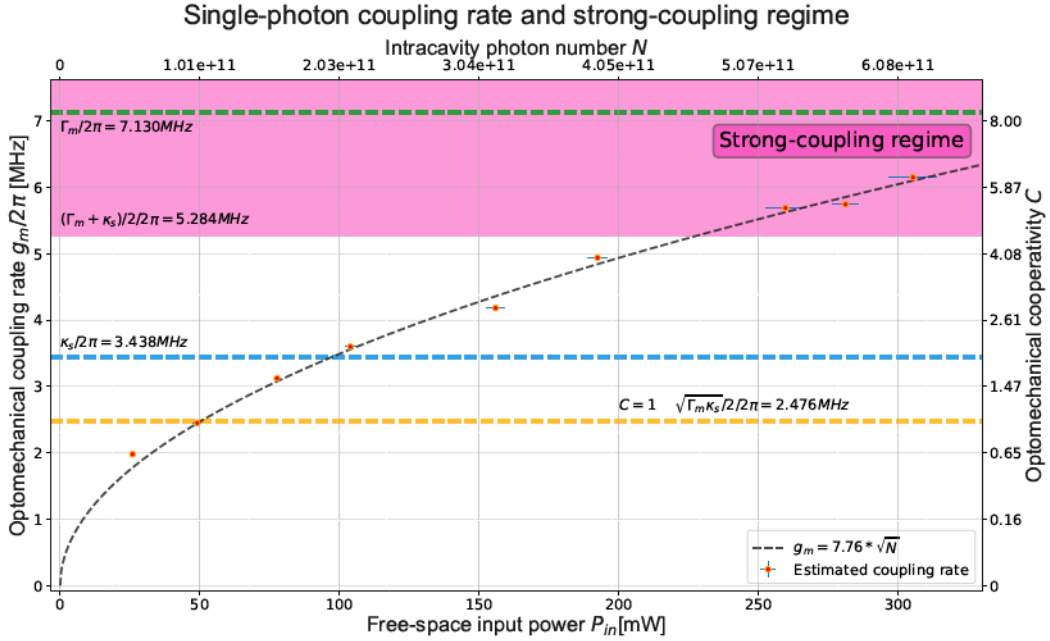
FIGURE 7.14: Power dependence of the optomechanical coupling rate estimated through the OMIA database fitting. The pink region corresponds with the strong-coupling regime. We also reported the optical and mechanical linewidth, and the $C = 1$ threshold, estimated from the fit results. Considering the coupling strength at different powers, we can estimate the single-photon coupling rate g_0. Note: the estimation of g_0 does not use the first data point because it has not been fit together with the others.

FIGURE 7.15: OMIT detuning measurements at $50.2\,\mathrm{mW}$ and $100.7\,\mathrm{mW}$. On the left, we have the filtered experimental data with detuning obtained from the fitting. On the right, we display the model prediction. When the power increases, a splitting in the resonance peak appears in correspondence with the Brillouin frequency.
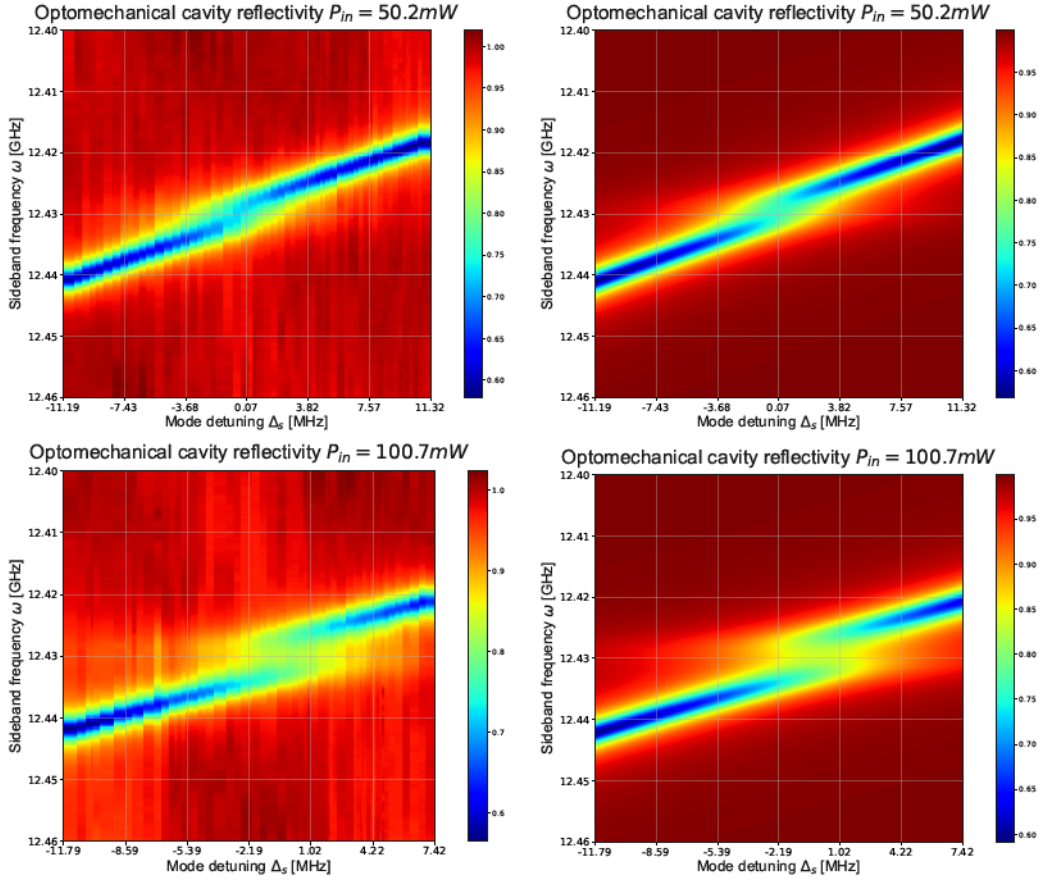
To conclude this description, we report the detuning measurement and their corresponding fittings, which allowed the estimation of the parameters in Figure 7.15, Figure 7.16, and Figure 7.17. In the first set of images, we can observe the mode splitting appear, with the top figure showing the two minima at $P_{in} = 50\,\mathrm{mW}$ and, at the bottom, the peak separation taking shape at $100\,\mathrm{mW}$. The first image corresponds to the condition $C = 1$, while the second has a coupling strength comparable to the mechanical linewidth Γ_m. Increasing the power at $150\,\mathrm{mW}$ and $200\,\mathrm{mW}$ (Figure 7.16), the modes spread further apart but remain within the weak-coupling regime. Finally, the peaks are resolved in the last set of figures, where the splitting is wider than double the hybrid-mode linewidth. We have avoided crossing in the detuning plots. For these measurements, locking noise and temperature instability limit the maximum achievable power. When we try to send more than $250\,\mathrm{mW}$ of power, the Peltier cell is no longer able to keep the temperature stable; the noise in the data is increased because of the out-of-peak sampling (see Section 6.3), and the lock is difficult to reach and maintain. As an example, at $300\,\mathrm{mW}$, only 10 - 15 % of the spectra are consistent and can be used.
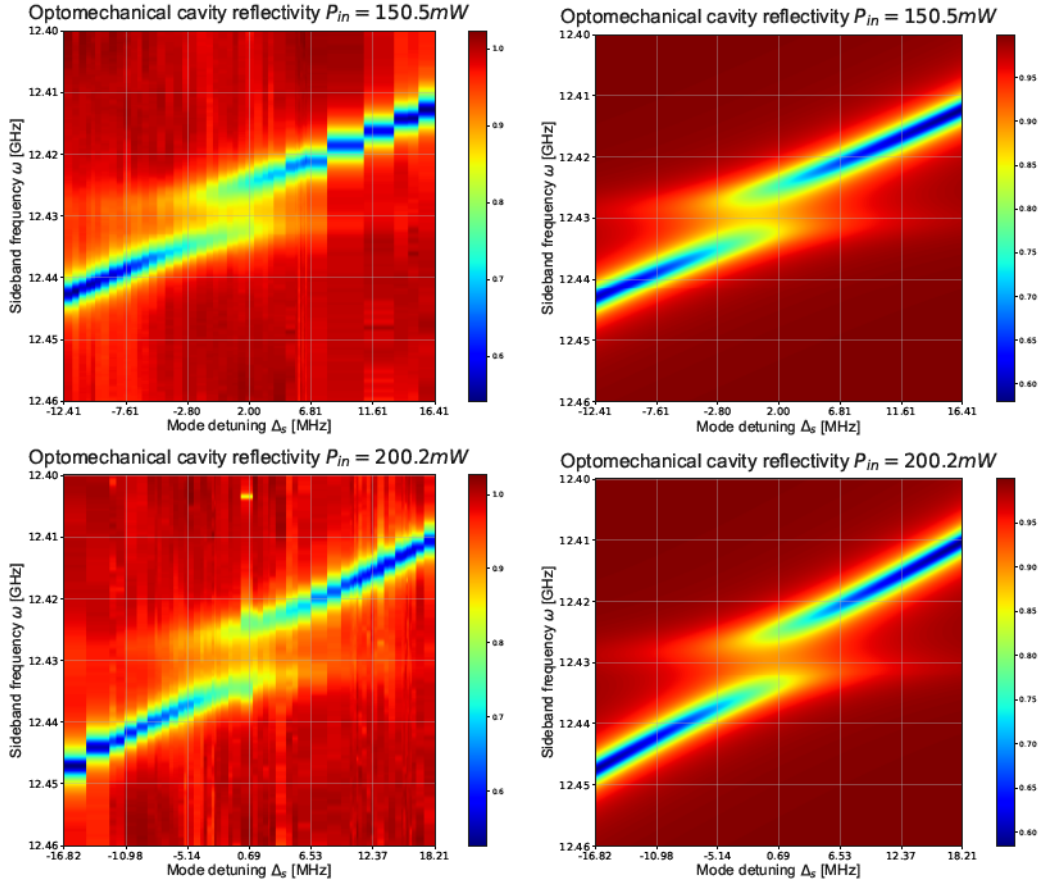
FIGURE 7.16: OMIT detuning measurements at $150.5\,\mathrm{mW}$ and $200.2\,\mathrm{mW}$. On the left, we have the filtered experimental data with detuning obtained from the fitting. On the right, we display the model prediction. The split distance at the Brillouin frequency increases with g_m and the pump power, spreading apart the two dips.

7.6 Limits of the setup and possible improvements

In presenting the experimental setup, the acquisition and analysis methods, and the final results, we have already introduced several limitations to the performances, which were analyzed and overcome during the project development. This Section will conclude the discussion, summarizing the main aspects and proposing strategies to solve the remaining issues. We can divide the analysis into two topics, the optomechanical cavity, and the measurement setup.

Starting the discussion with our cavity design limits, we recall the limiting aspects for the detuning measurements. On one side, we have non-uniform temperature distribution caused by the high power dissipated in the central crystal. On the other, we have the mechanical tolerances of the cavity holder, preventing an optimum alignment. The temperature stability is impaired by the insufficient power of the Peltier cell, the physical distance between the cooling source and the optical elements, and the position of the temperature sensor too far from the cavity core. The consequent temperature fluctuations are the primary source of cavity response instability and prevent adequate control with high laser powers. Still, the current setup can characterize the strong-coupling regime we aimed at. The remaining issue is the temperature drifting velocity, which prevents collecting enough data in a single temperature sweep because the fast temperature increase in the cavity core cannot be
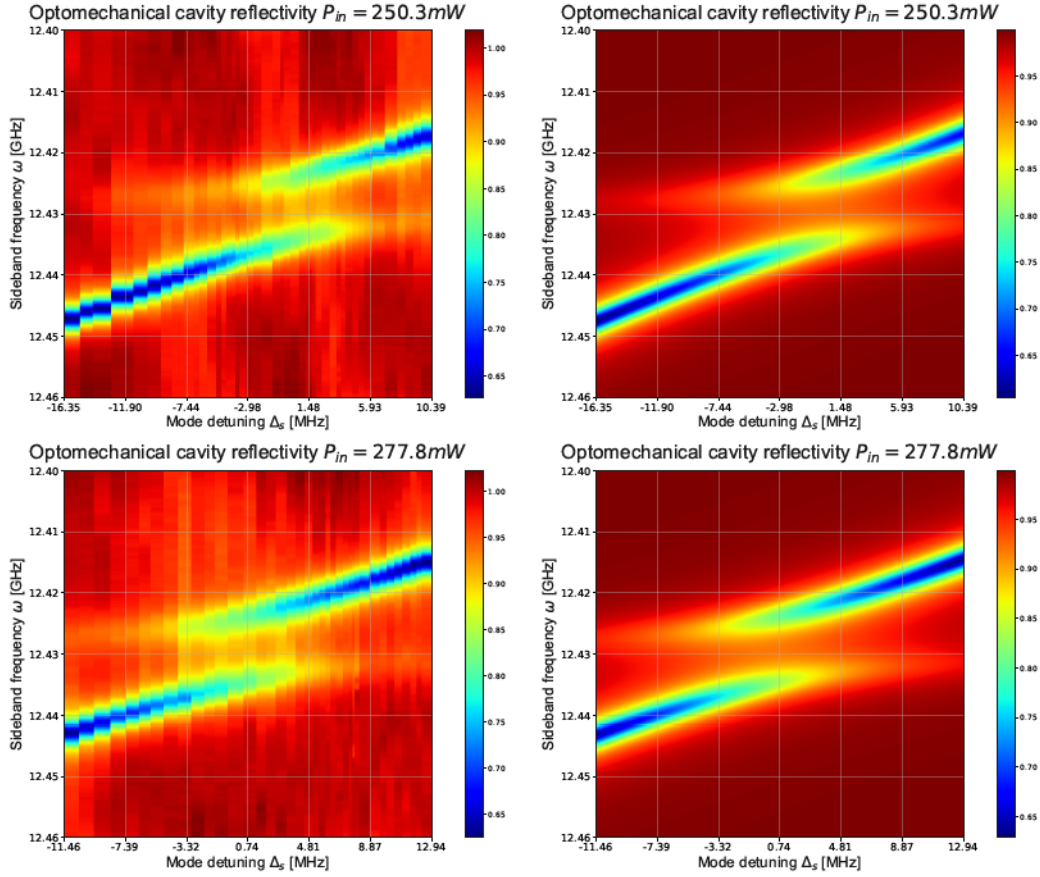
FIGURE 7.17: OMIT detuning measurements at $250.3\,\mathrm{mW}$ and $277.8\,\mathrm{mW}$. On the left, we have the filtered experimental data with detuning obtained from the fitting. On the right, we display the model prediction. After overcoming the strong-coupling threshold, we observe an avoided crossing, with the two resonance peaks resolved at the Brillouin frequency.

counteracted by the Peltier cell. Moreover, extending the dataset to multiple measurements with the same power cannot guarantee the same power condition, increasing the uncertainty of the estimated values. Moreover, the viable improvements imply a redesign of the cavity. Related to cavity stability, the second main issue regards its misalignment. The current mechanical elements do not provide sufficient precision in the crystal and mirror positioning, making the mode shift phenomenon arise. These rapid changes in the resonant modes caused by impaired thermal expansion have been widely studied and can cause a critical failure of the whole experiment. Impacting both the pumping power and the signal mode spectral response, they required looking through hundreds of modes and tens of realignments, searching for a suitable mode pair. An improved crystal holder has been developed, but its tolerances were too high, and new pieces have been machined but have not been tested yet because of delays in the design and manufacturing process. Moreover, the current horizontal design is vulnerable to misalignment compared to a vertical cavity, where gravity helps keep the optics aligned.

Discussing the more general measurement setup, the cavity lock system is the principal limiting factor. If the temperature stability degrades the spectral response data quality and the misalignment slows the search for suitable modes, the lock affects their characterization. The current locking system is very close to its limits and cannot lock the best cavity modes at high powers because the linewidth is smaller than the device threshold ($1\,\mathrm{MHz}$). Increasing

the mode power has a different effect depending on the specific mode and its closeness to the frequency transition regions, so it is hard to predict in advance. A change in the locking system, preferring a PDH locking system developed for high-finesse cavities [64], is compulsory to improve the performance and reduce the challenge in tuning the locking parameters to obtain most of the time a lock with power fluctuations $>10\%$.

Other minor issues include the vibrations propagating from the devices placed on the optical table, which concur with the unstable cavity temperature to the lock instability. Better synchronization between the frequency synthesizer and the spectrum analyzer can reduce the data noise and failed samples. Regarding the data analysis, we can notice that the principal uncertainty source is the optical power estimation because both the drift in the amplifier output power and fluctuation in the lock point prevent a stable value throughout the entire detuning measurement. Integrating the reflected and transmitted power sampling into the acquisition script can improve the estimates, having the instantaneous power measurements for each spectrum. Finally, we should remark that future improvements also involve the test of TeO_2 crystals, which have a higher single-photon coupling rate, and thus require lower powers to enter the strong-coupling regime.

Conclusions and outlooks 8

In this thesis, we presented the experimental characterization of a macroscopic optomechanical cavity comprising two high-reflectivity mirrors and a cm-scale quartz crystal to study the optomechanical response arising from Brillouin scattering at room temperature. From the optomechanics and quantum optics theory, we derive a mathematical model for the spectral response of our cavity, including the coupling coefficients between the external fields and the cavity modes and the optomechanical interactions within the crystal leading to energy transfer between the cavity resonances. In addition to defining reflectivity and transmissivity leading to the definition of Optomechanically Induced Amplification (OMIA) and Transmission (OMIT) phenomena, we simulate the temperature-related behavior of the cavity mode to confirm the tuning feature of the design. Finally, we provide a phenomenological description of the misalignment effects and the cavity instabilities as limits to the performances of our measurement setup.

In discussing the results, we demonstrate both Brillouin lasing and strong-coupling regimes at $1553.8\,\text{nm}$ and $T = 23.7\,^\circ\text{C}$. In the Stokes scattering measurements, we present the shrinking of the hybrid photon-phonon mode linewidth until reaching unitary cooperativity and lasing for $g_m/2\pi \approx 2.3\,\text{MHz}$ and $P_{in} \approx 75\,\text{mW}$. In the Anti-Stokes scattering data, we characterize the mode splitting due to the optomechanical hybridization with a formation of two peaks that move apart when increasing the pumping power. The unitary cooperativity threshold is $g_m/2\pi = 2.476\,\text{MHz}$ ($P_{in} = 51.53\,\text{mW}$) while we enter strong-coupling with an optomechanical coupling strength $g_m/2\pi = 5.284\,\text{MHz}$ and optical pumping power $P_{in} = 238.7\,\text{mW}$. Finally, we estimate the single-photon rate as $g_0/2\pi = 7.76 \pm 0.05\,\text{Hz}$ and the Quartz Brillouin frequency $\Omega_m/2\pi = 12.4296\,\text{GHz}$, values compatible with the theoretical predictions. The data have been presented through detuning measurements, which scan the optomechanical interaction over a frequency range around Ω_m to demonstrate avoided crossing of the modes in the strong-coupling regime. We should remark that the detuning is not power dependent, since the external temperature control allows increasing the laser power and compensating the additional heat introduced into the system from the absorbed light. It allows in-resonance excitation of the pump mode with a consequent increase of the intracavity photon number, thus reaching the strong-coupling regime at room temperature in a GHz-frequency system.

The performance limits lie in the cavity instabilities at high power which prevent a stable frequency lock to the resonance mode and in the cavity misalignment which reduces its quality factor from ≈ 12000 to ≈ 3500 and increases the strong coupling threshold. Improving the crystal alignment and the constraints for the thermal expansion can improve the setup

reliability and is a fundamental requirement for the following experiments. The objective of the project has been met with the complete characterization of the optomechanical response and the strong-coupling regime. Future developments include testing different high-frequency crystalline materials, e.g., TeO_2 ($\Omega_m = 11.7\,\text{GHz}$) and KPT ($\Omega_m = 17\,\text{GHz}$) by removing or adding spacers between the two mirrors.

Several strategies and skills have been improved and will support the development of a cryogenic temperature experiment aiming at coherent long-living phonon modes ($\Gamma_m \ll \kappa_s$) at ground state operation ($T < 100\,\text{mK}$). The creation of a phonon cavity with a high Qf product enables fundamental physics testing with heavy ($m_e \sim \text{µg}$) bulk acoustic waves and hybrid quantum technology development, e.g., coherent state transfer between optical and acoustic modes, storage of quantum information, and generation of non-classical light though the optomechanical interaction.

Bibliography

[1] H. J. Kimble. "The quantum internet". In: *Nature* 453.7198 (June 2008), pp. 1023–1030. DOI: 10.1038/nature07127.

[2] Frank Arute et al. "Quantum supremacy using a programmable superconducting processor". In: *Nature* 574.7779 (Oct. 2019), pp. 505–510. DOI: 10.1038/s41586-019-1666-5.

[3] Petar Jurcevic et al. "Demonstration of quantum volume 64 on a superconducting quantum computing system". In: *Quantum Science and Technology* 6.2 (Mar. 2021), p. 025020. DOI: 10.1088/2058-9565/abe519.

[4] V. V. Sivak et al. "Real-time quantum error correction beyond break-even". In: *Nature* 616.7955 (Mar. 2023), pp. 50–55. DOI: 10.1038/s41586-023-05782-6.

[5] A. Bermudez et al. "Assessing the Progress of Trapped-Ion Processors Towards Fault-Tolerant Quantum Computation". In: *Physical Review X* 7.4 (Dec. 2017). DOI: 10.1103/physrevx.7.041061.

[6] Sergei Slussarenko and Geoff J. Pryde. "Photonic quantum information processing: A concise review". In: *Applied Physics Reviews* 6.4 (Oct. 2019). DOI: 10.1063/1.5115814.

[7] Pu Wang, Yu Zhang, Zhenguo Lu, Xuyang Wang, and Yongmin Li. "Discrete-modulation continuous-variable quantum key distribution with a high key rate". In: *New Journal of Physics* 25.2 (Feb. 2023), p. 023019. DOI: 10.1088/1367-2630/acb964.

[8] Fabian Laudenbach et al. "Continuous-Variable Quantum Key Distribution with Gaussian Modulation-The Theory of Practical Implementations". In: *Advanced Quantum Technologies* 1.1 (June 2018), p. 1800011. DOI: 10.1002/qute.201800011.

[9] A. D. O'Connell et al. "Quantum ground state and single-phonon control of a mechanical resonator". In: *Nature* 464.7289 (Mar. 2010), pp. 697–703. DOI: 10.1038/nature08967.

[10] Alfredo Rueda et al. "Efficient microwave to optical photon conversion: an electro-optical realization". In: *Optica* 3.6 (June 2016), p. 597. DOI: 10.1364/optica.3.000597.

[11] A. P. Higginbotham et al. "Harnessing electro-optic correlations in an efficient mechanical converter". In: *Nature Physics* 14.10 (July 2018), pp. 1038–1042. DOI: 10.1038/s41567-018-0210-0.

[12] Yiwen Chu and Simon Gröblacher. "A perspective on hybrid quantum opto- and electromechanical systems". In: *Applied Physics Letters* 117.15 (Oct. 2020). DOI: 10.1063/5.0021088.

[13] K. Stannigel, P. Rabl, A. S. Sørensen, P. Zoller, and M. D. Lukin. "Optomechanical Transducers for Long-Distance Quantum Communication". In: *Physical Review Letters* 105.22 (Nov. 2010). DOI: 10.1103/physrevlett.105.220501.

[14] Andreas Wallucks, Igor Marinković, Bas Hensen, Robert Stockill, and Simon Gröblacher. "A quantum memory at telecom wavelengths". In: *Nature Physics* 16.7 (May 2020), pp. 772–777. DOI: 10.1038/s41567-020-0891-z.

[15]   Yiwen Chu, Prashanta Kharel, William H. Renninger, Luke D. Burkhart, Luigi Frunzio, Peter T. Rakich, and Robert J. Schoelkopf. "Quantum acoustics with superconducting qubits". In: *Science* 358.6360 (Oct. 2017), pp. 199–202. DOI: 10.1126/science.aao1511.

[16]   A J Leggett. "Testing the limits of quantum mechanics: motivation, state of play, prospects". In: *Journal of Physics: Condensed Matter* 14.15 (Apr. 2002), R415–R451. DOI: 10.1088/0953-8984/14/15/201.

[17]   Rodrigo A. Thomas et al. "Entanglement between distant macroscopic mechanical and spin systems". In: *Nature Physics* 17.2 (Sept. 2020), pp. 228–233. DOI: 10.1038/s41567-020-1031-5.

[18]   Niccolò Fiaschi, Bas Hensen, Andreas Wallucks, Rodrigo Benevides, Jie Li, Thiago P. Mayer Alegre, and Simon Gröblacher. "Optomechanical quantum teleportation". In: *Nature Photonics* 15.11 (Oct. 2021), pp. 817–821. DOI: 10.1038/s41566-021-00866-z.

[19]   Markus Aspelmeyer, Tobias J. Kippenberg, and Florian Marquardt. "Cavity optomechanics". In: *Reviews of Modern Physics* 86.4 (Dec. 2014), pp. 1391–1452. DOI: 10.1103/revmodphys.86.1391.

[20]   B. M. Brubaker et al. "Optomechanical Ground-State Cooling in a Continuous and Efficient Electro-Optic Transducer". In: *Physical Review X* 12.2 (June 2022). DOI: 10.1103/physrevx.12.021062.

[21]   Mohammad Mirhosseini, Alp Sipahigil, Mahmoud Kalaee, and Oskar Painter. "Superconducting qubit to optical photon transduction". In: *Nature* 588.7839 (Dec. 2020), pp. 599–603. DOI: 10.1038/s41586-020-3038-6.

[22]   J.B. Thaxter and P.E. Tannenwald. "Phonon Generation, Propagation, and Attenuation at 70 GHz". In: *IEEE Transactions on Sonics and Ultrasonics* 13.2 (1966), pp. 61–68. DOI: 10.1109/T-SU.1966.29377.

[23]   Dennis Høj, Fengwen Wang, Wenjun Gao, Ulrich Busk Hoff, Ole Sigmund, and Ulrik Lund Andersen. "Ultra-coherent nanomechanical resonators based on inverse design". In: *Nature Communications* 12.1 (Oct. 2021). DOI: 10.1038/s41467-021-26102-4.

[24]   Matt Eichenfield, Ryan Camacho, Jasper Chan, Kerry J. Vahala, and Oskar Painter. "A picogram- and nanometre-scale photonic-crystal optomechanical cavity". In: *Nature* 459.7246 (May 2009), pp. 550–555. DOI: 10.1038/nature08061.

[25]   Simon Gröblacher, Klemens Hammerer, Michael R. Vanner, and Markus Aspelmeyer. "Observation of strong coupling between a micromechanical resonator and an optical cavity field". In: *Nature* 460.7256 (Aug. 2009), pp. 724–727. DOI: 10.1038/nature08171.

[26]   Jasper Chan, T. P. Mayer Alegre, Amir H. Safavi-Naeini, Jeff T. Hill, Alex Krause, Simon Gröblacher, Markus Aspelmeyer, and Oskar Painter. "Laser cooling of a nanomechanical oscillator into its quantum ground state". In: *Nature* 478.7367 (Oct. 2011), pp. 89–92. DOI: 10.1038/nature10461.

[27]   Ralf Riedinger et al. "Non-classical correlations between single photons and phonons from a mechanical oscillator". In: *Nature* 530.7590 (Jan. 2016), pp. 313–316. DOI: 10.1038/nature16536.

[28]   P. Kharel, Y. Chu, D. Mason, E. A. Kittlaus, N. T. Otterstrom, S. Gertler, and P. T. Rakich. "Multimode Strong Coupling in Cavity Optomechanics". In: *Physical Review Applied* 18.2 (Aug. 2022). DOI: 10.1103/physrevapplied.18.024054.

[29]   W. H. Renninger, P. Kharel, R. O. Behunin, and P. T. Rakich. "Bulk crystalline optomechanics". In: *Nature Physics* 14.6 (Apr. 2018), pp. 601–607. DOI: 10.1038/s41567-018-0090-3.

[30] H. Doeleman, T. Schatteburg, R. Benevides, Vollenweider, and Y. Chu. "Brillouin optomechanics in the quantum ground state". In: *arXiv Preprint* (Mar. 2023). DOI: 10.48550/arXiv.2303.04677.

[31] Sissel Bay Nielsen. "Opto-acoustic Coupling in a Pristine Crystal via Brillouin Scattering". PhD thesis. Department of Physics, Technical University of Denmark, 2022.

[32] Prashanta Kharel, Glen I. Harris, Eric A. Kittlaus, William H. Renninger, Nils T. Otterstrom, Jack G. E. Harris, and Peter T. Rakich. "High-frequency cavity optomechanics using bulk acoustic phonons". In: *Science Advances* 5.4 (Apr. 2019). DOI: 10.1126/sciadv.aav0582.

[33] G. Enzian, M. Szczykulska, J. Silver, L. Del Bino, S. Zhang, I. A. Walmsley, P. Del'Haye, and M. R. Vanner. "Observation of Brillouin optomechanical strong coupling with an 11 GHz mechanical mode". In: *Optica* 6.1 (Dec. 2018), p. 7. DOI: 10.1364/optica.6.000007.

[34] Maxim Goryachev and Michael E. Tobar. "Gravitational wave detection with high frequency phonon trapping acoustic cavities". In: *Physical Review D* 90.10 (Nov. 2014). DOI: 10.1103/physrevd.90.102005.

[35] Igor Pikovski, Michael R. Vanner, Markus Aspelmeyer, M. S. Kim, and Časlav Brukner. "Probing Planck-scale physics with quantum optics". In: *Nature Physics* 8.5 (Mar. 2012), pp. 393–397. DOI: 10.1038/nphys2262.

[36] Yi Xia, Aman R. Agrawal, Christian M. Pluchar, Anthony J. Brady, Zhen Liu, Quntao Zhuang, Dalziel J. Wilson, and Zheshen Zhang. "Entanglement-enhanced optomechanical sensing". In: *Nature Photonics* 17.6 (Apr. 2023), pp. 470–477. DOI: 10.1038/s41566-023-01178-0.

[37] Carlos J. Bustamante, Yann R. Chemla, Shixin Liu, and Michelle D. Wang. "Optical tweezers in single-molecule biophysics". In: *Nature Reviews Methods Primers* 1.1 (Mar. 2021). DOI: 10.1038/s43586-021-00021-6.

[38] Alberto Barchielli and Bassano Vacchini. "Quantum Langevin equations for optomechanical systems". In: *New Journal of Physics* 17.8 (Aug. 2015), p. 083004. DOI: 10.1088/1367-2630/17/8/083004.

[39] *03 Free spectral range | Learn Laser Interferometry with Finesse*. 2009. URL: https://www.gwoptics.org/learn/02_Plane_waves/01_Fabry_Perot_cavity/03_Free_spectral_range.php (visited on 08/18/2023).

[40] *Zero-Point Fluctuations - Open Quantum Sensing and Measurement Notes*. 2019. URL: https://qsm.quantumtinkerer.tudelft.nl/4_ZPFs/ (visited on 08/18/2023).

[41] William Weber Coblentz. "Absorption, Reflection, and Dispersion Constants of Quartz". In: 237. US Department of Commerce, Bureau of Standards, 1915, pp. 471–481.

[42] D. Marcuse. "Coupled mode theory of optical resonant cavities". In: *IEEE Journal of Quantum Electronics* 21.11 (Nov. 1985), pp. 1819–1826. DOI: 10.1109/jqe.1985.1072590.

[43] *Thermal Expansion - Linear Expansion Coefficients*. 2003. URL: https://www.engineeringtoolbox.com/linear-expansion-coefficients-d_95.html (visited on 08/18/2023).

[44] Gorachand Ghosh. "Dispersion-equation coefficients for the refractive index and birefringence of calcite and quartz crystals". In: *Optics Communications* 163.1-3 (May 1999), pp. 95–102. DOI: 10.1016/s0030-4018(99)00091-7.

[45]   Robert W. Boyd. "Chapter 9 - Stimulated Brillouin and Stimulated Rayleigh Scattering". In: *Nonlinear Optics (Third Edition)*. Ed. by Robert W. Boyd. Third Edition. Burlington: Academic Press, 2008, pp. 429–471. ISBN: 978-0-12-369470-6. DOI: `https://doi.org/10.1016/B978-0-12-369470-6.00009-5`.

[46]   Robert W. Boyd. "Chapter 8 - Spontaneous Light Scattering and Acoustooptics". In: *Nonlinear Optics (Third Edition)*. Ed. by Robert W. Boyd. Third Edition. Burlington: Academic Press, 2008, pp. 391–428. ISBN: 978-0-12-369470-6. DOI: `https://doi.org/10.1016/B978-0-12-369470-6.00008-3`.

[47]   Sellmeier. "Zur Erklärung der abnormen Farbenfolge im Spectrum einiger Substanzen". In: *Annalen der Physik und Chemie* 219.6 (1871), pp. 272–282. DOI: `10.1002/andp.18712190612`.

[48]   A. Yariv. "Quantum theory for parametric interactions of light and hypersound". In: *IEEE Journal of Quantum Electronics* 1.1 (1965), pp. 28–36. DOI: `10.1109/JQE.1965.1072182`.

[49]   A. Schliesser, R. Rivière, G. Anetsberger, O. Arcizet, and T. J. Kippenberg. "Resolved-sideband cooling of a micromechanical oscillator". In: *Nature Physics* 4.5 (Apr. 2008), pp. 415–419. DOI: `10.1038/nphys939`.

[50]   Ulrik L Andersen, Tobias Gehring, Christoph Marquardt, and Gerd Leuchs. "30 years of squeezed light generation". In: *Physica Scripta* 91.5 (Apr. 2016), p. 053001. DOI: `10.1088/0031-8949/91/5/053001`.

[51]   R. Y. Teh, S. Kiesewetter, P. D. Drummond, and M. D. Reid. "Creation, storage, and retrieval of an optomechanical cat state". In: *Physical Review A* 98.6 (Dec. 2018). DOI: `10.1103/physreva.98.063814`.

[52]   *Quartz Crystals, Birefringent Crystals, quartz crystal wafers, quartz crystal ingot, quartz crystal substrate*. 2023. URL: `https://www.shalomeo.com/Laser-Crystals-and-Components/Quartz-Crystals/product-276.html` (visited on 08/18/2023).

[53]   *Low-Loss Mirrors | LayerTec*. 2023. URL: `https://www.layertec.de/en/products-services/mirrors/low-loss-mirrors/` (visited on 08/18/2023).

[54]   *Mirror coating NIR 1065-2500 nm | LaserOptik*. 2023. URL: `https://www.laseroptik.com/en/coatings/ranges/nir-1065-2500-nm` (visited on 08/18/2023).

[55]   *DLC pro | TOPTICA Photonics AG*. 2023. URL: `https://www.toptica.com/products/tunable-diode-lasers/ecdl-dfb-lasers/dl-pro` (visited on 08/18/2023).

[56]   *Lithium Niobate Electro-Optic Modulators, Fiber-Coupled (1260 nm - 1625 nm) | Thorlabs*. 2023. URL: `https://www.thorlabs.com/newgrouppage9.cfm?objectgroup_id=3918` (visited on 08/18/2023).

[57]   *APMS - up to 40 GHz Multi-Channel Signal Generator | AnaPico*. 2023. URL: `https://www.anapico.com/products/rf-signal-generators/multi-channel-analog-and-digital-signal-generator/apms-models-multi-channel-signal-generators-up-to-40-ghz/` (visited on 08/18/2023).

[58]   *Koheras BOOSTIK HP Amplifier | NKT Photonics*. 2023. URL: `https://www.nktphotonics.com/products/single-frequency-fiber-lasers/koheras-boostik-hp/` (visited on 08/18/2023).

[59]   *225 W TEC Controller | Thorlabs*. 2023. URL: `https://www.thorlabs.com/newgrouppage9.cfm?objectgroup_id=3512` (visited on 08/18/2023).

[60]   *Fiber-Q® fiber-coupled acousto-optic modulators | G&H*. 2023. URL: `https://gandh.com/products/fiber-optics/fiber-q-fiber-coupled-modulators/fiber-q-pm-1550-nm-200-mhz-hermetic-fiber-coupled-aom` (visited on 08/18/2023).

[61]   *Ultrafast Fiber Optic Photodetector Modules | Thorlabs*. 2023. URL: https://www.thorlabs.com/newgrouppage9.cfm?objectgroup_id=11975#ad-image-0 (visited on 08/18/2023).

[62]   *Double Balanced Mixer, RF/LO Freq 7500 - 20000 MHz | Mini-Circuits*. 2023. URL: https://www.minicircuits.com/WebStore/dashboard.html?model=ZX05-24MH-S%2B (visited on 08/18/2023).

[63]   *N9000A CXA Signal Analyzer, 9 kHz to 26.5 GHz | Keysight*. 2023. URL: https://www.keysight.com/us/en/product/N9000A/cxa-signal-analyzer-9khz-26-5ghz.html (visited on 08/18/2023).

[64]   Eric D. Black. "An introduction to Pound–Drever–Hall laser frequency stabilization". In: *American Journal of Physics* 69.1 (Jan. 2001), pp. 79–87. DOI: 10.1119/1.1286663.